Structure determination of thin polymer films using GIXRD and AFM

Huw E. Thomas

Thesis submitted for the degree of doctor of philosophy

School of Physics and Astronomy

Cardiff University

March 2010

ProQuest LLC
789 East Eisenhower Parkway
P.O. Box 1346
Ann Arbor, MI 48106-1346

Abstract

Structure determination of thin polymer films using GIXRD and AFM

Both atomic force microscopy (AFM) and grazing incidence x-ray diffraction (GIXRD) are used to determine the structure of polymer thin films. To enable experiments using these techniques to be conducted experimental apparatus was designed and built. These apparatus' included an in-situ heater to allow investigations at elevated temperatures to be conducted as well as a chamber for the work conducted using GIXRD to minimise the background scattering incident on the detector.

The structure of two polymers, F8 and PQT-12, have been investigated using GIXRD. Both of these polymers align in a layered geometry normal to the surface, and in an isotropic polycrystalline ordering in the plane of the surface. The F8 polymer, while in the α-crystalline phase, has a unit cell dimension of 27.3 ± 0.3Å normal to the surface and unit cell dimensions of 24.3 ± 0.3Å and 17.1 ± 0.2Å in the plane of the surface. As-spun PQT-12 of molecular weight of 5000amu has been found to form a metastable self-assembled crystalline phase with unit cell dimensions of 35.6 ± 0.7Å out-of-plane and 13.10 ± 0.12Å, 16.4 ± 0.6Å in-plane. The structure of PQT-12 has been shown to be dependent on molecular weight, annealing and physical preparation of the substrate.

The rate and mechanisms of crystallisation of a third polymer, PET, have also been investigated as a function of anneal temperature. The crystallisation was followed at each given temperature to follow the growth of individual spherulites. As the thickness of the PET film was increased from 43nm to 120 nm the radial growth rate of the spherulites increased linearly from 8.0 ± 0.9nm/min to 14.3 ± 1.3nm/min.

Contents

CHAPTER 1 – THESIS INTRODUCTION

1.1 Background of the materials and apparatus

Polymer interfaces and thin films play an increasingly important role in a wide range of applications, for example, packaging, barriers, adhesion, membranes, sensors, and medical implants [1-4]. These applications exploit both structural and chemical properties of the polymers. The molecular properties are often optimised by processes such as thermal annealing. Techniques such as x-ray diffraction have been used to follow the detailed changes that occur during processing in bulk polymers. However such studies are rare for polymer thin films. In this study we develop and exploit such in-situ studies of polymer thin films using grazing-incidence x-ray diffraction (GIXRD) and atomic force microscopy (AFM). We focus on a particular class of functional polymer, the liquid-crystalline conjugated polymers, with one study of a non-conjugated system,

poly(ethylene terephthalate), commonly used in packaging and soft-drinks bottles. The techniques developed are more widely applicable to any thin-film polymer system.

Conjugated polymers are a group of polymers which have alternating single and double bonds along the backbone of the polymer. Their backbones consist of contiguous sp^2 hybridized carbon centers. One valence electron on each centre resides in a p_z orbital, which is orthogonal to the other three sigma-bonds. These p_z orbitals form a partly delocalised electron density above and below the plane of the backbone. This bonding orientation is illustrated in figure 1.1.

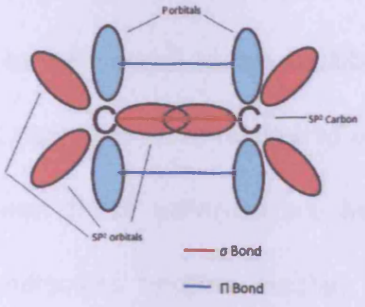

Figure 1.1 Bonding mechanisms for the carbon atoms along a conjugated backbone taken from [5].

Alan J. Heeger, Alan MacDiarmid and Hideki Shirakawa were awarded the 2000 Nobel prize in Chemistry *"For the discovery and development of conductive polymers"*, resulting from their work from the late 1970s. They have received much interest since their inception as they have the advantages of other non-conjugated polymers such as flexibility, toughness, malleability, elasticity, etc. [6] as well as having electrical advantages such as conduction, which is possible along its conjugated backbone. Historically these polymers were not used for their electrical properties as the electron

mobility was dramatically lower than in their semiconducting counterparts [6]. Recently however, modifications made to the polymers have enabled them to be used in a number of applications such as solar cells, and OLED flat screen displays [7-8].

The conjugated polymers investigated in this thesis are poly(9,9-di-n-octyl-2,7-fluorene), more commonly known as F8, and poly(3,3'''-didodecylquaterthiophene), PQT-12. As well at looking at these conjugated polymers we have also invested the polymer polyethylene terephthalate, PET.

At room temperature, the structure of these polymers is metastable. That is, the molecules are not necessarily in their lowest energy equilibrium state, but the individual strands do not have sufficient energy to move relative to one another in order to attain their equilibrium state. When these polymers are heated to a sufficiently high temperature, the polymer molecules become mobile, allowing them to approach equilibrium at this higher temperature, which may or may not involve a change of state. A more detailed explanation of this process can be found in chapter two. This thesis is mainly tailored to investigating the structure of the stated polymers in the crystalline phase. The crystalline phase produces a higher density of diffraction spots during the GIXRD experiments.

The use of GIXRD and AFM to study the structure of thin films complement each other well. As will be explained in more detail in the thesis, the depth at which GIXRD is sensitive within the sample can be tuned by altering the incident angle of the incoming

x-ray beam. At certain incident angles the observed scattering is only sensitive to the structure at the surface of the film, and at higher angles the diffraction pattern is sensitive to the structure in the 'bulk' of the film. The use of AFM complements the GIXRD experiments as the surface morphology of the thin films can further be investigated. In addition GIXRD probes the average, ordered structure of the film, whereas AFM images the local structure, whether ordered or disordered.

The three materials investigated are now introduced in turn.

1.2 Materials investigated

1.2.1 Poly(9,9-di-n-octyl-2,7-fluorene)

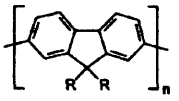

Figure 1.2 The repeating monomer structure of poly(9,9-di-n-octyl-2,7-fluorene), F8.

The main investigation into this polymer will be into its unit cell structure using GIXRD. Previously all attempts to determine the complex internal unit cell structure of conjugated polymers have been unsuccessful. This is mainly due to the weak scattering observed from the highly disordered film, and the limited number of crystalline peaks. In this investigation we will attempt to outline a possible method of obtaining such a structure. The process includes using an area detector to detect the scattered X-rays which can detect a large area of reciprocal space, allowing more crystalline peaks to be detected. These peaks are used in the analysis of the images recorded by the area

detector. Though the internal structure of the unit cell for this conjugated polymer has not been determined, it is believed that the method outlined in this work could be developed further to finally postulate a structure of F8, along with other conjugated polymers.

1.2.2 Poly(3,3'''-didodecylquaterthiophene)

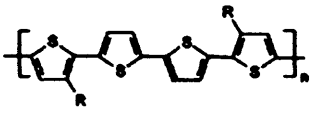

Figure 1.3 The repeating monomer structure of poly(3,3'''-didodecylquaterthiophene), PQT-12.

As with the F8 investigation, GIXRD is used to investigate the structure of this material. In chapter 5 we determine the unit cell parameters of this material in a thin film. PQT-12 has been shown to have relatively high electron mobility, and to be stable in air [9-10], unlike other conjugated polymers that are used in electrical applications, and as such has received particular attention in recent years. The structure was investigated at room temperature for as-spun samples, and also heated in-situ to determine how the structure of the films change as the polymer is heated through its glass transition temperature.

PQT-12 devices are often prepared by deposition of the polymer on top of an OTS modified monolayer surface. This has been shown to improve the electrical properties of the resulting devices [11-13]. Also investigated in chapter 5 was the affect that this monolayer has on the resulting structure of the overlying PQT-12 film.

Additionally the effect of molecular weight on the structure of the film was investigated.

1.2.3 Polyethylene terephthalate

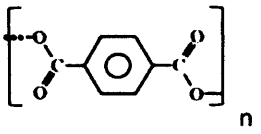

Figure 1.4 The repeating monomer structure of Poly(ethylene terephthalate), PET.

As stated previously, we investigated the concerned polymers using both GIXRD and scanning probe microscopy. Chapter 6 uses SPM, and more specifically AFM, to determine the rate of crystallisation of PET in thin films, and how the rate of crystallisation is affected by film thickness as well as crystallisation temperature.

The PET samples were annealed in-situ up to the desired crystallisation temperature, and the samples were continually scanned, taking images every 15 minutes. While scanning, the size of the growing spherulites was observed. These images were analysed to obtain the size of several spherulites within the scanning region, and a rate of crystallisation is inferred from these sizes.

The range of temperatures investigated was restricted by the fact that the piezoelectric tubes used by the AFM system to move the sample beneath the scanning probe would degrade at higher temperatures, which would limit the possibility of observing individual spherulites developing.

1.3 Instrumentation

In chapter 3 the design considerations for the equipment developed for these studies is outlined. The GIXRD experiments required a specific design brief. Since the investigated polymer films are highly disordered materials of low atomic number, scattering from windows and even the surrounding air is stronger than the required diffraction signal. Therefore the apparatus needed to be able to suppress background scattering to a manageable level. The apparatus was also required to enable the detector to detect a large area of reciprocal space efficiently.

A second demanding experimental requirement relates to in-situ AFM experiments conducted during annealing. The space available for the sample and heater in our Veeco Multimode AFM instrument is very limited. This required the design of a heater stage that was both very compact and yet provided sufficient temperature gradient over a short distance to prevent the piezo tubes overheating, causing long-term damage. The design of these heaters is discussed in chapter 6.

1.4 References

[1] R. Jones, Current opinions in solid state & materials science, 1997, 2, 673.

[2] D. Klee, H. Hocker, Biomedical applications: Polymer blends, 1999, 149, 1.

[3] Q. F. Li, J. O. Jensen, R. F. Savinell et al, Progress in polymer science, 2009, 34, 449.

[4] T. Nakamura, Analytical Sciences, 2007, 23, 253.

[5] http://chemwiki.ucdavis.edu/Organic_Chemistry/Conjugation/Overlap_of_Adjacent _p_ Orbitals-Electron_Delocalization

[6] http://en.wikipedia.org/wiki/Conductive_polymer#cite_note-22

[7] K. M. Coakley, M. D. McGehee, Chem. Mater., 2004, 16, 4533.

[8] M. O'Neill, S. M. Kelly, Adv. Mater., 2003, 15, 1135.

[9] B. Ong, Y. Wu, P. Liu Proceedings of the IEEE, 2005, 93, 1412.

[10] B. Ong, Y. Wu, P. Liu, S. Gardner, J. AM. Chem. Soc. 2004, 126, 3378.

[11] R. Hayakawa, M. Petit, T. Chikyow et al, Appl. Phys. Letters, 2008, 93, 153301.

[12] R. Hayakawa, N. Hiroshiba, T. Chikyow et al, Thin Solid Films, 2009, 518, 437.

[13] Y. Sun, X. Lu, S. Lin et al, Organics Electronics, 2010, 11, 351.

CHAPTER 2 – BACKGROUND THEORY

2.1 X-ray Diffraction

X-Rays were discovered in 1895 when Wilhelm Conrad Röntgen saw a faint flicker on a fluorescent screen a few metres away from a cathode ray experiment he was running. He knew that cathode rays do not penetrate air over this distance so postulated that a new form of radiation had been discovered. He named the new rays 'X' due he fact he didn't know what they were. In later experiments Rontgen discovered that x-rays have different penetration depths depending on the material. This was illustrated beautifully when he placed his wife's hand between the x-ray source and a photographic plate and produced the first "x-ray picture". This result led to huge advances in medical diagnosis, but it also inspired Max von Laue to study the effect of x-rays on solids. He observed spots on photographic-film consistent with diffraction from a periodic array, and developed an elementary theory of

diffraction by a periodic array of atoms[1]. Laue also showed that X-ray wavelengths were of the order of the interatomic spacing, a.

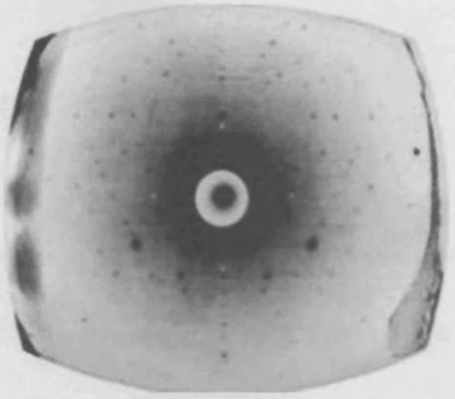

Figure 2.1. Diffraction pattern observed by Laue which resulted in him receiving the Nobel prize for Physics in 1914 taken from [2].

When dealing with scattering processes between waves and particles it is important to understand which regime one is dealing with. In the classical regime, there is an elastic "collision", and no energy is transferred between the wave and the particle (Thompson scattering). In the quantum mechanical regime the incident photon loses some energy to the particle and the exiting photon has less energy than the incident photon (Compton scattering). In both cases however, momentum is conserved, and the scattering event leads to the definition of the scattering vector **Q**.

$$\hbar \boldsymbol{Q} = \hbar \boldsymbol{k}_f - \hbar \boldsymbol{k}_i$$

..Equation 2.1

where ħ**Q** is the momentum transfer (i.e. the momentum transferred from the photon to the sample). The scattering vector is an important concept in diffraction

and will be explained further later in the chapter. For the experiments undertaken throughout this thesis a classical scattering approach is used. The case of an electromagnetic (EM) wave approaching a single electron will now be considered.

2.1.1 Scattering from one and two electron systems

When an EM wave approaches a single electron, the wave's electric field will exert a Lorentz force on the electron. The wave is periodic in time and the electron will therefore accelerate, and radiate another x-ray beam of equal wavelength to that of the incident x-ray. The electron will radiate in all directions, and the maximum amplitude of the scattered spherical wave is given by the equation [3]:

$$A(r) = A_0 \frac{1}{r} \frac{e^2}{mc^2}$$

..Equation 2.2

where A is the amplitude of the radiated wave, A_0 is the amplitude of the incident EM wave, r is the distance away from the electron in the plane of the EM wave, e is the charge of the electron, m is the mass of the electron and c is the speed of the incoming EM wave. The amplitude A of the spherical wave will depend on the observation direction, and on the relative orientation of the planes of polarisation of the incoming and scattered waves: equation 2.2 gives the maximum value when the scattering angle is zero. During this thesis there will be experiments that require intensities of diffracted peaks to be measured, and these effects will be discussed later.

We now progress from the single electron model to consider the radiation from two electrons. Each electron will behave as described above, but now it is important to consider how the radiation emitted from these two electrons will interact.

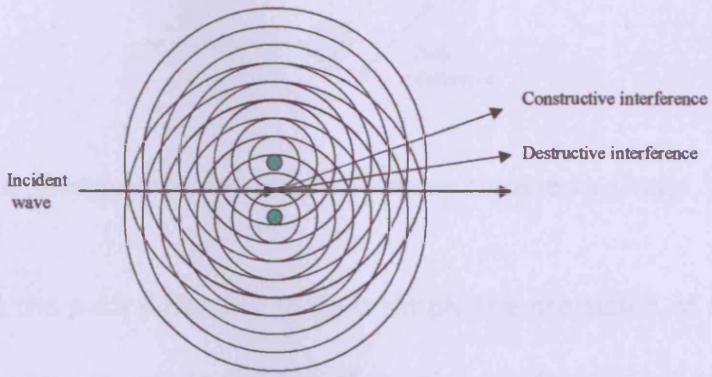

Figure 2.2, scattering pattern for two electrons

Figure 2.2 shows an incident X-ray being scattered by two electrons. The two extreme cases have been labelled, the first being the direction in which the peaks of the two waves radiated overlap and interfere constructively, and the second where the peak of the radiation emitted from one electron overlaps a trough of the other. When the two rays interfere constructively the difference in length of the two paths is a multiple number of wavelengths, or the phase between them is a multiple number of 2π.

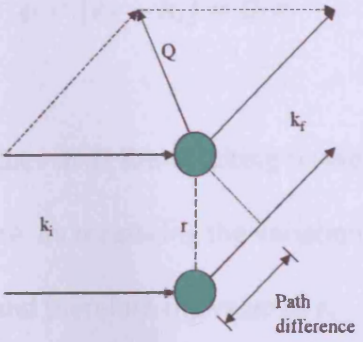

Figure 2.3, definition of the path difference between two scattering waves

As seen in figure 2.3 the path difference (p.d.) is simply the projection of r on the path of the radiated x-ray, or written in terms of the phase difference (φ), $\mathbf{k}_f.\mathbf{r}$. This is due to the fact that:

$$\varphi = \frac{2\pi}{\lambda} * \text{p.d}$$

..Equation 2.3

and the magnitude of the wavevector $\boldsymbol{k}_f = \frac{2\pi}{\lambda}$

..Equation 2.4

This example has been explained with r perpendicular to the incident x-ray. This of course is not always the case, and so the phase difference due to the incident x-ray arriving at the two electrons at different times has to be considered. The same idea (that the phase difference can be calculated by considering the projection of **r** on $\mathbf{k}_i$) can be applied, and the incident phase difference is calculated to be $\mathbf{k}_i.\mathbf{r}$. Applying these two equations to equation 2.1, the total phase difference at any configuration is given by:-

$$\varphi = (\boldsymbol{k}_f - \boldsymbol{k}_i) = \boldsymbol{Q}.\boldsymbol{r}$$

..Equation 2.5

This implies that for certain values of **Q** the resulting phase shift will equal 2π and therefore constructively interfere. By measuring the variation of intensity with angle, one can calculate the Q vector and therefore the value of **r**.

2.1.2 Scattering from atoms and molecules

In the two-electron system it is sufficient to know only the position of several values of Q for constructive interference to calculate the distance between the electrons. In more complex scattering systems the "scattering amplitude" at any given **Q** must be known. If A_0 is the amplitude of an incident wave and r is defined as a vector between two electrons the scattering amplitude, $A(\boldsymbol{Q})$, can be defined as:-

$$A(\boldsymbol{Q}) = A_0 \exp\,(2\pi i \boldsymbol{Q}.\boldsymbol{r})$$

..Equation 2.6

When there is more than one electron in a system, the scattering from all the electrons must be considered, and also the phases between the scatterings. Therefore equation 2.6 can be extended to include these extra scattering sites, to become

$$A(\boldsymbol{Q}) = A_0 \sum_{\mathbf{r}} \rho(\mathbf{r}) \exp\,(2\pi i \boldsymbol{Q}.\boldsymbol{r})$$

..Equation 2.7

where **r** defines the position of each electron and ρ(**r**) defines the electron distribution of each electron. The scattering from all the electrons in an atom is called the atomic form factor. This term can then be extended to calculate the scattering amplitude of a molecule:

$$A_{mol}(\boldsymbol{Q}) = \sum_j f_j(\boldsymbol{Q}) \exp\,(i\boldsymbol{Q}.\boldsymbol{r_j})$$

..Equation 2.8

where f_j(**Q**) is the atomic form factor of the jth atom in the molecule. Similarly, the scattering amplitude equation can be altered to incorporate scattering from molecules, and can be further altered to include all molecules in a crystal structure.

$$A_{crystal}(\boldsymbol{Q}) = \sum_j f_j(\boldsymbol{Q}) \exp\,(i\boldsymbol{Q}.\boldsymbol{r_j}) \sum_m \exp\,(i\boldsymbol{Q}.\boldsymbol{R_m})$$

..Equation 2.9

Equation 2.9 above is similar in form to equation 8 but it includes an extra term. A crystal structure can be defined by a repeating array of atoms called the unit cell. This is illustrated in figure 2.4 where ***r*** is the position of the atoms within the unit cell and ***R*** is the position of each of the unit cells within the crystal.

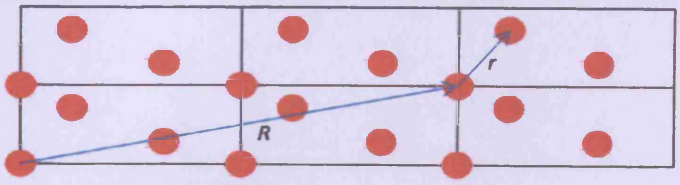

Figure 2.4. The definition of vectors ***r*** and ***R*** within a crystal.

The first term in equation 2.9 sums up the scattering contributions from all the atoms (or molecules) within the unit cell, and the extra term sums up the scattering contributions from all the unit cells, m, in the crystal, therefore summing up all scattering from each of the atoms in the crystal [5].

We now consider how the size of the crystal affects the overall diffraction pattern. If the crystal structure is simplified to a 1-D chain having one atom per unit cell, ie an atom every ua along the chain where u is an integer and a is the atomic spacing, the second term in equation 2.9 will become $\sum e^{iQ.au}$. This term can be recognised as a simple geometric series whose resultant can be calculated to be $\sum e^{iQ.au} = \frac{1-e^{iQ.Na}}{1-e^{iQ.a}}$, where N is the number of atoms along the 1-D chain. Since the scattering amplitude is proportional to this geometric series, and the intensity of the scattered wave is equal to the scattering amplitude multiplied by its complex conjugate, the resultant intensity is calculated to be:-

$$I \propto \frac{1-e^{iQ.Na}}{1-e^{iQa}} * \frac{1-e^{-iQ.Na}}{1-e^{-iQa}} = \frac{sin^2\left(\frac{NQa}{2}\right)}{sin^2\left(\frac{Qa}{2}\right)}$$

..Equation 2.10

Figure 2.5 shows two intensity distributions for this series for N=3 and N=10.

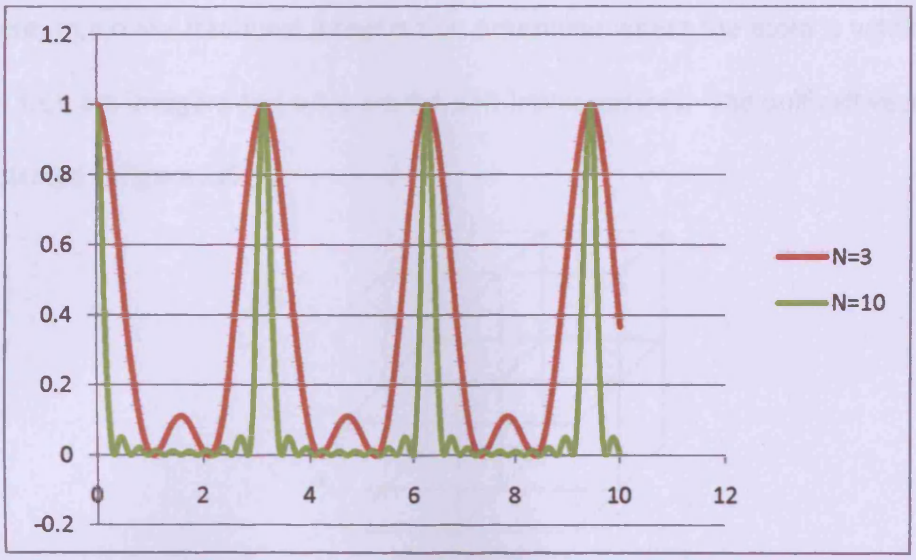

Figure 2.5. Effect of varying the number of repeating units.

As can be seen the higher the value for N the sharper the peaks become. (The two intensity distributions have been normalised to highlight the shape of the peaks)

2.1.3 The reciprocal lattice, Laue equations & the Ewald sphere

As mentioned previously, a crystal can be defined by a repeating unit cell. The unit cell has a definite volume, and is defined by a set of vectors that determines the shape of the cell. These vectors are called the unit lattice vectors. An atom's position in a crystal can then be defined by: -

$$r_{atom} = (m\boldsymbol{a} + n\boldsymbol{b} + o\boldsymbol{c}) \quad + \quad (s\boldsymbol{a} + t\boldsymbol{b} + u\boldsymbol{c})$$

..Equation 2.11

where m,n,o are fractional integers that determine where the atom is within a unit cell. s,t,u are integers and a,b,c are the unit lattice vectors. The unit cell vectors are illustrated in figure 2.6.

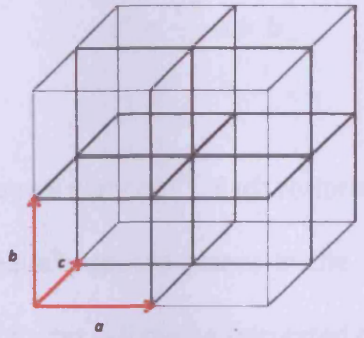

Figure 2.6. Definition of the unit cell vectors ***a***, ***b*** and ***c***.

Previously it was shown that for constructive interference the phase shift between scattering must be equal to 2π radians ie $\mathbf{Q}.\mathbf{r}=2\pi$. Therefore for scattering from neighbouring unit cells to constructively interfere the following must simultaneously occur:

$$\left.\begin{aligned} \mathbf{Q}.\mathbf{a} &= 2\pi h, \\ \mathbf{Q}.\mathbf{b} &= 2\pi k, \text{ and} \\ \mathbf{Q}.\mathbf{c} &= 2\pi l \end{aligned}\right\} \quad \text{where } h,k,l \text{ are integers}$$

..Equations 2.12

These conditions are called the Laue equations and points in Q space where these are satisfied form the reciprocal lattice. Like the real space vectors (**a**, **b**, **c**) these points also lie on a grid that can be defined in terms of vectors **a***, **b*** and **c***. For constructive interference $\mathbf{Q}=\mathbf{G}_{hkl}$ where $\mathbf{G}_{hkl}=h\mathbf{a}^*+k\mathbf{b}^*+l\mathbf{c}^*$. Using this and the Laue equations it can be shown that the reciprocal lattice vectors are

$$\boldsymbol{a}^* = \frac{2\pi}{V}\boldsymbol{b} \times \boldsymbol{c}$$

$$\boldsymbol{b}^* = \frac{2\pi}{V}\boldsymbol{c} \times \boldsymbol{a}$$

$$\boldsymbol{c}^* = \frac{2\pi}{V}\boldsymbol{a} \times \boldsymbol{b}$$

..Equations 2.13

where V is the volume of the real unit cell [5]. Each reciprocal lattice point represents an *hkl* set of parallel and equally spaced planes in the real lattice. This distance between the planes for a cubic unit cell can be calculated by the equation:

$$d_{hkl} = \frac{1}{\sqrt{h^2\boldsymbol{a}^2 + k^2\boldsymbol{b}^2 + l^2\boldsymbol{c}^2}}$$

..Equation 2.14

The Ewald Sphere construction is a useful aid in visualising the properties of Bragg's law. A sphere is drawn in reciprocal space with a radius of $2\pi/\lambda$ through the origin of the reciprocal lattice. If any lattice points lie on the sphere surface then the Laue equations are satisfied and diffraction arises. In theory, if the scattering process was elastic and the X-rays were monochromatic then the sphere would be infinitely thin and no lattice points would lie on the sphere. In practise, this is not the case, and diffraction is seen. Figure 2.7 shows the Ewald sphere for a white beam. If a white beam is used to illuminate a sample then a large range of diffraction spots can be seen.

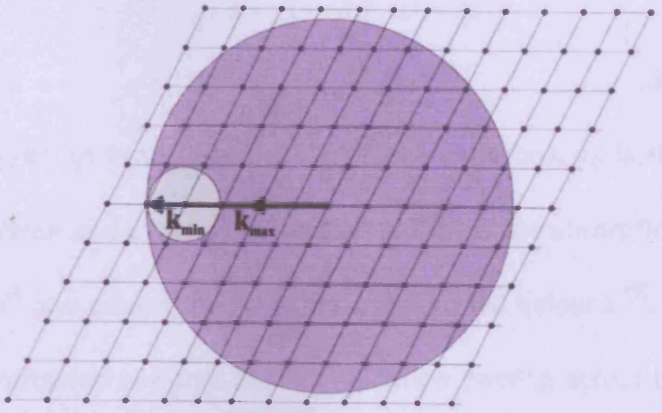

Figure 2.7. Construction of the Ewald Sphere [5]

2.1.4 Refraction

During grazing incident x-ray diffraction the amplitude and penetration depth within the polymer medium is determined by refraction. When light passes through one medium, with a particular refractive index, into another medium with a different refractive index, the light changes direction. This was first observed by Snell and resulted in the equation;

$$n_1 cos(\alpha) = n_2 cos(\alpha')$$

..Equation 2.15

where α is the incident angle, α' is the angle in the medium and n_1, n_2 are the refractive indices within the two mediums. For most wavelengths the refractive index of solids is between 1.2 and 2.0, but for x-rays, where the x-ray's frequency is much larger than that of any resonant frequencies of the particles, the equation for a medium's refractive index becomes: [5]

$$n = 1 - \delta + i\beta$$

..Equation 2.16

Where $\delta = 2\pi\rho r_0/k^2$ (ρ is the number density of electrons, r_0 is the scattering amplitude per electron and k is the wavevector) and $i\beta$ is the absorption effect. δ is of the order of 10^{-5} and causes the refractive index to fall below 1 [5]. Rather than the x-rays being refracted towards the normal when passing across the interface, they are refracted away from the interface normal. This implies that below a 'critical angle', α_c, the x-rays are reflected.

If we consider a wave incident on a sharp interface between vacuum and a sample of refractive index n, where α_i is the angle of incidence and α_i' is the angle of refraction, then Snell's law states that [6]

$$\alpha_i'^2 = \alpha_i^2 - \alpha_c^2$$

..Equation 2.17

This implies that when the incident angle is below the critical angle the refracted angle becomes imaginary. This results in the wavevector 'within' the sample also being imaginary, and an evanescent wave occurs, which is exponentially damped normal to the surface. Due to the heavily damped nature of this wave the 1/e penetration depth is small and equal to [7]

$$\Lambda_i = \left(2kIm(\alpha')\right)^{-1}$$

..Equation 2.18

For polymers this is typically of the order of 15-50Å at incident angles < α_c.

During GIXRD experiments the incident angle is varied around the critical angle to probe different depths within the sample, but to know how the incident angle compares with the critical angle one must know at what angle the critical angle occurs. In order to do this we must turn to Maxwell's equations. The amplitudes of the reflected and refracted waves for small angles are given by [8]

$$E_{reflected} = \left(\frac{\alpha_i - \alpha_i'}{\alpha_i + \alpha_i'}\right) E_i = RE_i$$

$$E_{refracted} = \left(\frac{2\alpha_i}{\alpha_i + \alpha_i'}\right) E_i = TE_i$$

..Equation 2.19

At angles below the critical angle the x-rays are totally externally reflected and R=1. When $\alpha_i = \alpha_c$ the transmission within the sample is twice the incident. This is due to the incident and reflected wave being in phase. At angles above the critical angle the transmission falls off towards 1. The amplitude and intensity of the transmitted wave are shown below.

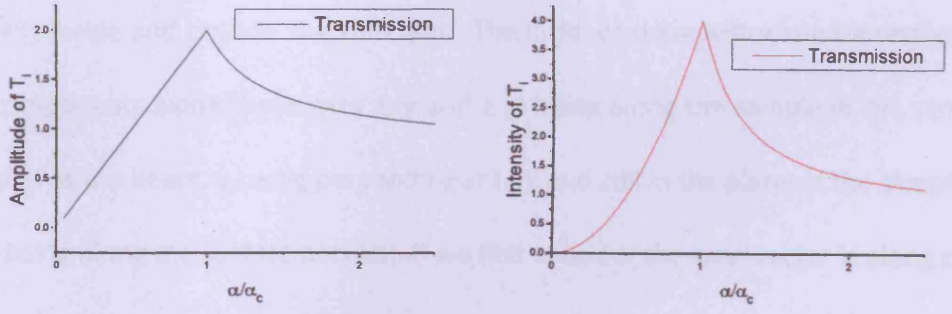

Figure 2.8. Transmission Amplitude and Intensity as a function of incident angle.

Experiments described in this thesis have x-rays travelling from a helium environment into a thin polymer film encountering a change in refractive index and therefore a change in direction. Probing of the samples will be performed with the incident angle of the x-ray beam at and around the critical angle of thin polymer film, and therefore the difference between the k vector in and outside the film will need to be considered, and corrections to the observed scattering angle maybe required to translate the observed scattering angles into the scattering angles realised in the polymer films.

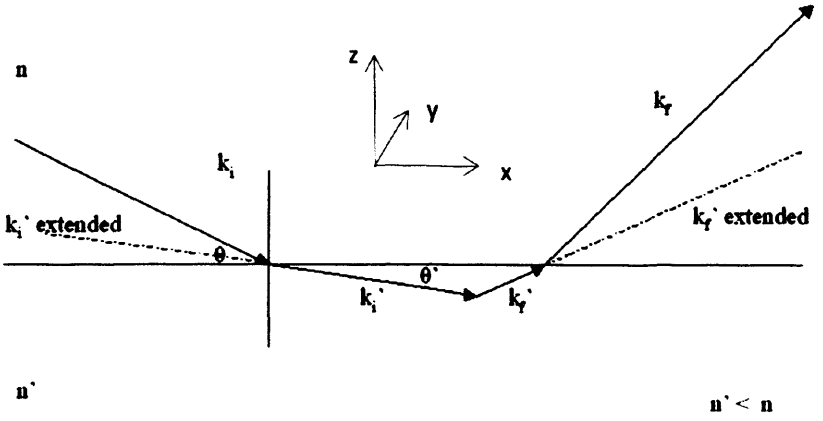

Figure 2.9 The path of a scattered x-ray beam as it passes into and out of the polymer film.

Figure 2.9 above is a diagram that shows that the scattering vector $\mathbf{Q}(\mathbf{k}_i-\mathbf{k}_f)$ is largely different inside and outside the thin film. The incident wavevector can be resolved into components along three axes x, y and z (x being along the sample in the same direction as the beam, y being perpendicular to x and still in the plane of the sample, and z being along the surface normal). If we first consider the wavevector $\mathbf{k}_i$ along z,

$$k_z' = nksin\theta'$$

$$k_z{}' = nk(1 - cos^2\theta')^{1/2}$$

$$k_z{}' = nk\left(1 - \frac{cos^2\theta'}{n^2}\right)^{1/2}$$

$$k_z{}' = k(n^2 - cos^2\theta)^{1/2}$$

using $n=1-\delta+i\beta$,

n^2 is approx equal to $1- 2\delta + i2\beta$, which makes

$$k_z' = k(sin^2\theta - 2\delta + 2i\beta)^{1/2}$$

..Equation 2.20

and similarly for the diffracted beam.

Algebra for the corrections along the x and y directions led to $k_x=k_x'$ and $k_y=k_y'$. This is due to the fact that the refractive indices in those directions are constant at any one time, unlike for z in which, at the interface, the refractive index is different along positive and negative directions. Using typical values for the critical angle and absorption effects the affect these considerations made to the values calculated in chapters 4 and 5 were within experimental errors and as such no corrections have been made to the data to incorporate this affect.

2.2 Polymers

The majority of the experiments outlined in this thesis investigate the structural ordering of various polymers. Polymers are materials that are composed of repeating atoms or groups of atoms linked together along a chain, and whose properties do not change drastically with the addition of an additional repeating unit. Apart from PET, the polymers investigated are liquid crystalline in nature.

2.2.1 Liquid Crystals.

The term Liquid Crystal (LC) is a loose description of this class of materials; they are never crystalline and only sometimes liquid. A better term is *"mesomorphic"* materials. The term is derived from the Greek, 'mesos' meaning 'middle' and 'morphe' meaning 'form'. Liquid crystals exhibit some properties typical of both liquids and of crystals, and therefore the term 'middleform' [9] is used. Liquid Crystalline materials are only LC in a certain temperature range, between the melting temperature, T_m and the 'upper transition temperature' where the LC phase reverts to an isotropic liquid [10]. Liquid crystals have long been used commercially. Initially coming to public recognition in the form of Kevlar, first synthesized and developed by Kwolek in the mid 1960's. More recently LC's have been used in TV displays [11].

2.2.2 Rigid rod polymers – Hairy rod polymers

The diffraction experiments in this thesis have been investigating the structure of two Rigid rod polymers, PQT-12 and F8. These are similar in that that have rigid backbones that have fairly long alkyl side chains. Without the side chains the rigid backbones have low solubility (making dissolving and spincasting difficult) and also have very high melting points (unsuitable for commercial use). They are called Hairy Rods because the side chains are highly flexible. Hairy rods are characterised by forming layers while in the LC phase, which is ideal if using x-ray diffraction to probe the structure.

2.2.3 Friedelian classes of LC

LC's can be split up into 3 types. These are nematic, cholesteric and smectic, first formulated by Friedel in 1922 [12]. The nematic phase possesses long range orientational order between polymer chains, but has no short range positional order. The smectic phase has many sub divisions but can be characterised by having short range order as well as orientational ordering. The last classification, cholesteric, is similar to the nematic phase but rather than the chains mutually aligning along a vector n. The chains have been twisted periodically perpendicular to n. Below is a figure representing all three cases.

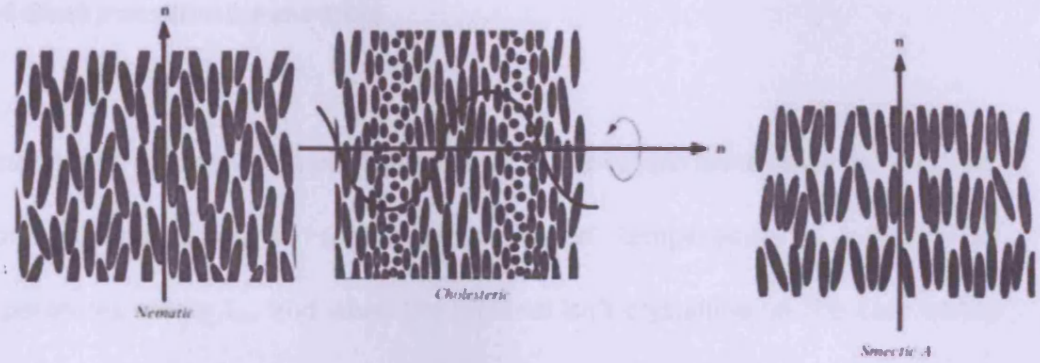

Figure 2.10 The three types of Friedelian classes, Nematic, cholesteric and smectic taken from reference [10]

Both the Nematic and Cholesteric phases will not produce a characteristic diffraction pattern. However as can be seen from Figure 2.10 the Smectic phase has a layered structure whose regular spacing will produce characteristic diffraction spots. Figure 2.11 shows a diffraction pattern realised from PQT-12 which is in the Smectic liquid crystalline phase.

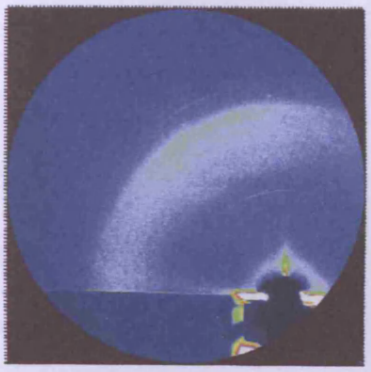

Figure 2.11. Diffraction pattern of PQT-12 which shows the characteristic diffraction pattern of a sample which contains the Smectic Liquid crystalline phase.

2.2.4 Glass transition temperature

As mentioned previously, LC phases can occur in the temperature range from T_m, the crystal melting point, to the upper transition temperature. However, at temperatures below T_m, and when the material isn't crystalline (in the case where the material has been quenched from a high temperature, or after deposition) the transition into the LC phase is called the glass transition. The glass transition temperature is defined as the temperature at which the material starts to increase its specific volume (volume per unit mass of material) from the "glass" state. The glass transition temperature for a given material is dependent on rate of heating and the time the material is held at temperature. For example, if the same material is allowed to cool at different rates, the respective specific volumes will be different and will also be reached at different temperatures. Therefore the glass transition is not a 'thermodynamic transition' as the final glass state is not in equilibrium[10].

2.2.5 Conjugated polymers

As well as being liquid crystalline the polymers investigated with x-ray diffraction are also conjugated. This means that there are alternating single and double bonds along the polymer backbone. The result of this arrangement is that the π bonds in the double bond overlap, allowing the electrons to flow, by a hopping motion, along the backbone. This property of conjugated polymers has led to much research into its commercial use as a low cost alternative to Si based devices. To be a useful

material, the conjugated polymer must not only have the alternating single and double bond but also a backbone that does not have large torsion angles at the bonds, which would reduce the delocalisation length of the electrons. The quality of the conjugation, and thus the conduction, is dependent on the persistence of the electron delocalization through the linking groups, and on the mutual planarity of the rings[10]. Though conjugated polymers are used primarily used in polymer electronics the electrical properties are not being investigated in this thesis [13].

2.3 AFM theory

The Atomic Force Microscope (AFM) was invented in 1986 by Binnig, Quate and Gerber[14], and since its conception the AFM has been an instrumental piece of equipment in scientific advancement in multiple fields.

The AFM is not a microscope in the traditional sense, where lenses are used to optically magnify the surface. It was developed so that an image of the surface could be made by using a sharp tip at the end of a flexible cantilever to scan across the surface using the short-range attractive forces, i.e. using van der Waals forces, to map out the surface.

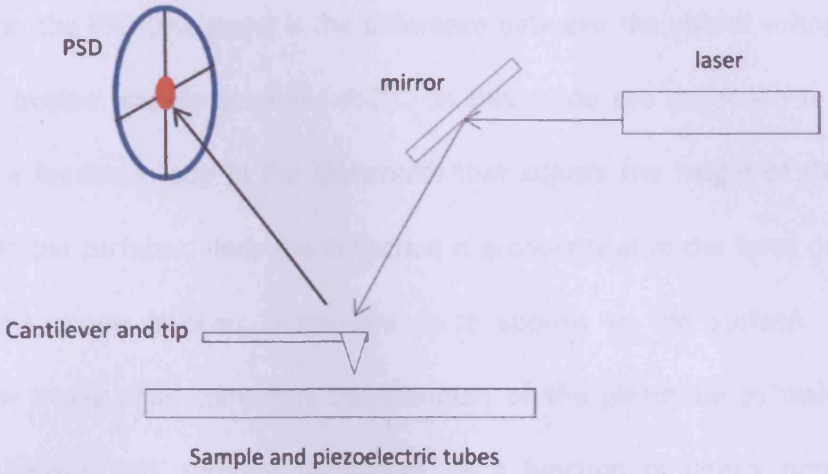

Figure 2.12 The basic set-up of an AFM.

Above is a picture showing the basic set up for an AFM. A laser shines a beam of light onto a mirror which directs the light down onto the cantilever which in turn reflects the light onto a position sensitive photodiode (PSD). The mirror can be adjusted so that while the cantilever is well above the sample surface the laser light hits the centre of the PSD. While the tip is brought down next to the surface (so that it "feels" the Van der Waals forces) the piezoelectric tubes on which the sample sits scans the sample underneath the tip making measurements of the deflection for each x,y postion, creating a topographical image of the surface. The piezoelectric tubes can be scanned on the picometre scale.

2.3.1 Contact AFM

"Contact AFM" is the simplest form of AFM. As the name suggests, in contact mode AFM, the tip is scanned across the sample surface while maintaining intimate contact. The deflection of the cantilever is detected by the position of the reflected

laser beam on the PSD (the signal is the difference between the output voltage of the top and bottom segments of the PSD). In this mode the deflection is kept constant by a feedback loop in the electronics that adjusts the height of the tip above the sample surface. Since the deflection is proportional to the force on the cantilever, this mode involves a constant force applied to the surface. The topographical image thus comprises the z-motion of the piezotube to maintain constant deflection (the setpoint deflection), as a function of lateral position. Though this is the simplest way to obtain an image of the surface, it is also the most invasive for soft materials, often leading to surface damage during the scanning process. Later in this thesis the AFM will be used to obtain topographical images of PET at temperatures above its melting point, which if contact AFM is used would affect the image and contaminate the tip. Therefore another mode of the AFM will be used, Intermittent-Contact AFM.

2.3.2 Intermittent-Contact AFM

Intermittent-contact AFM differs from contact AFM in that the tip is driven close to its resonant frequency causing it to oscillate a small distance above the surface, making contact with the surface intermittently at the lowest point of the oscillation. This method is obviously an improvement over the contact mode when scanning soft materials such as organic polymers. The motion of the tip is analogous to that of a driven, damped simple harmonic oscillator [14].

The tip is at the end of a cantilever that is attached to a piezoelectric driver in contact with the cantilever, leading to a displacement of

$$u = u_0 + aexp(iwt)$$

..Equation 2.21

and a tip position of

$$Z = z_0 + z$$

..Equation 2.22

where u_0 and z_0 are the rest positions of the attached end of the cantilever and the tip apex respectively, and z is the position of the tip apex of the driven cantilever (which is a function of time). The equation of motion for a driven oscillating tip free from external forces, as is the case when the tip is above the sample and out of range (to feel the long range attractive forces), is

$$m\frac{d^2Z}{dt^2} + \gamma\frac{dZ}{dt} + k(Z - u) = F_0$$

..Equation 2.23

where *z* is the displacement of the tip, *m* is the effective mass of the cantilever, *k* is the spring constant of the cantilever and γ is the damping coefficient. Substituting the two equations above makes equation 2.24

$$m\frac{d^2z}{dt^2} + \gamma\frac{dz}{dt} + k\big(z_0 + z - u_0 - aexp(i\omega t)\big) = F_0$$

.. Equation 2.24

Since the tip oscillates above the sample the restoring force can be expressed as $F_0 = k(z_0 - u_0)$ and equation 2.24 becomes

$$m\frac{d^2z}{dt^2} + \gamma\frac{dz}{dt} + k\big(z - aexp(i\omega t)\big) = 0$$

.. Equation 2.25

The oscillation of the tip will have the same frequency as the piezoelectric driver but may be out of phase depending on the frequency of the driver compared with the resonant frequency of the cantilever and tip. Therefore the vibration of the tip is given by

$$z = Aexp[exp(\omega t - \varphi)]$$

.. Equation 2.26

where A is the amplitude of oscillation and φ is the phase angle between the driver oscillation and the response of the tip. This equation can be substituted into equation 2.25 and A can be shown to be

$$A(\omega) = \frac{ak}{\sqrt{[(k - \omega^2 m)^2 + \omega^2\gamma^2]}}$$

.. Equation 2.27

This is the amplitude of the oscillation of the tip, and is dependent on the driving oscillation's amplitude and frequency, the spring constant and mass of the cantilever and tip, and the damping coefficient. This amplitude occurs when the tip is well above the sample. However, while the tip is closer to the sample, it is affected by

the Van der Waals forces. A similar calculation can be performed, but rather than force being uniform ($F=F_0$) there is a nonuniform interaction force $F = F(z_0) + \frac{\partial F}{\partial z}\delta z$ or an effective spring constant $k' = k - \frac{\partial F}{\partial z}$ and the amplitude of the tip can be expressed by

$$A = \frac{a\omega_0^2}{\sqrt{\left[(\omega'^2_0 - \omega^2)^2 + \frac{\omega^2\omega_0^2}{Q^2}\right]}}$$

.. Equation 2.28

where the resonance frequency in the non-uniform field is $\omega'_0 (=\sqrt{k'/m})$ and Q is the quality factor ($=m\omega_0/\gamma$). The amplitudes of the tip oscillation depend on the tip's height above the surface. A feedback loop is used to maintain constant oscillation amplitude (where the setpoint is the amplitude of the AC signal from the PSD). Other AFM modes employ alternative setpoint parameters such as the resonant frequency shift or the phase shift between the driving signal and the cantilever response, both of which are related to the cantilever damping coefficient.

2.4 References

[1] www-outreach.phy.cam.ac.uk/camphy/xraydiffraction/xraydiffraction5_1.htm

[2] http://www.xtal.iqfr.csic.es/Cristalografia/parte_11-en.html

[3] M. Kakudo & N. Kasai, X-Ray Diffraction by Polymers, Elsevier Publishing Company, 1972

[4] J. G. Brown, X-Rays and their applications, London ILIFFE Books LTD, 1966

[5] J. Als-Nielsen & D. McMorrow, Elements of Modern X-Ray Physics, Wiley, 2001

[6] R. James, The optical principles of the diffraction of x-rays, Ox Bow Press 1982.

[7] G. H. Vineyard, Physical Review B, 1982, 26, 4146.

[8] M. Born, E. Wolf, Principles of Optics, Cambridge University Press, 1999.

[9] U. W. Gedde, Polymer Physics, Springer 1995.

[10] A. M. Donald, A. H. Windle, Liquid Crystalline Polymers, Cambridge University Press, 1992.

[11] B. Ong, Y. Wu, P. Liu Proceedings of the IEEE, 2005, 93, 1412.

[12] G. Friedel, L Royer, Comptes Rendus Hebdomadaires Des Seances De L Academie Des Sciences, 1922, 174, 1523.

[13] W. R. Salaneck, S. Stafstrom, J. L. Brédas, Conjugated Polymer Surfaces and Interfaces, Cambridge University Press, 2003.

[14] G. Binnig, C.F. Quate, Ch. Geber, Physical Review Letters, 1986, 56, 930.

[15] H. Young, R. Freedman, University Physics, Addison Wesley publishing company, 1996.

CHAPTER 3 – GIXRD EXPERIMENTAL APPARATUS

3.1 Introduction

The majority of the work undertaken in this thesis concerns the ordering in thin films of semiconducting polymers studied with Grazing Incidence X-Ray Diffraction (GIXRD). In this chapter the design of the apparatus used in these experiments is described. GIXRD is a widely used technique and has been used in the study of thin film for many years. GIXRD experiments however have an intrinsic problem associated with them. At angles below the critical angle of the sample, the incident x-rays only penetrate ~ 50Å into the sample. The great majority of the x-rays incident on the sample are reflected, resulting in only a few of the incident x-rays being scattered by the sample, leading to a low intensity of scattered x-rays. This in turn results in low signal to noise ratios and the

need to have long exposure times to detect a sufficiently high number of scattered x-rays for analysis.

In addition to the inherent problem associated with GIXRD another problem arises due to the conjugated polymer films investigated being only 50-100nm thick, and relatively disordered. These characteristics of the films, and the fact that they also contain atoms of low atomic number, lead to scattering of low intensity.

An obvious solution to the problem of weak scattering is to use a high intensity incident beam. For this reason the GIXRD experiments were carried out at the ERSF, a source of synchrotron radiation.

3.2 The Beamline and ESRF X-Ray source

The ESRF has an 850m circumference storage ring that circulates electrons at an energy of 6GeV and a current of 200mA. The BM28 beamline used in this investigation had a 0.4 Tesla dipole magnet on the storage ring. The beamline uses two Si (111) crystals as a monochromator, whose angle can be changed to produce x-ray beams with an energy range of 2.3 – 15keV. Our experiments were carried out between 5.5 and 9keV, which produced a high intensity beam of ~ 10^{13} photons/sec. The beamline uses an 11-axis Huber diffractometer which facilitates operation in both vertical and horizontal scattering geometries. This diffractometer does however put a limit on the size of the sample chamber which can be built. This will be clarified later in the chapter. At the

centre of rotation of the diffractometer, which is aligned to coincide with the maximum focus of the beam, the beam cross section is approximately 0.8x0.2mm. While the beam dimensions can be reduced further by the use of slits, these cannot be situated close to the sample, and an additional pair of slits is required downstream to cut out the scattering from the slit edges.

3.3 Design of the sample Chamber

Even with this high flux beamline, however, the scattering from the samples is still relatively weak compared with the background scattering. It is important therefore to reduce the background levels as much as possible. The background scattering arises from any material in the beam, such as windows, slits and air-paths. One can easily gauge the extent of the problem in that we are typically measuring the diffracted signal from a 50nm thick polymer film whereas the window into the sample chamber is 10μm thick polymer film. Even an air-path of 0.15m causes stronger scattering than the polymer sample. There are three obvious solutions to this problem:-

a) reduce the path length of the x-rays through the air outside the sample chamber;
b) mount the sample in a chamber having an inert gas atmosphere, which does not absorb or scatter x-rays; and
c) introduce shielding at strategic points to intersect and absorb unwanted scattering from objects such as windows, slits or air gaps.

These three solutions were incorporated into our design.

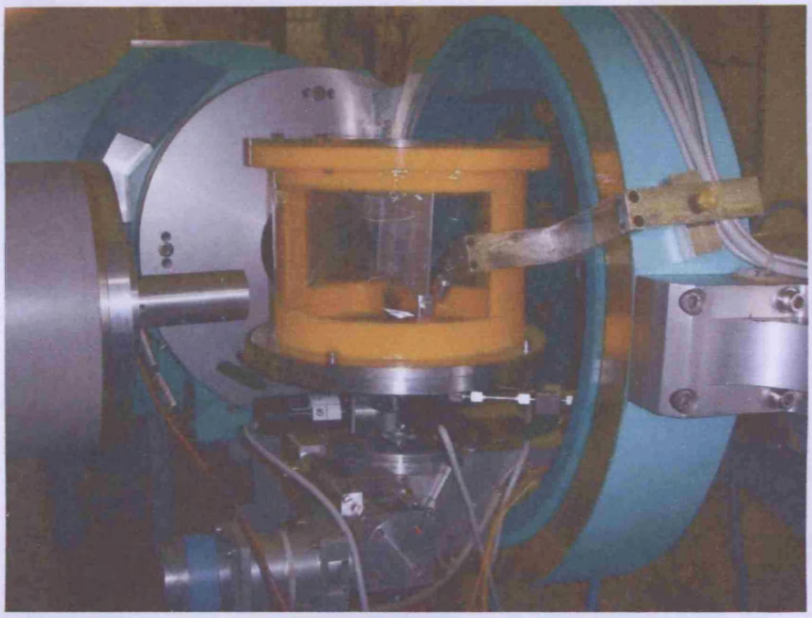

Figure 3.1: The chamber sitting on the 11-axis diffractometer at the ESRF

Figure 3.1 shows the experimental apparatus that we used while taking measurements on the beamline. A detailed description of the design forms the remainder of this chapter.

3.3.1 The chamber

As mentioned above, one way to reduce the background scattering is to reduce the path length of the x-rays through air. This is partly achieved by mounting the sample in the sample chamber, of diameter 250mm (significantly greater than the sample size), and filling it with an inert gas of low atomic number to minimise the scattering from the gas, or by evacuating the chamber to remove the air. Other beamlines, available at the ESRF, such as the ID1 beamline, have the sample holder, detector and x-ray source in

chambers that can be evacuated. These beamlines are extremely effective in reducing the background scattering, but the chambers are very large and take a long time to be evacuated. With limited time allocation and multiple samples, a different design of sample chamber was needed. The chamber illustrated in figure 3.1 is large enough to have a flight path that gives a high angular resolution.

The chamber itself consists of three main parts:

i) The Perspex lid which allows easy access to the sample stage;

ii) The base which allows the chamber to be attached to the diffractometer and holds the helium inlet and outlet together with electrical feedthroughs; and

iii) The middle section which comprises large apertures that allow x-rays to pass through.

All three sections are assembled with nuts and bolts, with o-rings to keep the chamber air tight. The chamber also includes a sample stage and shielding. These will be discussed later in the chapter.

The middle section was constructed from a plastic industrial gas pipe. Two large windows were cut out from either side enabling the incident x-rays to enter the chamber and scattered x-rays to be detected by the detector outside of the chamber. The exiting window had to be as large as possible to enable the greatest angular range of Q be detected. Additionally, to enable the chamber to be either evacuated or filled with helium, these windows had to be "glazed" with a material that is strong enough to keep the chamber airtight but would not scatter the x-rays. Kapton was used for this

purpose. We had originally thought of using a beryllium dome, as the chamber would have the advantage of being evacuated, but soon discovered that it was far too heavy for the necessarily small goniometer used. Kapton is not entirely transparent to x-rays and requires shielding to restrict x-rays scattered by the Kapton from reaching the detector. The design of this shielding will be discussed later.

The base of the chamber was made of Aluminium. This was the heaviest part of the chamber, and sections of the base had to be machined to be as thin as possible to minimise the weight of the chamber, which was to be mounted on a Huber goniometer. In order to attach the goniometer to the chamber base, a mount was needed. Due to the weight of the chamber the mount had to be secure enough not to slip away from the goniometer while the diffractometer was moving. Also, due to the motors of the goniometer arcs and the gas valves, which were required to supply a pressure of helium, the mount has limited access. Two bolts attach the mount to the base of the chamber. The threaded holes tapped into the base did not go all the way through the base plate into the chamber. This ensured that the only gas entering the chamber was through the inlet valve. This was also true for the sample holder in the chamber.

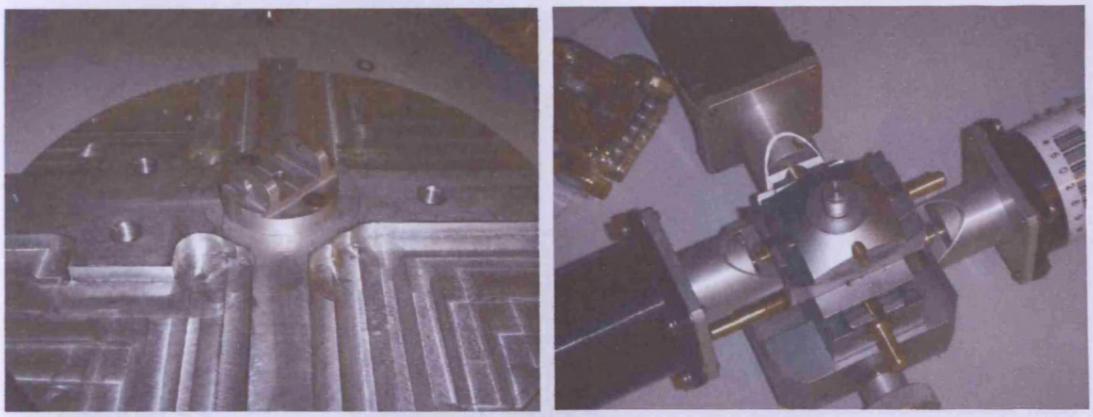

Figure 3.2: The chamber base and the goniometer that attaches it to the diffractometer. Sections of the base have been machined away to minimise the weight of the chamber.

Two horizontal holes were made either side of the mount, one of which allowed access to the goniometer key, the other tapped to allow a grub screw to clamp the mount onto the goniometer.

3.3.2 The shielding

i) from the front kapton window

As previously stated, Kapton isn't entirely transparent to x-rays, and so causes scattering of the incident x-rays from the windows. To maximise the signal to noise ratio of the scattering from the samples, the scattering from the Kapton windows must be minimised, and every design effort was made to restrict the unwanted x-rays scattering from these windows being detected, so to make the weak scattering from the ordering in the films dominant.

To prevent scattering from the x-rays passing through the front window from being detected, shielding was placed all around the sample holder.

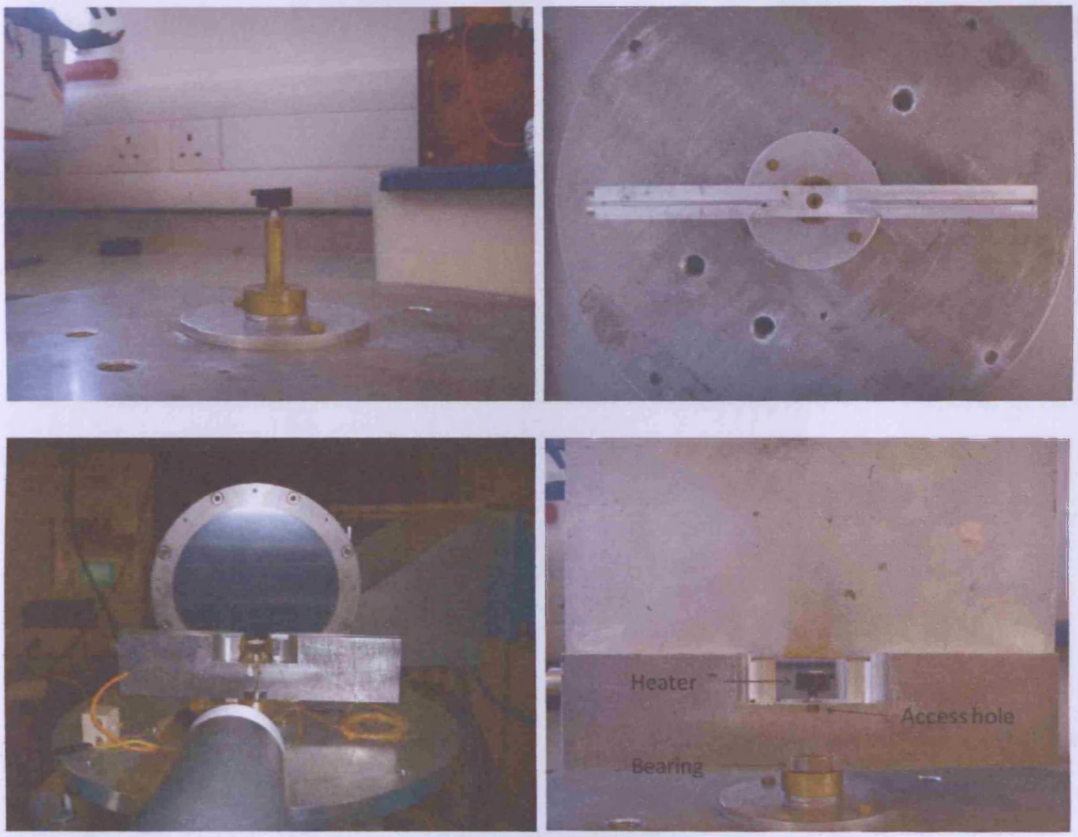

Figure 3.3: Different stages of the mounting of the shielding used to minimise the effect of unwanted scattering from the front window reaching the detector. The shielding is in two parts to allow the sample to be mounted in-situ.

The four images displayed in figure 3.3 show the stages at which the shielding is placed around the sample in order to ensure maximum shielding and a maximum signal to noise ratio. The sample is positioned on the black heater shown. The shielding has been designed in two halves. The lower half has a central hole allowing it to be placed over the sample mount. The heater pin can then be placed into the end of the sample mount

and held by a grub screw, access to which is possible through a small hole in the shielding. The lower shielding also has a bearing at the bottom, allowing the whole shielding assemble to rotate. A groove has been made along the upper side of the shielding to allow the upper shielding to sit on top after a sample has been attached to the heater.

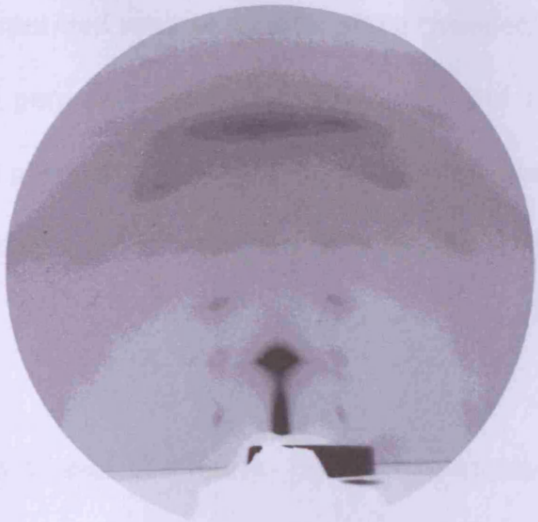

Figure 3.4: A diffraction pattern illustrating shielding effectiveness. The intense area at the bottom of the image is due to x-rays scattered by the Kapton front window passing through the gap in the shielding surrounding the sample.

The effectiveness of the shielding can be seen in figure 3.4, a diffraction image from a sample of F8. The dark area at the bottom is an area of high intensity x-rays. These x-rays have been scattered from the front Kapton window and passed through the gap around the sample. Without the shielding similar rays would have been detected all over the detector and it would not have been possible to resolve the weak sample scattering.

ii) The shielding in phi rotation

In this investigation we were not interested in rotating the sample and holder. However, a collaborating group from Hull University were studying the effect of substrate alignment on the orientation of the film. Therefore another chamber specification was incorporated to allow rotation of the chamber, and the sample, while keeping the shielding perpendicular to the x-ray beam. For a sample in which the molecular backbone is preferentially aligned, the scattering varies with azimuthal angle, the contrast being strongest when the alignment is parallel and perpendicular to the x-ray beam.

The diffractometer has 11 axes of rotation. The required rotation is carried out on the phi circle independently of the chi circle. The image below shows a clamp that attaches to the chi circle. A magnet was attached to the end of the clamp. At the end of the shielding, within the chamber, another magnet was attached. The attraction between these two magnets kept the shielding in the plane perpendicular to the beam while the sample (and chamber) was rotated. Without the magnets the small amount of friction would have caused movement of the shielding.

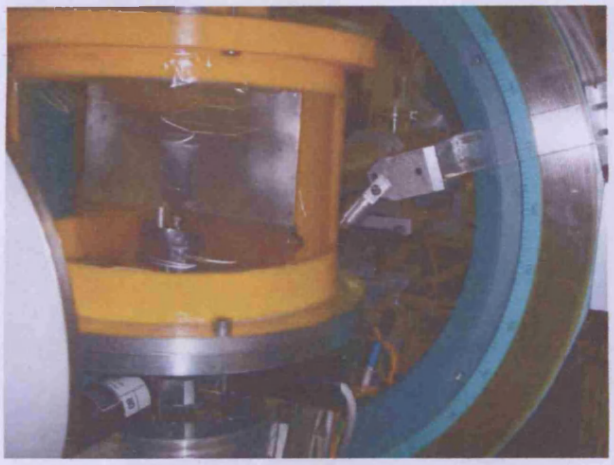

Figure 3.5: The phi rotation clamp allowing the shielding to remain stationary with respect to the beamline as the sample and chamber rotates

The whole chamber could rotate by only 110 degrees. This was due to wires from the heater coming into contact with the shielding and restricting any further rotation without moving the shielding. This was not an issue though because before this could occur the vertical supports on the side of the middle section of the chamber intercepted the path of the diffracted x-rays to the area detector.

iii) the rear beam stop.

Most of the x-rays that pass into the chamber aren't scattered at all and pass straight through. Thus the intense direct beam strikes the back Kapton window of the chamber. A beamstop must be placed immediately after this window firstly to stop scattering from this point reaching the detector and secondly to protect the detector from the unscattered x-rays whose intensity is much greater than the scattered x-rays from the sample. This beamstop could not be attached to the chamber because the chamber is

rotated relative to the direct beam. Instead, the beamstop was mounted on a motorised x-z translation stage, which in turn was mounted on a stationary part of the diffractometer.

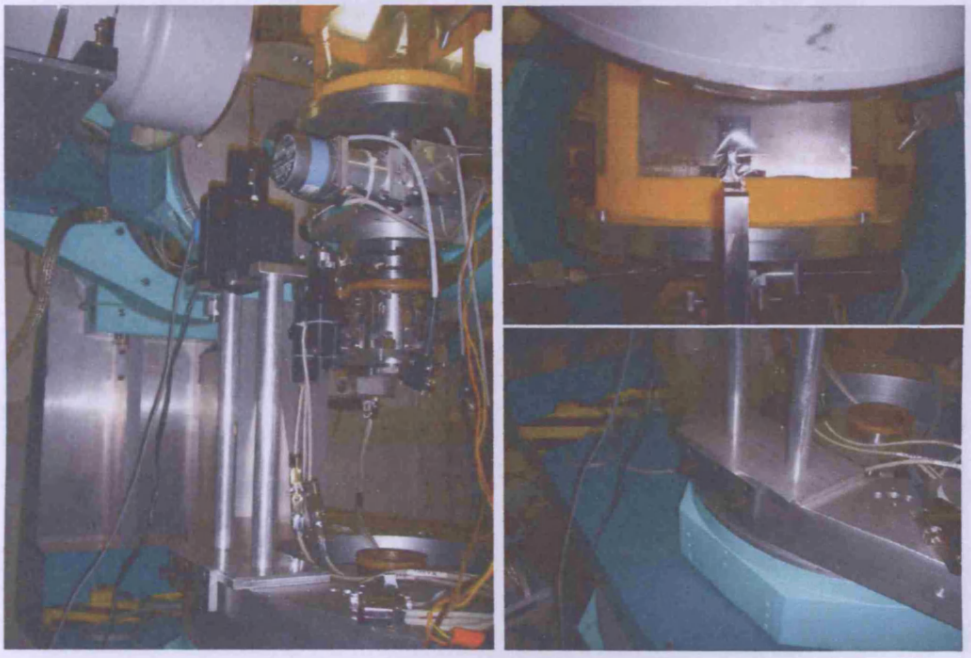

Figure 3.6: Shielding from the rear beam stop to shield the area detector from unscattered x-rays.

3.4 The in-situ heater

The final feature of the experimental apparatus is the sample holder, which incorporates a heating stage. The heater enabled structural changes to be followed *in-situ* during annealing.

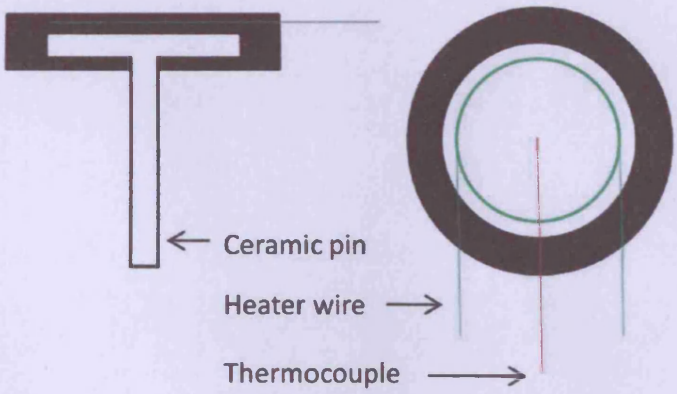

Figure 3.7. Side and top view of the heater used for *in-situ* heating

The heater design is show in Figure 3.7. It consists of a ceramic pin that is surrounded by thermally setting epoxy resin. Within the epoxy, lying above the ceramic pin, a wound insulated heater wire and a thermocouple are positioned just below the surface. The heater wire is wound to increase the length and resistance of the wire that lies within the epoxy. The ceramic pin allows a high temperature gradient between the sample and the heater holder (seen in figure 3.3). A PTFE mould was machined so that the heaters could be easily fabricated. This heater design was modified for the compact heating stage built for the Veeco Multimode Scanning Probe Microscope which is described in chapter 6.

CHAPTER 4 – STRUCTURE DETERMINATION OF F8

4.1 Introduction

Conjugated polymers have been widely investigated in the last few decades due to their potential for display and transistor-based devices as a consequence of their semiconducting nature. A particularly attractive feature is that their solution-based processing is suitable for coating large areas cheaply. They have been used in such devices as organic solar cells [1] and LCD television screens [2]-[5].

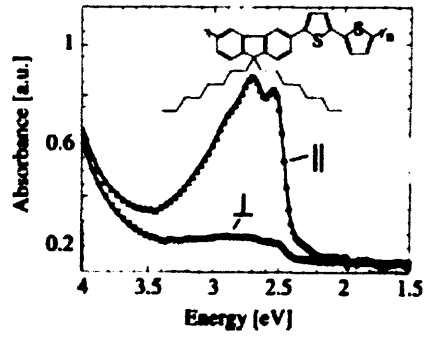

Figure 4.1. The affect of alignment of LC semiconductors on carrier mobility[6]

As is seen in the figure 4.1 the carrier mobility has been shown to increase considerably as the molecular alignment is improved [6]. This has led to considerable effort by various research groups to try to align the molecules within the films, using various approaches such as brushing the top surface of an alignment layer prior to spin coating of the semiconducting layer [6]-[8], and photo alignment [9]-[11]. Liquid crystalline polymers are attractive to organic electronics as the polymers transfer the alignment of underlying layers into the polymer film due to inter-molecular interactions[6]-[11]. While it might appear that the molecular alignment can be further improved in the crystalline phase rather than in the liquid crystalline phase, the grain boundaries that are formed around crystalline domains scatter carriers and will often trap charge [12].

Despite their technological significance, no detailed structural models exist for the molecular arrangement in conjugated polymers. Such knowledge is fundamental to detailed modelling of inter-molecular conduction. Diffraction studies in the liquid crystalline phase are severely limited by the small number of diffraction peaks, making detailed structural analysis impossible. Structural analysis of crystalline phases is made easier by the larger number of measurable diffraction peaks, and these may shed light on the molecular packing in the liquid crystalline phase. This chapter describes an attempt to model one such structure for one conjugated polymer, poly(9,9-di-n-octyl-2,7-fluorene), known as F8, commonly used as a light-emitting polymer either in its pure form or as a copolymer. The broader issues involved in this study, exemplified with this specific polymer, are:

- the requirement for detailed models of molecular packing in conjugated polymers.
- structural analysis in a thin film geometry, universally used for polymer devices, for which a grazing incidence geometry is most well-suited
- the use of an area detector to speed up data collection and hence to minimise beam damage, which is relatively rapid in these materials. The weak scattering and open detector geometry constitute a particular challenge for grazing incidence diffraction.
- the effect of the surface on molecular orientation: F8, in common with other conjugated polymer materials we have studied, aligns in a layered geometry normal to the surface and in an isotropic polycrystalline ordering in the plane of the surface.
- the large unit cells of low symmetry require many diffraction peaks for structural analysis. As will be seen later, the number of crystalline peaks observed is still relatively small, and hence some structural constraints need to be included in the model.

The conjugated polymer studied in this chapter, F8, belongs to a group of polymers called polyfluorenes. As a group these polymers were introduced in the late 1990's and have received much attention ever since[13]-[19]. In general all PFO's have been shown to have good electron mobilities (typically $2.0 \times 10^{-4} - 1 \times 10^{-3}$ $cm^2/(V.s)$) [20] and have long device lifespans due to their excellent thermal and chemical stability[15]. Along with these advantages, these materials can be deposited onto a

substrate to form thin films, making commercial exploitation viable. F8 has received more attention because, upon heating, mesomorphic and crystalline phases are realised [15]. The mesomorpic phase has been shown to contain three distinct sub-phases. These three phases, known as the α, α', and β phases, are formed from different cooling cycles from temperatures above T_m [15]. As mentioned above, working devices use F8 in the LC phase. However, in this chapter the structure of the thin film, when the F8 is in the α phase is investigated to assist in the understanding of the conduction within these devices.

Another important property to consider when investigating the structure of a thin film that will be used in an electronic device, is the roughness of the free surface. Electrical contacts are sometimes deposited onto the surface after the material has been subjected to a heating process. In this chapter we also investigate the affect the heating process that produces F8 with a high degree of α crystallites has on the free surface. This is conducted by means of imaging the surface with an AFM after different annealing temperatures.

4.2 Sample preparation

The F8 used in these investigations was prepared by Prof M L Turner, University of Manchester, and had a molecular weight of 102 kamu. For the x-ray diffraction experiments, samples were prepared with 10mg/ml solutions of F8 in toluene, spin-coated at 2000rpm onto a native SiO_2/Si substrate. Prior to spin coating the SiO_2 was

cleaned using acetone, followed by Isopropyl alcohol to remove any impurities on the surface. Due to this relatively high concentration the solution was heated to 50°C to encourage dissolution. This concentration led to a film thickness of approximately 50nm, as measured by scratching the surface of the sample and measuring the depth of the scratch with the AFM. After spin coating, the samples were heated to 50°C for 2 hours to evaporate any remaining toluene. As mentioned in the introduction, the three phases known within the mesomorphic phase can be achieved by different cooling cycles. The α phase sample was produced by heating to above its melting temperature T_m into a nematic phase and then cooled at 1^0C/min to 170°C, and then quenched to room temperature to freeze in the nematic phase. After quenching, the sample was then heated at 140°C for an hour to crystallise it, and quenched again. Crystallisation from the quenched nematic phase leads to a greater order than from the more disordered as-spun orientation. The other two phases that have been shown to exist are the α' and β phases[15]. Already published x-ray diffraction data for these three phases can be seen below in figure 4.2.

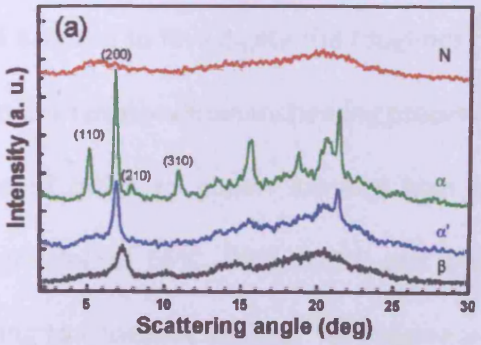

Figure 4.2. X-ray diffraction sections for each of the three distinct sub-phases taken from [15].

This investigation concentrates on the ordering of the α phase. Cooling at a steady rate, rather than quenching, produces samples that contain a high degree of α' crystallites, but these samples retain more of the nematic phase between the crystalline domains, hence this mixed phase was avoided. During the investigation it was necessary to heat the sample in-situ using the heat process outlined above. This process leads to a sample that is high in the α phase. However, due to the sample being mounted on a small heater with finite heat capacity within the chamber, described in chapter 3, instantaneous quenching from 170°C to room temperature was not possible: the current was switched off and it took approximately 90 seconds for the temperature to drop below T_g. This led to some crystalline peaks being formed in the diffraction pattern following the quenching from the nematic phase. Following crystallisation, these peaks were more intense and in the same position prior to and after annealing. Comparison of the intensities of the in-situ annealed samples with the ex-situ annealed samples showed that the in-situ annealed samples contained α phase crystallites, with no discernable α' phase peaks.

The samples which will be used to investigate the roughness of the top free surface have been subjected to the same preliminary heating process as the samples used in the diffraction studies in order to obtain samples high in the nematic phase. Samples were then annealed at 65°C, 90°C, 115°C and 140°C for two hours and quenched by transferring to a metallic surface. All imaging was carried out at room temperature in ambient conditions.

4.3 Determination of the size of the unit cell

4.3.1 Calibration of the area detector

The unit cell parameters were determined from 1-D intensity profiles extracted from 2-D area detector images, mainly those with scattering vectors of Q_z=0 or $Q_{//}$=0 as shown in Figure 4.3.

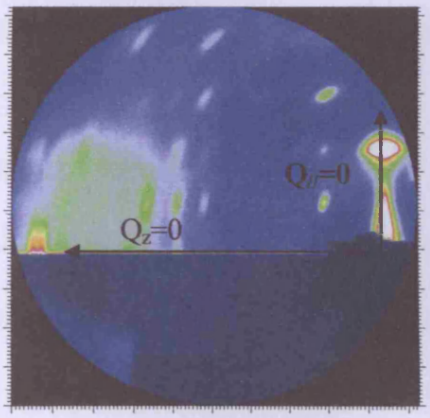

Figure 4.3 Area detector image of F8 showing the 1D sections along the in-plane and out-of-plane directions, used to calculate the unit cell parameters

Peak positions on the area detector image or in the 1-D profiles were converted into a scattering vector Q using a straightforward calibration and conversion procedure. Figure 4.4 shows a schematic of the beam position on the area detector at different stages of the calibration process.

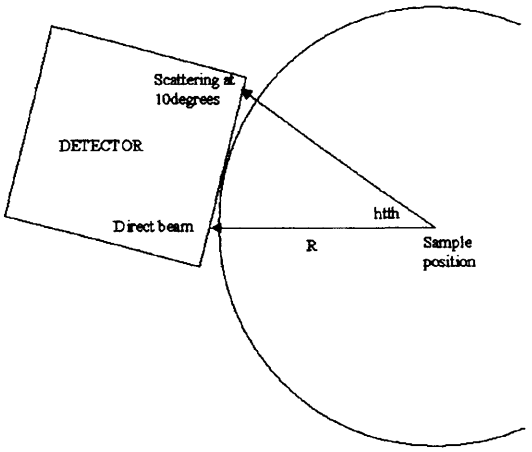

Figure 4.4 Calibration of the pixels on the area detector to convert pixel values to scattering angles, and subsequently into the magnitude of a scattering vector.

The pixel position of the direct beam on the area detector was monitored at the start and end of the experiment with the detector arm positioned at (htth=0°, vtth=0°) and (htth=10, vtth=0), where htth and vtth are angles subtended by the detector arm horizontally and vertically respectively. When the detector is at htth=vtth=0 the path of the direct beam is perpendicular to the surface of the detector, and at all other values of htth and vtth the scattered beam incident on the centre of the detector is perpendicular to the detector. Using simple geometry the distance of the area detector from the sample in pixel units, R, can be calculated using $\tan(10°)=\frac{PX_{10}-PX_0}{R}$, (and similarly for PY). The scattering angle, 2θ, corresponding to any general pixel position (PX, PY) at a general diffractometer setting (htth, vtth) can then be determined using the equations $\frac{PX-PX_0}{R} = \tan(htth-2\theta_h)$ and $\frac{PY-PY_0}{R} = \tan(htth-2\theta_v)$. The right angled triangle set up by the x-ray beam in relation to the area detector at 0° and 10° is shown in figure 4.5.

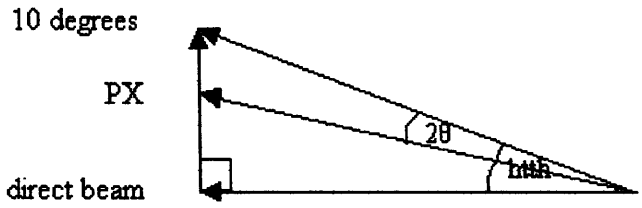

Figure 4.5 Converting pixels on the detector into scattering angles

The **Q** values corresponding to these 2θ values can then be determined using equations 4.1.

$$Q_z = k(\sin\alpha_i + \sin\alpha_f)$$

$$Q_x = k(\cos\alpha_i - \cos\alpha_f \cos 2\theta_h)$$

$$Q_y = k\sin 2\theta_h$$

$$\text{and } Q_{in\text{-}plane} = (Q_x^2 + Q_y^2) \qquad \text{..Equations 4.1}$$

4.3.2 Profiles selected to calculate the lattice parameters

The intensity profiles shown in figures 4.6 were converted from pixel units to scattering angle 2θ, corrected for refraction effects, as explained in chapter 2, then converted to the magnitude of the scattering vector Q in order to search for regular spacing in the intensity maxima, to infer unit cell parameters. Figure 4.7 shows the intensities profiles after pixels have been converted to the magnitude of the scattering vector, Q.

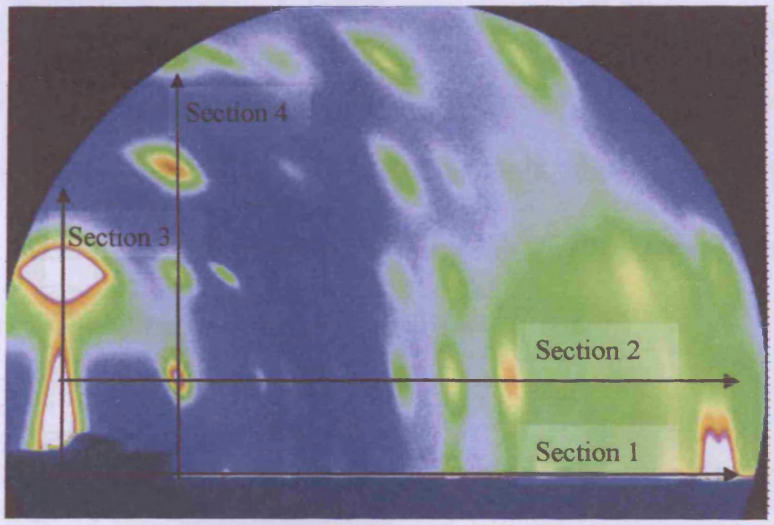

Figure 4.6 Area detector image indicating sections used to determine unit cell parameters. Sections 1 and 3 are sections that would conventionally be used in experiments involving point detectors, and sections 2 and 4 are additional sections that were vital in determining the unit cell parameters.

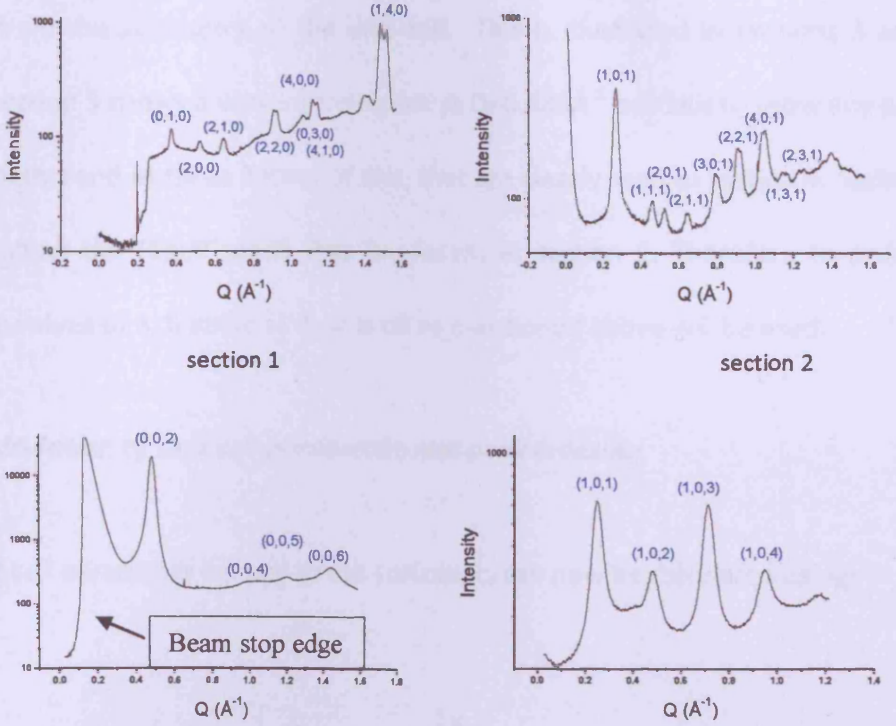

Figure 4.7 The line profiles for the corresponding sections from figure 4.5

A beam stop has to be placed in front of the area detector to prevent the direct x-ray beam damaging the detector. The sharp increases seen at the start of section 3 is due to the edge of the beam stop. For the remainder of the chapter I will refer to the peaks by their indices (*h,k,l*), where *h* and *k* are the Miller in-plane indices and *l* is the Miller out-of-plane index. The indexing is discussed later.

One advantage of using an area detector is that images can be taken of large areas of reciprocal space without being restricted to in-plane and out-of-plane directions. As well as being able to observe extra peaks, area detectors also enable both peak positions and peak intensities to be determined simultaneously.

In indexing the diffraction peaks, care must be taken regarding systematic absences arising from the symmetry of the unit cell. This is illustrated in sections 3 and 4 where section 3 shows a very intense peak at Q=0.483Å^{-1} but fails to show any peaks at half of this and at three halves of this, that are clearly seen in section 4. Section 1 fails to show the (1,0,0) peak that is present in section 2. Therefore to produce accurate values of **a**, **b** and **c** all four profiles mentioned above will be used.

4.3.3 Calculation of Unit cell parameters and peak indexing

The unit cell parameter normal to the surface, **c**, can now be calculated using:-

$$c = \frac{2\pi}{Q_l - Q_{l-1}}$$

...Equation 4.2

To reduce the errors introduced by the limited number of pixels on the detector, and by the subjective judgement of where the peaks centre is, an average of spacing between adjacent peaks of Q=0.230 (±0.002) $Å^{-1}$ is used. This gives a value for the unit cell parameter, **c** of 27.3 ± 0.3 Å.

Calculation of the in-plane unit cell parameters is harder to determine because of there being two parameters to determine. As mentioned earlier, this task is made easier due to the advantage of having images covering a large area of reciprocal space, which enables detection of the (*h,k,l*) peaks where $l \neq 0$. Section 1, along (*h,k*,0), has strong peaks at Q=0.377 and Q=1.111 (±0.002) $Å^{-1}$ arising from (0,1,0) and (0,3,0) orientations, and resulting in the unit cell parameter, **b** of 17.1 ± 0.2 Å. The third unit cell parameter was calculated from peaks at Q=0.265 and Q=0.781 (±0.002) $Å^{-1}$ in section 2 attributed to indicies of (1,0,1) and (3,0,1) respectively, and resulting in the second in-plane unit cell parameter, **a**, of 24.3 ± 0.3 Å. Other in-plane peaks in both section 1 and section 2 can be indexed using these calculated values, and having an angle, γ^* of 88.6 ± 1.2 degrees between $\mathbf{a}^*$ and $\mathbf{b}^*$ which was found to be consistent with the peak positions using the equations:-

$$\boldsymbol{Q} = h\boldsymbol{a}^* + k\boldsymbol{b}^*$$

...Equation 4.3

$$\boldsymbol{Q}^2 = h^2\boldsymbol{a}^{*2} + k^2\boldsymbol{b}^{*2} + 2hk\boldsymbol{a}^*\boldsymbol{b}^* cos\gamma^*$$

...Equation 4.4

The unit cell parameters were calculated from analysis of the four sections illustrated in figure 4.7. However there are many more peaks seen in the diffraction pattern illustrated in figure 4.6. Using these calculated parameters it is possible to predict check our unit cell parameters to see if the calculated positions fall upon these extra peaks seen. Figure 4.8 is the same image diffraction pattern seen in figure 4.7 with red circles positioned where diffraction spots are believed to be seen.

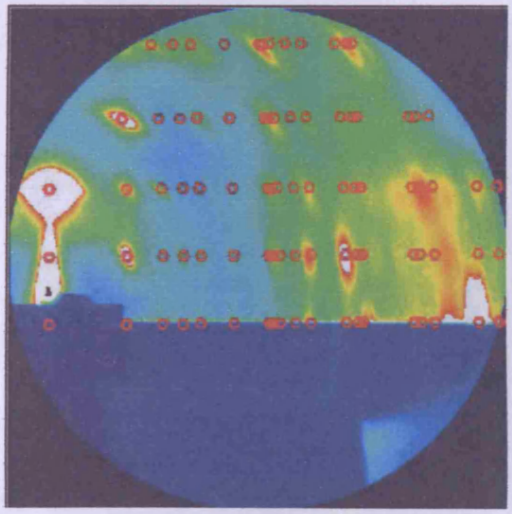

Figure 4.8. The diffraction image seen in figure 4.6 with projected diffraction spot positions calculated from the unit cell **a**=24.3Å, **b**=17.1Å and **c**=27.3Å.

In the whole the majority of the calculated positions correspond with a diffraction spot. The calculated positions where no diffraction spot is seen can be explained as crystallographic reflections which lead to a structure factor of, or close to, zero.

As discussed in chapter two, the positions of the diffracted peaks are determined by the size of the unit cell, and the positions of the atoms within the unit cell determine the intensity of each of the diffracted peaks.

4.3.4 Calculation of (hkl) intensities

In all techniques aimed at determining the atomic structure of the unit cell, an accurate measurement of the intensity of each of the (*h,k,l*) peaks is required.

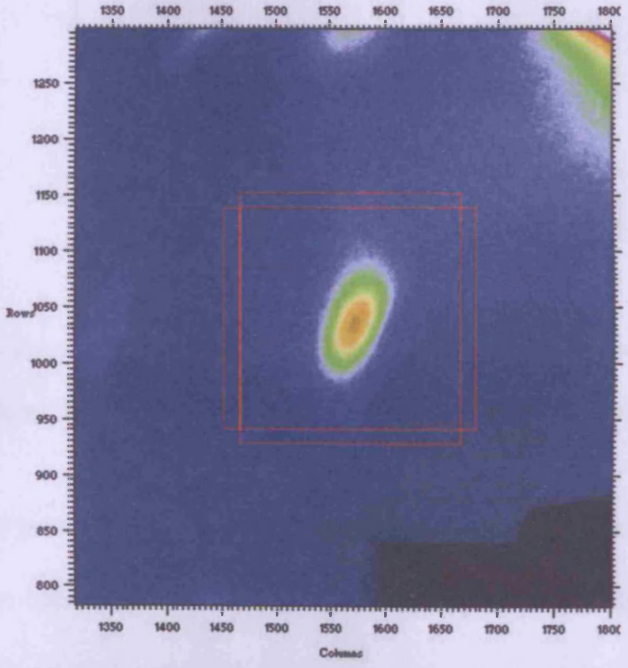

Figure 4.9. A (*hkl*) peak enclosed in a box, the summation of the intensities of the pixels within the box minus the background intensity on which the peak is portrayed equates to the scattering intensity for that given (*hkl*) peak that can be compared with the other measured (*hkl*) peaks.

Figure 4.9 shows a section of the area detector which contains the (1,0,1) peak. In order to obtain an accurate measurement of the intensity, a good value for the background intensity is paramount. A section was taken across the peak along the x axis of the detector and the y axis of the detector. Figure 4.10 shows the section along the y axis (top to bottom through the centre on the image above).

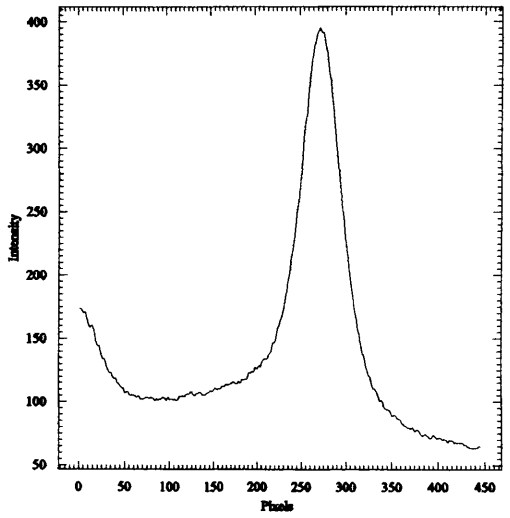

Figure 4.10. A section through the peak illustrated in figure 4.8 to help determine the extent of the peak, so that the position of the background measurement can be made.

A similar section is seen along the x axis. Once these sections have been taken, a number of steps are taken to obtain a calculated intensity for each individual peak:-

- Starting and end points of the sections along x and y axis are decided upon so that the whole peak is encompassed within these points.
- These values then form coordinates for the box around the peak on the area detector.

- Smaller boxes which have a width of 10 pixels are drawn around each side of the box, and are used to calculate the background intensity.
- The average intensity of each pixel within these background boxes is subtracted from each pixel within the box encompassing the peak, and the total remaining intensity is attributed to scattering from the peak.

The determination of the exact value of the background level is very important in calculating the intensity of the peak. Each calculated value of peak intensity was subjected to further checks. If the calculated value is valid, then slightly changing the size of the peak's box shouldn't affect the total intensity. Therefore, the size of the box for each of the peaks was varied in the x and y direction independently, and recalculated to see how the recalculated value differed from the original calculation. This process was repeated until the calculated intensity was constant over a range of box sizes. This intensity was taken as the (*h,k,l*) peak intensity. A larger uncertainty occurs at higher orders of (*h,k,l*) due to peaks being close enough together in **Q** to often overlap, making background determination almost impossible.

The final point to consider in evaluating these peak intensities is that the less intense peaks are not considerably larger than the background, leading to a larger percentage error in peak intensity evaluations.

4.3.5 Geometrical corrections to I(h,k,l)

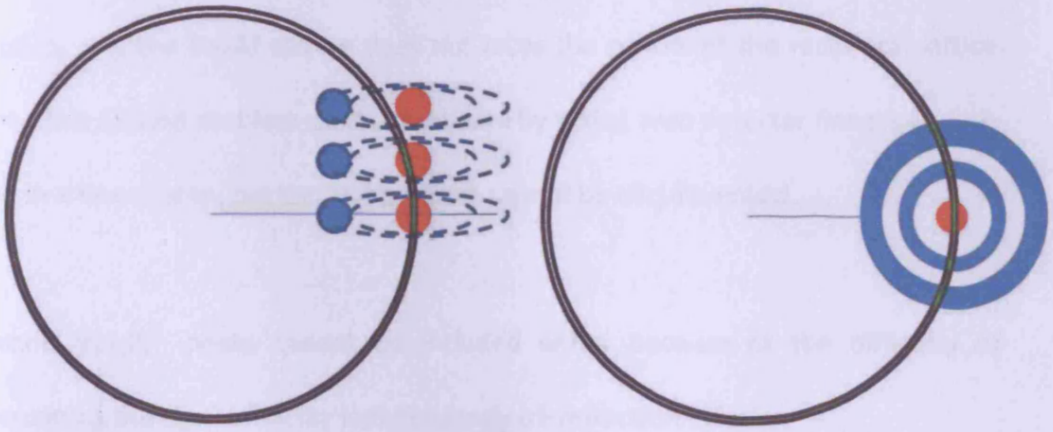

Figure 4.11. Side and plan view of the Ewald Sphere

The integrated intensities must be corrected for geometrical effects. For crystalline polymers, such as F8, we observe isotropic polycrystalline rings in the plane of the surface, whereas the ordering is layer-like normal to the surface. The corresponding Ewald sphere construction is shown schematically in Fig 4.11 in side view and plan view. Red spheres denote specular (0,0,*l*) peaks, and the blue tori denote non-specular rings in reciprocal space. The finite thickness of the Ewald sphere, arising from the wavelength spread $\Delta\lambda/\lambda \approx 10^{-4}$ is also indicated. The intersected volume in reciprocal space for the non-specular peaks is dependent on the wavelength spread and the width of the polycrystalline rings (dependent in turn on the domain size). Different non-specular peaks can be normalised by considering the intersection of the polycrystalline rings with the Ewald sphere. This intersected volume is proportional to $[\cos(\alpha_v)\sin(\frac{180-\alpha_h}{2})]^{-1}$, the domain size and wavelength spread being the same for all *h,k* values.

However, specular (0,0,*l*) peaks cannot be normalised using this factor for two reasons. Firstly all the polycrystalline domains contribute to the peak. Secondly, unless $\alpha_f = \alpha_i$ the Ewald sphere does not cross the centre of the reciprocal lattice point. This second problem can be overcome by taking area detector images at each point in a fine α_i scan, but the first problem cannot be circumvented.

In-plane (*h*,*k*,0) peaks cannot be included either because of the difficulty of determining the $\mathbf{Q_z}$=0 intensity independently of refraction effects.
These considerations imply that one can only include (*h*,*k*,*l*) peaks with *l*>0 and with *h* or *k* being non-zero in a dataset for structural analysis.

Apart from this Ewald sphere consideration, there are also corrections to be made due to the polarization of the synchrotron source and also the sample illumination. The polarization correction is due to the fact that electrons within the synchrotron ring are accelerated in the horizontal plane. This results in a polarization factor

$$P = cos^2(2\theta)$$

...Equation 4.5

where 2θ is the scattering angle between the incident and diffracted beam horizontally. There is no polarization correction for the vertical component of the diffracted wave.

The sample illumination correction is due to the dimensions of the incident beam of x-rays.

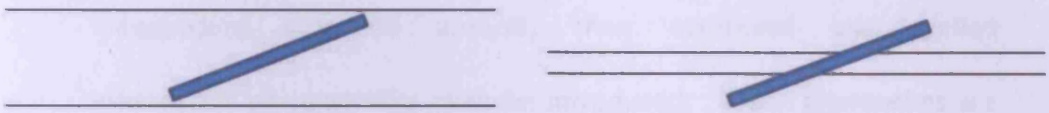

Figure 4.12: Sample illumination, where the beam is larger and smaller than the sample

In the case where the beam dimensions are larger than the sample dimensions, there is no correction. When the beam only illuminates a fraction of the sample surface then the illumination correction is $1/sin(\alpha_i)$. Due to the low scattering by the materials used throughout this investigation, the beam fully illuminated the sample, and thus no correction was required.

4.4 Determination of the Structure of the unit cell

Once the set of experimental intensity data I(h,k,l) has been obtained, the approach to structural analysis demands careful consideration. Two broad approaches are used in crystallography:

1. When one possesses a complete dataset $I_{dat}(h,k,l)$ for many diffraction peaks, then a model-independent approach, such as a Patterson analysis, or the direct methods formalism, can be adopted [21]. The over-determination implicit in the data can be used to infer statistically the

phase of the amplitude of each diffraction peak using statistical approaches.

2. For cases where the number of peak intensities is insufficient for a model-independent structural analysis, then additional user-supplied information or constraints must be introduced. These approaches are generally referred to as direct space methods [22]-[24]. One of the most common approaches here is to introduce a structural model involving a relatively small number of fitted parameters. This structural model is used to calculate directly the structure factor $F_{calc}(h,k,l)$ and its related intensity $I_{calc}(h,k,l) = |F_{calc}(h,k,l)|^2$.

4.4.1 Direct methods & Patterson analysis

As mentioned above, one possible method of determining the structure within the unit cell is by performing a Patterson analysis. The Patterson function is a function which can be computed without the knowledge of the phases of the structure factors and can give details of the structure of the unit cell [21].

$$P(x,y,z) = \frac{1}{V}\sum_{h,k,l} |F_{hkl}|^2 cos\{2\pi(hx + ky + lz)\}$$

...Equation 4.6

After placing all the scattered intensities into the function, a contour map can be drawn to represent the real-space unit cell. A positive peak in the contour map

means that there are two (or more) atoms within the unit cell separated by a vector equal to the one created from the peak to the origin of the contour map.

Direct methods are another early way in which the structures of simple unit cells were calculated. Harker and Kasper in 1948 showed that inequality relationships existed between the structure factors, and that such relationships were capable of giving phase information.

One drawback of the traditional methods of structural analysis is that one needs a large number of measured peak intensities to obtain an accurate result. However, this problem does not affect the second approach (direct-space methods) of determining the structure of the unit cell because a model is used to calculate a full set of intensities which can be compared to the partial set of experimental values.

4.4.2 Direct Space approach

The direct-space methods approach contains a trial postulation of the unit cell and the structure factor calculated from this trial unit cell. The trial solution can be postulated by the known molecular connectivity of the material. Once a trial solution has been made, global optimization techniques such as least square fitting, Monte Carlo or genetic algorithms are used to locate the global minimum corresponding to the best structure solution. This structure factor can then be compared with experimental data. Different trial solutions are tried until the calculated structure factors compare well with experimental data.

Direct-space methods for determining the structure of materials has been mainly applied to unit cells with low molecular numbers, due to making the structure determination more complex in terms of degrees of freedom ie. the number of structural parameters varied to generate new trial solutions. The unit cell that we have calculated for F8 is large, and contains many atoms (~1000 atoms), so there are many possible trial solutions, which makes using this method unviable.

4.4.3 Molecular dynamics

Due to the problems explained above, another procedure was needed in order to determine the structure. Molecular dynamics simulations calculate the positions and velocities of each particle in a system at every timestep within in a calculation. The timestep between calculations must be shorter than the vibrational frequency of the atoms, and there must be enough timesteps so that the system reaches equilibrium.

Again, to compute this requires considerable computing power. To make this computing time shorter, a single chain can be first calculated, and then subsequent chains can be placed parallel to the first, and several simulations can be run from several starting positions, which can be compared.

During our studies of the structure of F8, a group from the National Sun Yat-Sen University in Taiwan published a paper which claimed to have made these calculations for PFO [14]. They also published structure factor calculations for their

energy-minimised structure, together with experimental data, and claimed reasonably good agreement between them. After correspondence they kindly sent us their x, y, z positions of the atoms within the unit cell for their model.

4.4.4 The structure factor calculation

As described in chapter 2 the unit cell structure factor can be calculated using the equation:

$$F(Q) = \sum_{r_j} F_j^{molecule}(Q) e^{iQ.r_j}$$

...Equation 4.7

where r_j is the position of the jth molecule within the unit cell. Here, $F_j^{molecule}$ is replaced by the atomic scattering factor f_j and F(Q) is summed over all atoms in the unit cell. A program was written to perform this summation.

Before writing a program for this purpose, it was important to ensure that the supplied unit cell data was accurate. To do this it was advantageous to obtain a visual image of the unit cell. The file supplied by S Chen et al only contained x, y, z coordinates which needed to be converted into a format that VMD, the program used to view the structure, could read. The obvious choice for this is the Protein Data Bank (PDB) format. Below is an example of a .pdb file

ATOM	1	C	C	A	0	4.050	3.410	32.530	1.00	0.00
ATOM	2	C	C	A	0	4.700	4.280	31.630	1.00	0.00

The first column is the particle type. The second column is the serial number, ie each atom is labelled with a number. The third column is its chemical symbol, The fourth, fifth and sixth column are its residue number, chain orientation and residue sequence number respectively. The next 3 columns contain the atom's x, y, z coordinates within the atom ensemble in units of angstroms. The final two columns are the occupancy factor and temperature factor. Since the purpose of converting to the .pdb format is to view the unit cell, only the x, y, z values are important, and so standard values for all other variables have been used.

The unit cell structure put forward by S Chen et al contained 8 chains, each one containing 4 monomer repeat units. In total, the model contained 928 carbon atoms. In turn each of these chains were individually viewed in VMD. This structure can be seen in figure 4.13.

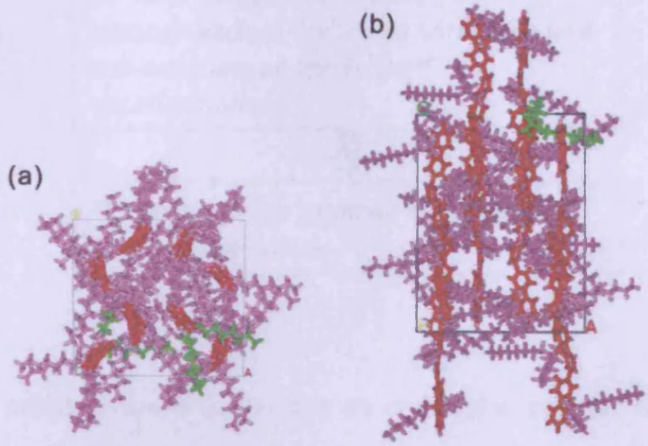

Figure 4.13. The unit cell supplied by S Chen taken from [14]. a) viewed along unit cell direction **c** and b) viewed along unit cell direction **a**.

Once the supplied unit cell atom positions had been checked, a Fortran90 program was written to calculate the structure factors, using this .pdb file as an input file. The structure of the program is outlined here.

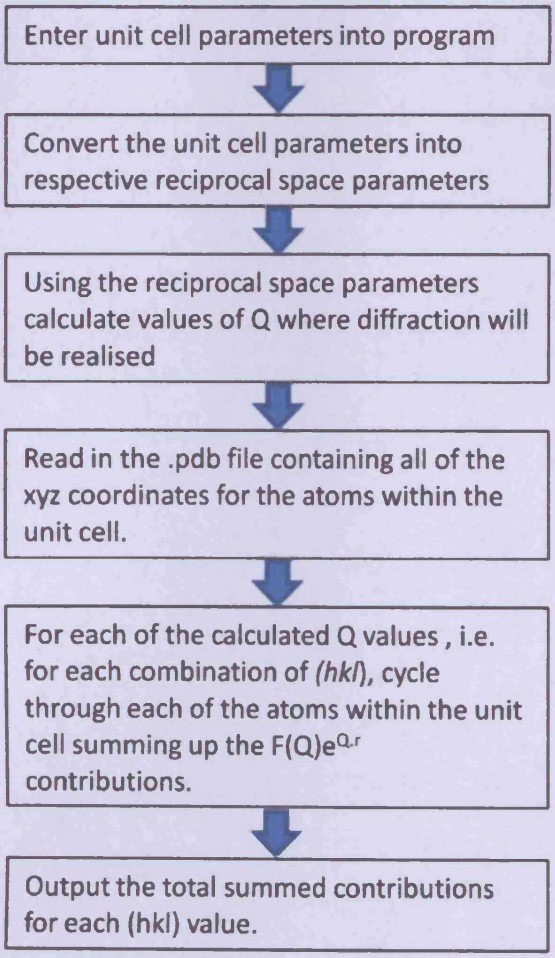

The program outlined above was tested by creating a .pdb file that contained the positions of the potassium and chlorine atoms within a KCl crystal. KCl was chosen for this test case as the solution for the crystalline structure is well known.

4.4.5 Results obtained from the structure factor calculations

The calculations carried out by S Chen et al were on samples which had been cast from a high concentration onto a glass substrate. The high concentration produced films which had an absence of preferred orientation, and produced "powder" diffraction patterns. This meant that when comparing our samples with theirs, it was necessary to multiply any peak they detected by the magnitude of its corresponding scattering vector squared. Below is a table that details the intensities observed and calculated by S Chen and myself. S Chen's intensities listed in table 4.1 were taken from the 2004 Macromolecules paper, reference [14], and have been normalised to the 002 peak, as have our calculated peaks. Our observed intensities cannot be normalised to the 002 peak due to our not being able to detect all of the intensity from the (0,0,*l*) peaks, and have therefore been normalised such that the intensity of the (101) peak equates to the (101) observed by S Chen et al.

(hkl) index	S Chen observed peaks	S Chen calculated peaks	Our observed peaks	Our calculated peaks
101	6.0	12.6	6.0	0.7
102	7.8	10.4	1.6	5.5
103	45.9	74.0	9.6	0.4
303	49.4	49.4	6.2	0.3
401	50.4	50.4	18.3	3.9
002	100	100	N/A	100
205	52.1	67.0	13.0	4.9
502	93.3	50.8	N/A	4.6
305	98.4	62.6	N/A	2.7
301	N/A	N/A	3.6	6.2
201	N/A	N/A	0.6	28.7
202	N/A	N/A	0	3.3
203	N/A	N/A	1.5	90.6
204	N/A	N/A	3.0	3.0
302	N/A	N/A	3.1	6.3
304	N/A	N/A	10.2	2.0

Table 4.1. Observed and calculated intensities for our data along with S. Chen's data.

In the column containing S Chen's intensities, N/A denotes peaks which are not present on graphs presented in the paper. For our peaks, N/A denotes peaks that are so close together that it was not possible to record reliable intensities.

To calculate their structure factors, S Chen et al used a package called Cerius2 (version 4.6, Accelrys). This package positions the polymer chains within an exaggerated unit cell size and runs the molecular dynamics, forbidding the chains to come together. After the system has reached an equilibrium (i.e. the system sits in a local potential energy minima) the chains are brought closer together and the computing is repeated until the chains are close enough together for the restriction to be taken away, and the unit cell is achieved. However, as is seen in table 4.1, the structure factors that have been calculated from the supplied unit cell do not match the ones calculated from the MD package.

4.5 Summary and Conclusions of the Diffraction investigation

A process for determining the experimental structure factors for a thin polymer film, using grazing incidence x-ray diffraction, has been described for the first time. F8 was selected as an archetypal conjugated polymer for the study due to the common use of it and its derivatives in devices. Determining the structure of conjugated polymers is particularly challenging due to their large unit cells, low symmetry and the relatively low number of measureable peaks, and at present no detailed structural determinations exists for any of these polymers, either in the bulk or thin

films. The use of an area detector greatly speeds up experimental measurement, and the practical aspects of this are also discussed. The films are polycrystalline in the plane of the surface whereas the $\mathbf{c}^*$ axis is normal to the interface, with well-defined peaks in this direction, consistent with layering of the structure normal to the surface. The correction factors for this kind of ordering are discussed. Peaks with $h=k=0$ and those with $l=0$ must be omitted from the dataset because of the difficulty of accounting for the effects of the polycrystalline ordering, and for refraction.

A limited set of structure factors was produced for F8. These were then compared with a paper by Chen et al that appeared concurrently with our work, which claimed to present a full structural determination of F8, which was produced using samples of a very thick film of rough morphology, prepared by sequential drop-casting. Their published x-ray diffraction intensities differed significantly from our dataset, though the unit cell parameters were consistent with our area detector images. They performed molecular modelling to predict the structure of the F8 unit cell, and claimed that the intensities calculated from this structure gave reasonably good agreement with their observed x-ray diffraction intensities. Our calculations using their structural model give intensities which are inconsistent with both the Chen x-ray data and with the intensities they claim to obtain from their structural model. As the sample preparation for the α phase samples we prepared are consistent with the sample preparation outlined by Chen it is believed that any possible mixed phases that maybe present in the samples would be present in both our samples as well as

the samples prepared by Chen. Subsequent discussions with Prof G Ungar, University of Sheffield, whose group has performed extensive unpublished fibre diffraction studies of F8, confirmed that the structure postulated by Chen is questionable. They concluded independently that the Chen paper was unreliable and that great care must be taken with structural studies of F8 to obtain samples which are not contaminated with small amounts of other phases. Despite their extensive analysis, the Sheffield group has failed to solve the structure of F8 and their work remains unpublished. Moreover, further discussions with another group headed by Prof. Jenny Nelson, of Imperial College London, established that they had used a chemical modelling package to minimise the energy of F8 and had found that their results disagreed with Chen et al.

This leaves an unsatisfactory situation in which the only published paper presenting a detailed structural model of a conjugated polymer film is shown to be unreliable. Our work points the way towards a detailed structural study of such materials using a combined approach of x-ray diffraction analysis with a parameterised model involving energy-minimised structures from molecular dynamics, but we have make little progress in this direction. The central role of conjugated polymers in molecular electronics technologies should provide sufficient motivation for this kind of study to be undertaken in future.

The lack of publications for structure determination of conjugated polymers supports this conclusion. At present only one publication has claimed to have achieved this, and this chapter has raised doubts about their claim.

4.6 AFM roughness calculations

As mentioned earlier in the chapter, an important property contributing to the conduction of PFO within a device is the roughness of the free surface. Organic thin film transistors are extremely sensitive to small changes in morphology as well as the structure of the polymer film. The rms roughness of the free interface of another conjugated polymer P3HT has been found to vary between 2-20Å after annealing.

Work has been carried out on another conjugated polymer, pentacene, which showed that the roughness of the gate electrode in a field effect transistor affected the performance of the transistor. In this chapter we report measurements taken of the free surface roughness of F8 to ascertain whether the roughness of the F8 changes during the crystallisation phase transition.

Figure 4.14 shows AFM images of several PFO samples annealed at different temperatures that have been flattened after capture by applying a 3rd order polynomial. All the samples were prepared simultaneously from the same solution and were annealed sequentially.

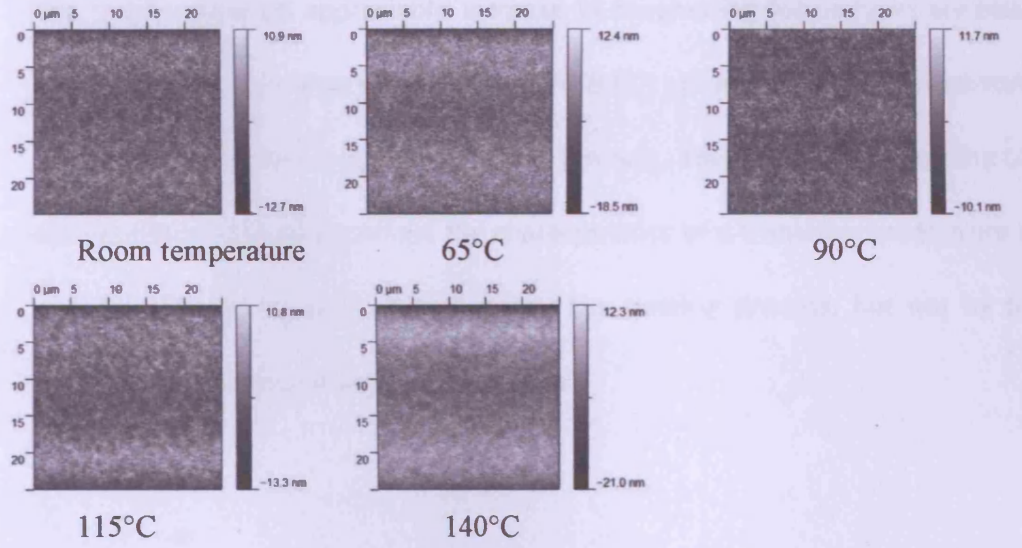

Figure 4.14. AFM images for each annealing temperature

After flattening, an rms roughness value is taken from each 25x25µm image. Each image is split up into 3x3 smaller images and another rms roughness is taken of each smaller image. An error is calculated from these values for each temperature. The graph of figure 4.15 illustrates how the roughness changes as the PFO undergoes a phase change.

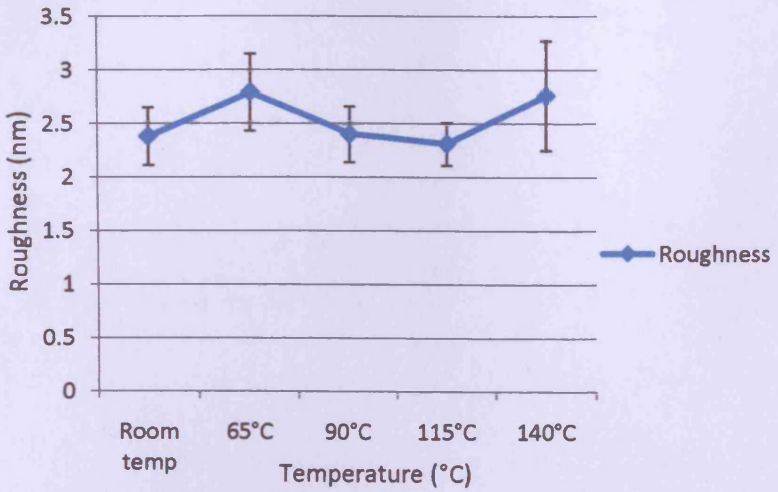

Figure 4.15. A graph of roughness vs temperature illustrating no appreciable increase in roughness as the sample undergoes a phase transition.

The results show no appreciable increase in roughening for samples annealed above the glass transition temperature (~70-80°C) nor at the anneal temperature of 140°C at which the crystalline phase is formed. This suggests that during the aforementioned heating process the characteristics of a transistor made from F8 may be affected by other factors during the heating process, but not by the roughness of the top surface of the F8 film.

4.6 References

[1] K. M. Coakley, M. D. McGehee, Chem. Mater., 2004, 16, 4533.

[2] M. O'Neill, S. M. Kelly, Adv. Mater., 2003, 15, 1135.

[3] C. Weder, C. Sarwa, C. Bastiaansen, P. Smith, Adv. Mater, 1997, 9, 1035.

[4] A. Montall, C. Bastiaansen, P. Smith, C. Weder, Nature, 1998, 392, 261.

[5] C. Weder, C. Sarwa, A. Montall, C. Bastiaansen, P. Smith, Science, 1998, 279, 835.

[6] H. Sirringhaus, R. J. Wilson, R. H. Friend et al, APL, 2000, 77, 406.

[7] G. Lieser, M. Oda, T. Miteva et al, Macromolecules, 2000, 33, 4490.

[8] M. Grell, W. Knoll, D. Lupo, A. Meisel et al, Adv. Mater, 1999, 11, 671.

[9] S. Dröge, M. S. Al Khalifah, M. O'Neill et al, J. Phys. Chem. B, 2009, 113, 49.

[10] A. E. A. Contoret, S. R. Farrar et al, Adv. Mater, 2000, 12, 971.

[11] M. P. Alfred, P. Vlachos, A. E. A. Contoret et al, J. Mater. Chem, 2005, 15, 3208.

[12] C. Liu, H. Tang, A. J. Bard, J. Phys. Chem., 1996, 100, 3587.

[13] M. Grell, D. D. C. Bradley, G. Ungar, Macromolecules, 1999, 32, 5810.

[14] S. H. Chen, H. L. Chou, A. C. Su, Macromolecules, 2004, 37, 6838.

[15] S. H. Chen, A. C. Su, C. H. Su, Macromolecules, 2005, 38, 379.

[16] M. Knaapila, R. Stepanyan, B. P. Lyons, Macromolecules, 2005, 38, 2744.

[17] S. H. Chen, A. C. Su, S. A. Chen, Macromolecules, 2006, 39, 9143.

[18] M. Grell, D. D. C. Bradley, M. Inbasekaran et al, Adv. Mater., 1997, 9, 798.

[19] G. Klärner*, M. H. Davey, W. D. Chen et al, Adv. Mater., 1998, 10, 993.

[20] A. Babel, S. A. Jenekhe, Macromolecules, 2003, 36, 7759.

[21] M. M. Woolfson, Rep. Prog. Phys., 1971, 34, 369.

[22] R. Cerny, Chem. Met. Alloys, 2008, 1, 120.

[23] K. D. M. Harris, M. Tremyane, P. Lightfoot, P. G. Bruce, J. Am. Chem. Soc., 1994, 116, 3543.

[24] Y. G. Andreev, P. Lightfoot, P. G. Bruce, J. Appl. Crystallogr., 1997, 30, 294.

Chapter 5 – Investigation into the structure of thin film PQT-12

5.1 Introduction

Organic thin-film transistors have attracted a great deal of interest in recent years as they have developed from research curiosities to emerging technology. This is mainly due to them being a low cost alternative to silicon transistors, being made from solution-based deposition techniques. It is believed that molecular ordering in these devices is essential to achieving high carrier electron mobility because the transport mechanisms rely on the intermolecular electronic coupling [1]. Apart from high structural ordering, the chosen materials must have sufficient stability to permit fabrication before a capping layer is applied.

Chapter 5 – Investigation into the structure of thin film PQT-12

Polythiophenes, in particular head-to-tail P3HT, have been shown to be an important class of solution-processable polymers for OFETs [2-5]. When processed and maintained in an inert atmosphere these have been shown to have a high mobility [2-5]. However, when processed in air this mobility is considerably lower [6-7]. B Ong et al have shown that another polythiophene, PQT-12, also has high mobility and is also stable in air [6-7]. PQT differs from P3HT in having unsubstituted thienylene moieties along the polymer backbone which increase torsional deviations, which in turn reduces the π-conjugation, which has been shown to reduce stability in air [7]. However, having the constraint of fabricating the devices under vacuum decreases the economic advantage OFETs have over their amorphous silicon counterparts.

Though work has been carried out on the electrical properties of PQT [8-12], little has been done to investigate the microstructure of PQT-12 film. Hairy rod polymers, a class of which PQT is a member, generally lead to a packing scheme dependent on the molecular structure of the backbone and the side chains [1]. These hairy rod polymers generally adopt lamellar structures, with the adjacent backbones perpendicular to the lamellar stacking direction having overlapping π-orbitals. This structure leads to anisotropic electrical transport, where the electrons can either flow along the backbone or through the π-stack. Therefore it is advantageous to have the polymers arranged so that the desired electron transport direction in a device corresponds to one of these two directions.

The aims for this chapter were to ascertain:

i) The structure of as-spun PQT-12;

ii) The structure of PQT-12 upon annealing;

iii) The effect of modifying the substrate onto which the PQT-12 is deposited, in particular using OTS-functionalised SiO_2 as the substrate; and

iv) The effect of the molecular weight of the PQT-12 on the structure of the film in both as-spun and annealed samples.

During the experiment a number of other effects were observed that, to our knowledge, have not previously been observed during GIXRD experiments. These will also be discussed in this chapter.

5.2 Sample preparation and experimental procedure

The PQT-12 used in this investigation was supplied by Prof. M. Turner of Manchester University. Samples of two molecular weights were used, one of 5000amu and one of ~16000amu, both dissolved in Chloroform at a concentration of 10mg/ml. Samples were spin-coated from their respective solution onto a Si(100) substrate having a 300nm oxide layer at 4000rpm for 180s. The oxidised silicon substrate was cleaned prior to spin-coating using acetone followed by Isopropyl alcohol to remove any impurities on the surface, followed by drying under flowing nitrogen gas. No heat treatment of the samples was performed prior to the samples being placed on Beamline BM 28 at the ESRF. Experiments to determine the structure of the unit cell were all carried out at room temperature. Experiments were also performed to investigate the effect of

heating on the self assembled structure that was created during the sample preparation process. These temperature studies were carried out on samples of both previously stated molecular weights. The samples were cycled once in-situ through the heat cycle of room temperature - 60°C - 80°C - 130°C, then cooled to a temperature of 40°C at a rate of 1°C/min. At each temperature the samples were maintained at temperature while area detector images were taken until no further change was observed, before heating/cooling to the next temperature.

5.3 The structure of as-spun PQT-12

5.3.1 Unit cell parameter out of plane and one of the unit cell parameters in plane

The unit cell parameters for the 5000amu PQT-12 were calculated from the area detector image shown in figure 5.1.

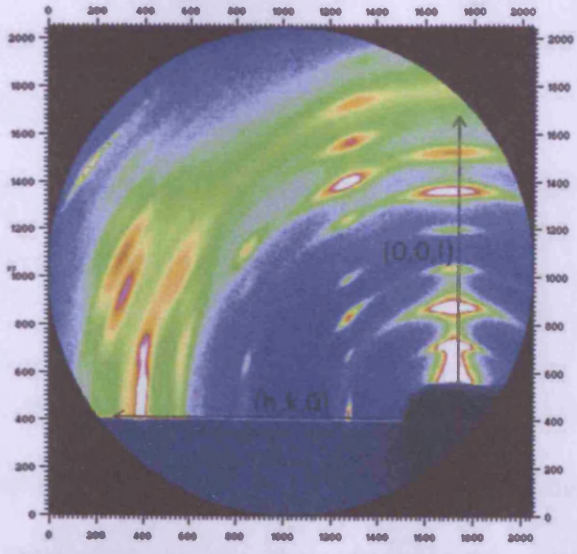

Figure 5.1 Area detector image showing the as spun self assembled diffraction pattern, the two arrows defining the out-of-plane and in-plane directions.

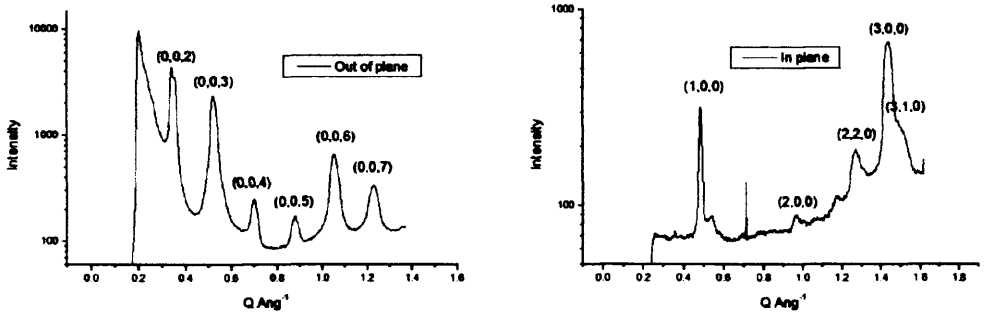

Figure 5.2 Corresponding sections from figure 5.1 taken along (0,0,l) (Out of plane) and (h,k,0) (In plane). The main peaks have been labelled resulting in a calculated unit cell of a=13.10Å, b=16.42Å, c=35.60Å.

From the experimental image shown in figure 5.1 several deductions can be made:

1. **c*** is perpendicular to the surface.
2. There is a clear in-plane periodicity in one dimension, arbitrarily chosen to be the [1,0,0] direction.
3. Peaks for the second in-plane (0,*k*,0) direction are not directly observed.
4. (1,0,*l*) peaks have the same spacing as (0,0,*l*) peaks but have an offset which suggests an angle between **c*** and **a***. This offset is negative for peaks where $l \leq 4$ but positive for peaks where $l \geq 5$.
5. The peaks are asymmetric, i.e. thin radially and broad tangentially, which suggests a polycrystalline structure.

From the definition of the reciprocal lattice (where $\mathbf{c}^* = (2\pi/V)\mathbf{a} \times \mathbf{b}$) **c*** must be perpendicular to a and **b**. Using this equation and deduction 1 above, it is inferred that **a** and **b** run parallel to the surface. Regular spacings seen in the section along (0,0,*l*) relate to a unit cell parameter, **c**, of 35.6 ± 0.7 Angstroms.

As seen in the area detector image shown in figure 5.1, there is also a dominant spacing in the in-plane direction. The (0,0,*l*) and (1,0,*l*) peaks are observed in addition to the peak at (2,0,*l*) and a major peak is detected at (3,0,*l*) with $l \approx 0$. This spacing results in an in-plane unit cell length of 13.10 ± 0.12 Angstroms.

As stated in deduction 3, (0,*k*,0) peaks are not directly observed. However, in-plane peaks are observed at Q=1.262 ± 0.002Å^{-1} and Q=1.510 ± 0.002Å^{-1}, which were attributed to (*h*,*k*,0) orientations.

5.3.2 Possible model for determining the third unit cell parameter

The above analysis identifies clearly the magnitude of the **a** and **c** unit cell vectors. However, we cannot unambiguously identify the **b** unit cell vector. Here, we consider the possible indexing of the two in-plane peaks at Q=1.262Å^{-1} and Q=1.510Å^{-1}. We tentatively attribute these to be the (2,2,*l*) and (3,1,*l*) peaks respectively.

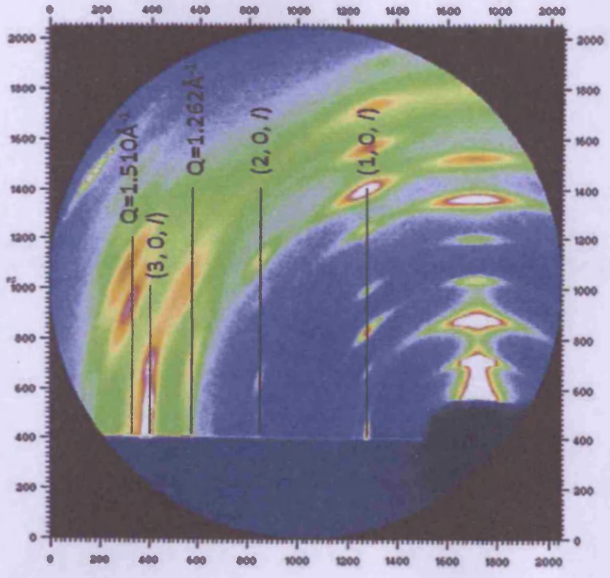

Figure 5.3 The partial in-plane indexing of PQT-12 with Q values for the uncertain peaks.

The spacing between the (2,0,*l*) peaks and the peaks at Q=1.262Å^{-1} is greater than the spacing between the (3,0,*l*) peaks and the peaks at Q=1.510Å^{-1}, and hence the former peak is likely to have a higher *k* index than the latter. Other possible (*h, k, l*) indices are unlikely, in that they would involve unrealistic values for **b**. From the values of the two unit cell parameters, already determined from the area detector image, the final parameter, b, has been calculated to be 16.4 ± 0.6Å with an angle between $\mathbf{a}^*$ and $\mathbf{b}^*$, γ, to be 86.6 ± 2.3° using:

$$Q^2 = h^2a^{*2} + k^2b^{*2} + 2hka^*b^*cos\gamma^*$$

..Equation 5.1

Which leads to a unit cell with overall dimensions shown in figure 5.4.

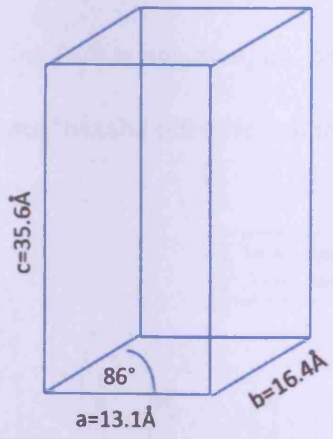

Figure 5.4. The unit dimensions when the inplane peaks at $Q_{//}$=1.262Å and $Q_{//}$=1.510Å are attributed to the (2,2,*l*) and (3,1,*l*) peaks

5.3.3 Offset of peaks along (1, 0, *l*)

The most puzzling aspect of this diffraction pattern is the apparent offset in the *l* values of the (1, 0, *l*) peaks relative to the (0, 0, *l*) peaks. The spacing between the (1, 0, *l*) peaks is the same as that between the (0, 0, *l*) peaks. However, there is an offset between the *l* values at the diffraction peaks, and this offset is of opposite sign for $l \leq 4$, where it is negative, i.e. observed at a lower Q value, and for $l \geq 5$ where the offset is positive. Furthermore, one would expect that (*h, k, l*) peaks and (*-h, -k, l*) peaks would both be observed since there is no preferred in-plane alignment. For instance, one would expect that if a peak is observed at, for example (1, 0, 3), then a corresponding peak should be observed at (-1, 0, 3). However this is not observed. Figure 5.5 displays sections along (1, 0, *l*) and (0, 0, *l*) to illustrate the offset between the peaks of the sections. The figure also illustrates that the offset for $l \leq 4$ is negative, i.e. observed at a lower Q value, and positive for peaks where $l \geq 5$ and that the offset for all the peaks is equal.

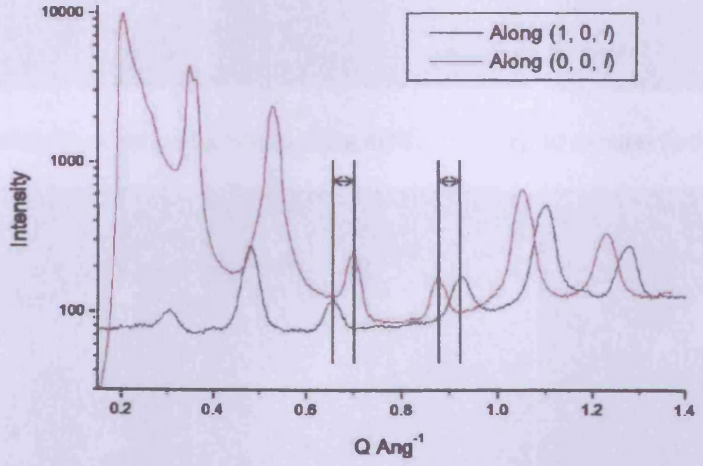

Figure 5.5 Sections along (1, 0, l) and (0, 0, l) showing an offset between peaks

We have discussed this diffraction pattern with Professor Kenneth Harris and his group in the School of Chemistry at Cardiff. They have extensive, broad experience of indexing peaks to determine unit cell parameters. They could not explain the diffraction pattern further, and we conclude that this is likely to represent a mixed phase. The behaviour of the (1, 0, *l*) together with the puzzling offset of peaks relative to the (0, 0, *l*) peaks is not understood.

5.4 The structure of PQT-12 after annealing

While heating the 5000amu sample of the previous section, the crystalline peaks disappeared as the temperature was increased.

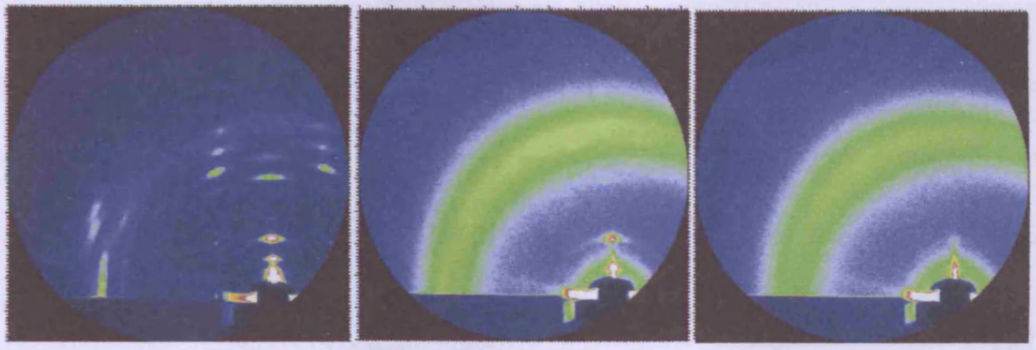

a) Room Temperature/ As spun b) 10 minutes at 60°C c) 10 minutes further annealing a 80°C

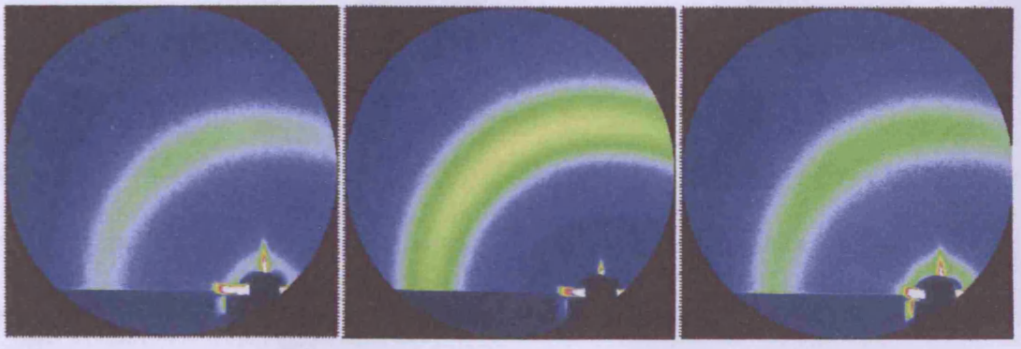

d) 10 minutes at 100°C e) 10 minutes at 130°C f) Room temperature after cooling

Figure 5.6 Area detector images taken at various temperatures during a heating cycle.

As the PQT-12 is heated from room temperature to 60°C the crystalline structure is quickly lost. After 10mins at 60°C only the strong (003) can be still be seen. Also when heating to 60°C a broad amorphous peak rapidly develops at Q=0.267Å^{-1}. Another broad peak further out is also seen, which is due to the 300nm thick amorphous SiO_2 layer on the Si(100) substrate. Intensities at various positions across this peak have been taken at various incident angles around the critical angle of the PQT-12 to determine whether a weaker PQT-12 peak is being dominated by the SiO_2 scattering. All intensity profiles taken suggest that there is no PQT-12 peak there. When the temperature is increased to 80°C the (003) peak disappears and all remnants of the original as-spun crystalline structure has been lost during the melting process. This amorphous structure remains as the temperature is increased to 130°C. Above 130°C all structure is lost. The temperature was then dropped from 130°C to 40°C at 1°C/min. The heater was then switched off and the sample was left for 20mins to allow the sample to stabilise at room temperature. Images taken of the sample after cooling showed that the amorphous ring at Q=0.267 ± 0.002 Å^{-1} had returned, but showed no crystalline structure. At various temperatures between 60°C and 130°C the sample was cooled to RT at the same rate as described before, and the same amorphous ring was seen. Due to no scattering being seen above 130°C, no measurements were taken above this temperature.

These low molecular weight samples of PQT-12 were not exposed to any heat treatment during preparation of the samples. The diffraction pattern observed in figure 5.5(a) is due to the crystalline structure created during the spin coating of the film. Since this structure disappears on minimal heating, it suggests that this is a metastable phase

which self-assembles during spin-coating. The structure cannot be solved, and may well represent a mixed phase. The structure does not return when the sample is cooled quickly or cooled slowly from 130°C to 40°C through the film's glass transition temperature. This effect will be discussed later in the chapter in the context of grazing incidence diffraction studies of PQT-12 nanowires.

An investigation of the effect of temperature on the samples of higher molecular weight can be found later in the chapter.

5.5 The effect of OTS-modification of the SiO_2 substrate on the PQT-12 film

One of the great advantages of the use of polymers in field effect transistors (FET's) is that they can be fabricated easily and cheaply on various substrates[13]. Applying a surface treatment to the gate insulator is a possible approach to improve the performance of such devices in order to improve the molecular alignment in the channel adjacent to the polymer/gate insulator interface[14]. Applying a self-assembled monolayer of octadecyltrichlorosilane (OTS) to the gate insulator has been shown to improve the performance of an OFET[14]-[16]. Whereas silicon oxide is hydrophilic, OTS comprises a hydrophobic alkyl chain with a polar $SiCl_3$ headgroup which attaches the chain to the silicon oxide surface. Here, we investigate the effect of an OTS interlayer on the ordering in the PQT-12 film.

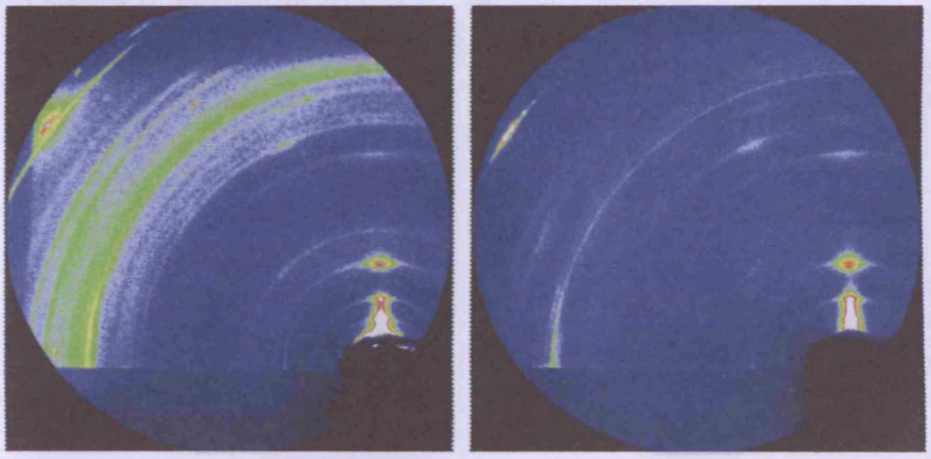

Figure 5.7 Area detector images of the PQT film which has been spin-coated onto OTS treated SiO_2 and native SiO_2 respectively for an incident angle of lower than the critical angle. The OTS treated sample shows a higher degree of polycrystallinity at its surface.

Figure 5.7 shows area detector images of OTS treated and untreated SiO_2 samples with a thin PQT-12 layer on top. The major difference seen from these is that the treated sample would appear to have a higher degree of polycrystallinity, as is inferred from the ring-like diffraction pattern.

As the incident angle is increased, and the X-rays start to probe deeper into the bulk the diffraction pattern from the OTS treated SiO_2 sample shows a more crystalline orientation, becoming similar to the diffraction pattern from the film on the native SiO_2 substrate.

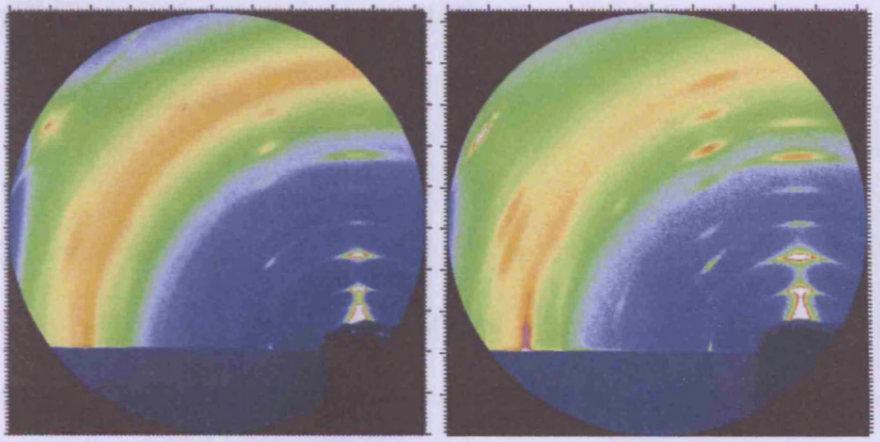

Figure 5.8 Area detector images detecting the bulk scattering of the PQT film which has been spin-coated onto OTS treated SiO_2 and native SiO_2 respectively, showing a more similar type of structure.

The strong broad ring seen further out is due to the SiO_2. Sections taken out of plane with the OTS still show polycrystalline rings.

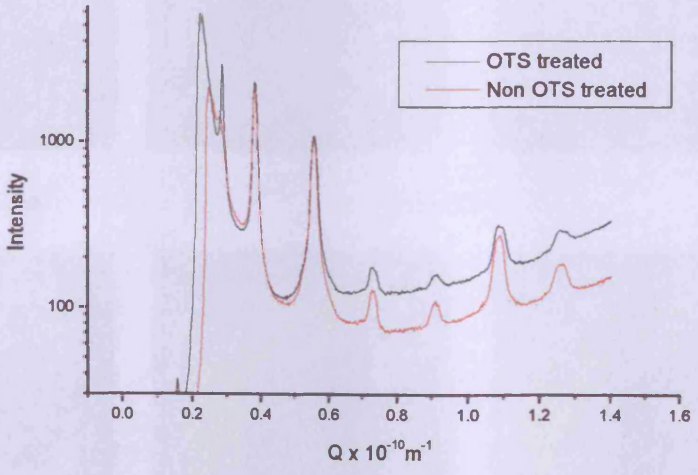

Figure 5.9 Out of plane 'bulk' sections for the PQT film deposited onto the two types of substrate illustrating a strong polycrystalline peak at $Q=0.240Å^{-1}$.

The sharp increase at $Q \approx 0.2\text{Å}^{-1}$ in the profile of figure 5.8 is due to the transition from an area shielded by the beamstop.

During the experiment, the depth-variation of the molecular ordering was probed by varying the incident angle of the x-ray beam. Figures 5.7 and 5.8 illustrate the diffraction pattern for the surface and bulk respectively, and differences are seen between the structures at the two depths. Figure 5.10 shows the diffraction patterns realised from a full range of incident angles in an attempt to analyse the way in which the structure develops as the x-rays probe deeper into the deposited film.

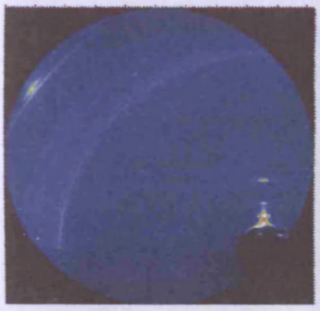

θ_i=0.100

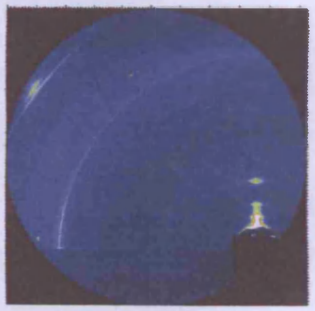

θ_i=0.125

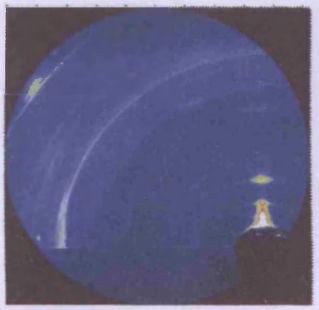

θ_i=0.150

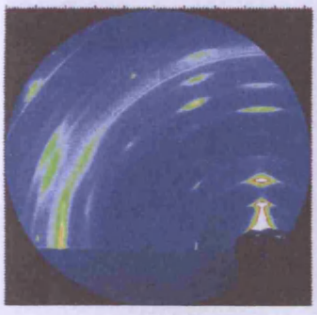

θ_i=0.175

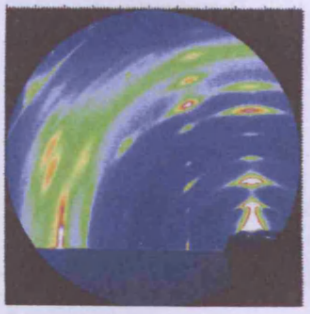

θ_i=0.200

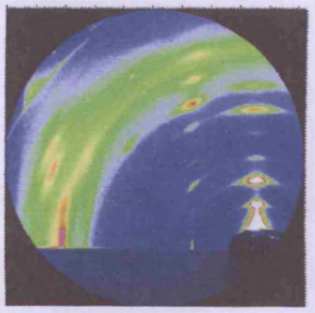

θ_i=0.225

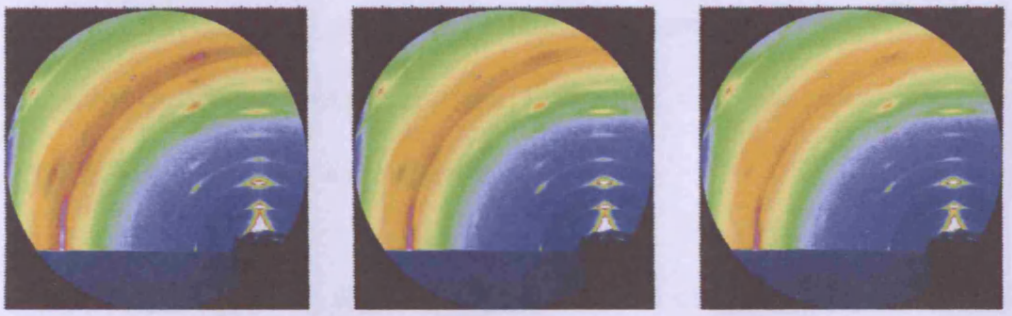

θ_i=0.250 θ_i=0.275 θ_i=0.300

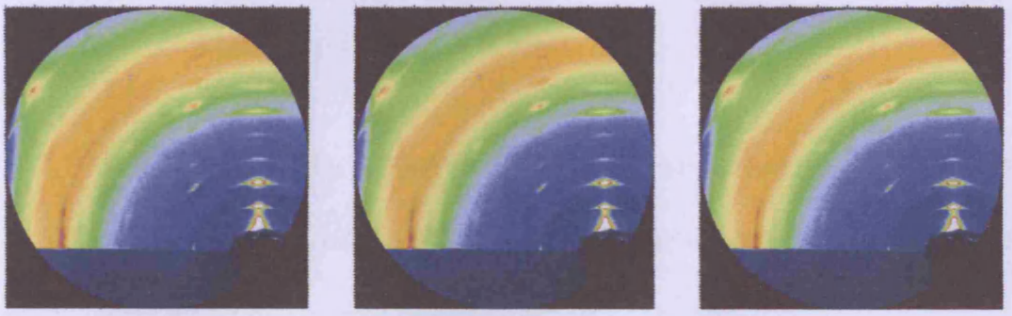

θ_i=0.325 θ_i=0.350 θ_i=0.375

Figure 5.10 Diffraction images for PQT-12/OTS/SiO_2 for varying incident angle which shows the incident angle dependency of the diffraction pattern.

These images show crystalline peaks developing as the incident angle is increased, and the signature SiO_2 amorphous scattering appears when the incident angle is raised above the critical angle of the SiO_2 (around 0.25°) and the x-rays penetrate into the substrate.

The x-rays at incident angles below the critical angle only penetrate into a fraction of the film, and therefore the scattering is only due to the structure at this small fraction of the film. It can be seen from the diffraction pattern at this incident angle that the structure is polycrystalline. Also at incident angles above the critical angle of the film the structure appears more crystalline, and the top fraction of the film, that previously contributed to all the diffraction pattern, now only contributes to a small fraction of the

scattering observed in the diffraction pattern. To determine whether the polycrystalline structure is present in the bulk, as well as the surface, one must compare the intensities of the polycrystalline ring for the two regimes.

Regions of interest in the diffraction images are now defined around several important features of the scattering, and the intensity within these regions of interest is followed as the incident angle is increased. These are:

i) along a section of a polycrystalline ring (for the purpose of this section the 004 ring has been chosen, but the trend is the same for other polycrystalline rings);

ii) around part of a crystalline peak (the 003 peak); and

iii) around a part of the SiO_2 scattering.

Since the true values of the intensity of the regions of interest are important, the background scattering has also been calculated for each incident angle and subtracted from the intensities derived from the regions of interest defined above.

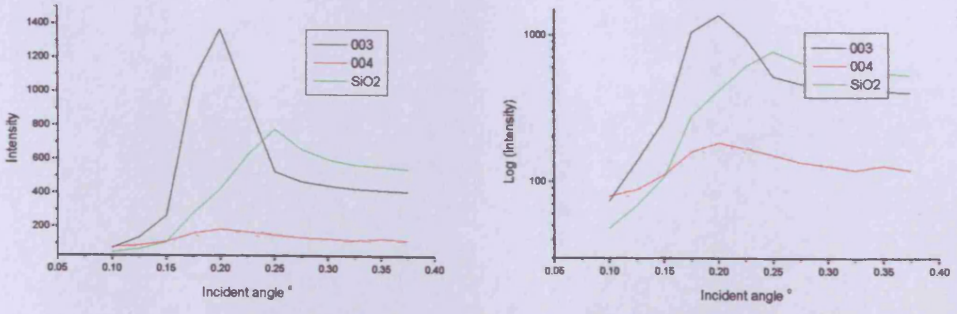

Figure 5.11 Intensity profiles for regions of interest around the 003 crystalline peak, the 004 polycrystalline ring and the SiO_2 ring. The Log of the measured intensities has been taken to better illustrate the trend in the intensities.

If the polycrystalline structure is only present at the top surface, and not present throughout the film, the intensity of the scattering should fall off to close to zero as the incident angle is increased above the critical angle. This is due to the majority of the scattering originating from the 'bulk' of the film and not limited to the top surface. As can be seen in figure 5.11 this is not the case, which suggests that there is a mixture within the film of polycrystalline and crystalline domains.

5.6 The effect of the molecular weight of PQT-12 on the film structure

All the previously presented data was taken on PQT-12 of molecular weight 5000amu, which corresponds to a molecular length of ~ 10 monomer units. Limited work was also performed on a higher molecular weight material of molecular weight ~ 16000amu, corresponding to a length of ~ 30 monomer units.

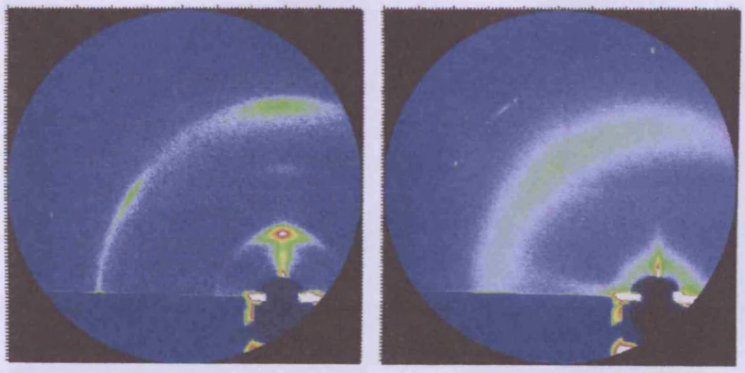

(a) Room Temperature/ As spun (b) 10 minutes at 130°C

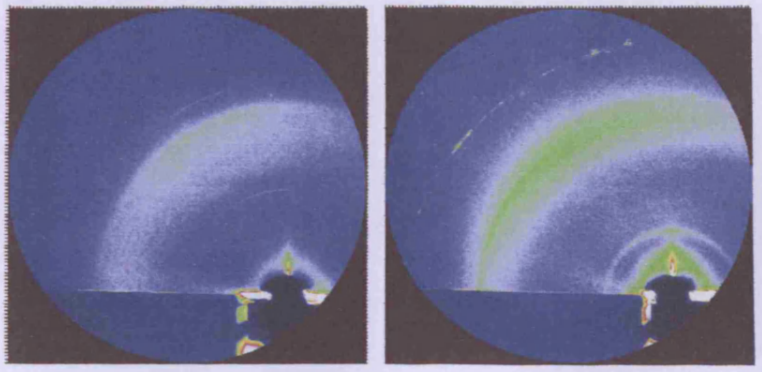

(c) 20 minutes at 130°C (d) Room temperature after cooling

Figure 5.12 Diffraction images of PQT-12 films of molecular weight ~ 16000 amu that have been taken at different times along the heating cycle (room temperature - 130°C – room temperate at a cooling rate of 1°C/min).

Figure 5.12 shows that the structure of the as spun higher Mw PQT-12 sample is very different from the corresponding lower molecular weight (Mw ~ 5000amu) sample. Many of the crystalline peaks are not observed, and only a few strong peaks remain. Also the peaks are more polycrystalline, with a smaller domain size (inferred from the broader diffraction peaks). Out of plane the peaks that are seen are at Q=0.330, 0.524, 1.067 and 1.578 ± 0.002$Å^{-1}$. The last three of these peaks can be attributed to (003) (006) and (009) peaks in the Lower Mw sample. However, the peak at Q=0.330 $Å^{-1}$ is not seen for the lower Mw sample. The in-plane scattering shows a similar trend, with a peak at Q=1.266 $Å^{-1}$, which is also seen in the lower Mw sample, attributed to the (2,2,0) peak, and a peak at Q=1.52 $Å^{-1}$ which is not observed for the lower molecular weight.

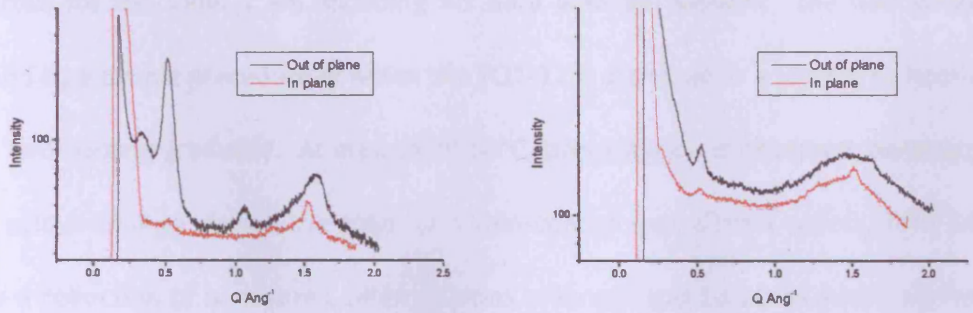

(a) As-spun (b) Heat treated sample

Figure 5.13 Sections in and out of plane for the as-spun sample and heat treated sample that have been returned to room temperature.

When heated, the structure was lost above 70°C, and the characteristic amorphous ring appeared at Q=0.267 $Å^{-1}$, along with the SiO_2 ring. At 130°C the amorphous ring was still present. However, after 20 minutes the peak was starting to disappear. The sample was held at 130°C until this peak fully disappeared. The sample was then cooled at 1°C /min to 50°C and an image was taken every 10°C. The amorphous ring reappeared almost immediately when dropping the temperature to 120°C and upon further cooling, crystalline peaks reappeared: these were more polycrystalline in nature.

5.7 The structure of PQT-12 when prepared into Nanowires

The chamber that I designed has been subsequently used by Mark Hampton, a research student investigating conjugated polymer nanowires. Following on from my work, he performed GIXRD investigations of the structure of the nanowires, and the effect of annealing. Since this data sheds light on the kind of effects I have observed and

reported for the films, I am including his data with permission. The nanowires are formed by a simple procedure in which the PQT-12 is dissolved in a solvent by heating to 70°C and cooling gradually. At around 40-50°C, precipitation is observed, accompanied by a colour change. When the solution is spin-coated onto silicon wafers, AFM images show a collection of nanowires, often microns in length and 10-20nm wide. GIXRD was performed on drop-cast samples, which gives thicker layers. Below are diffraction patterns realised from PQT-12 nanowires which have been dissolved in chlorobenzene and ortho-xylene prior to deposition.

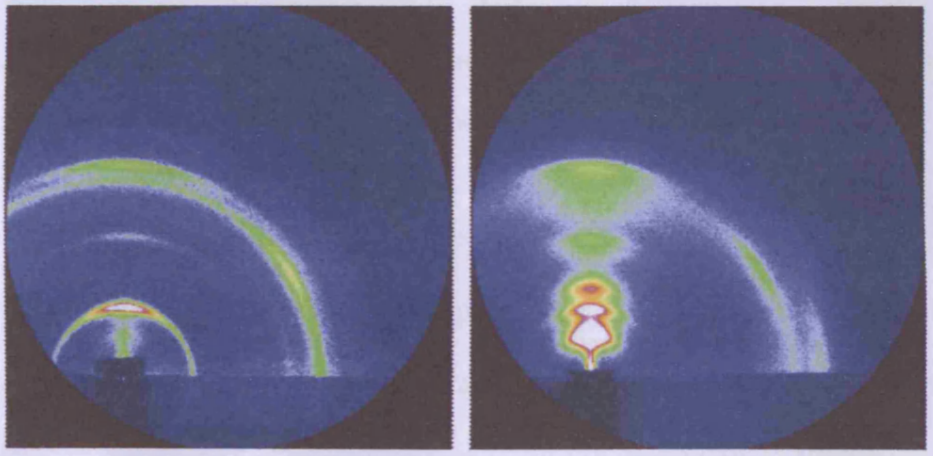

Figure 5.14, Diffraction patterns caused by PQT-12 nanowires dissolved in a) Chlorobenzene and b) Ortho-Xylene.

As seen in the two images in figure 5.13, the two different solvents used lead to very different diffraction patterns. The most intense out-of-plane peaks produced by the chlorobenzene occur at a Q value of 0.539$Å^{-1}$, and less intense peaks are realised at multiples of this at Q = 1.076 $Å^{-1}$ and 1.592 $Å^{-1}$ resulting in a d spacing along the surface normal of 11.65Å. Peaks are also seen at Q=0.323 and 1.472$Å^{-1}$. The peaks at Q =

0.539Å^{-1} and 1.472Å^{-1} are also seen in-plane along with another in plane peak at Q = 1.260Å^{-1}.

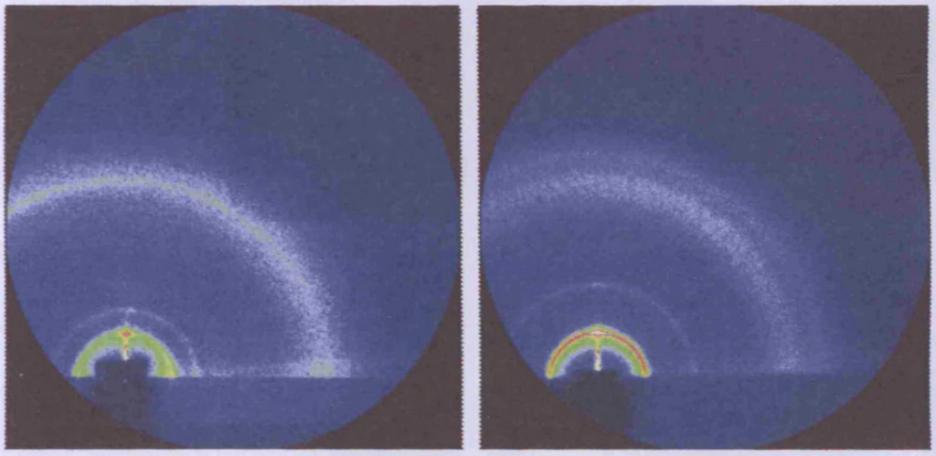

Figure 5.15, Diffraction patterns caused by PQT-12 nanowires dissolved in a) Chlorobenzene and b) Ortho-Xylene after annealing at 140°C.

The peaks seen in the diffraction pattern realised from the PQT-12 nanowires dissolved in Ortho-Xylene, occur in slightly different positions. The regular spacing seen out-of-plane in Q is slightly smaller, resulting in a d spacing of 11.80Å. The peak seen at Q=0.323Å^{-1} in the sample prepared with the chlorobenzene solvent is now seen at Q=0.342Å^{-1}, and a peak at twice this Q value is now observed. Weak peaks are seen in plane wide out at Q = 1.270, 1.515 and 1.705Å^{-1}. It should be noted that the chlorobenzene sample shows a higher degree of polycrystallinity as the (001) peak is seen in the in-plane sections. This suggests that the packing of the nanowires in the film is more restricted to an orientation along the surface normal.

The strong dependence of the nanowire structure on the solvent used strongly suggests that the solvent molecules are incorporated into the crystalline structure. Annealing of

these nanowire films at 140°C, followed by gradual cooling to room temperature, resulted in similar diffraction patterns, suggesting that the solvent molecules have been driven away, leading to the equilibrium structure in the nanowires. This suggests further that the solvent-dependent nanowire structure is metastable, incorporating solvent molecules. It is therefore possible that the crystalline structure observed for the low molecular weight film that is formed during spin-coating is in a similar metastable state (possibly incorporating solvent molecules) and that it is easily disrupted by gentle heating.

5.8 Other effects observed during the PQT-12 experiment

While undertaking this experiment we observed additional out-of-plane peaks that were absent for angles below 0.2^{0} (the critical angle for PQT-12) and above 0.25^{0} (the critical angle for $Si0_2$). These peaks did not stay at a constant scattering angle as the incident angle was varied. Below are out-of-plain sections, one at the critical angle for PQT-12, one at the critical angle for $Si0_2$ and one at an intermediate incident angle. Note that extra peaks are seen in the intermediate sections. For an incident angle that is equal to the critical angle of the SiO_2 the extra peak is still visible as a hump on the side of the major peak.

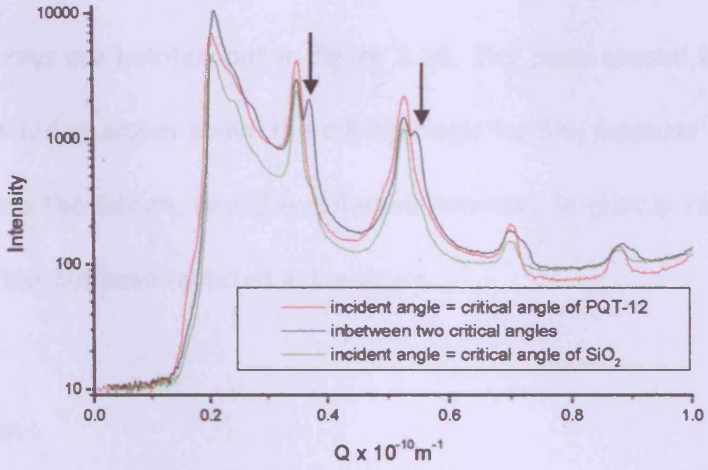

Figure 5.16 Graphs of scattering along (0,0,l) for various incident angles between the critical angles of the two materials

These peaks are believed to be due to scattering of X-rays that have been reflected from the PQT-12/SiO_2 interface and scattered while passing back through the film.

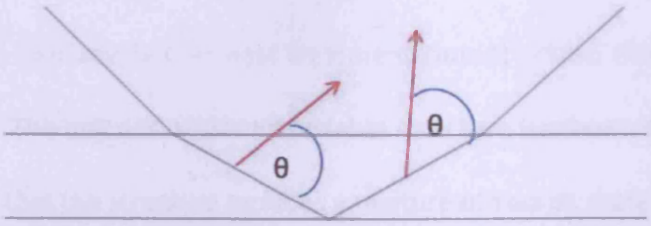

Figure 5.17 The believed path the X-rays took through the PQT film showing scattering from the incident and reflected waves.

The two red lines shown in figure 5.17 illustrate this effect. The scattering angles for the two red lines are equal. As can be seen though the angle these two red lines subtend with the surface of the sample is larger for the scattering realised from the X-rays which

have been reflected by the film/SiO_2 interface. The peaks that are believed to be due to the reflected x-rays are pointed out in figure 5.16. The peak caused by the reflected wave is not realised at angles above the critical angle for SiO_2 because the unscattered wave travels into the Silicon, and the reflected intensity is greatly reduced. To our knowledge this has not been reported in literature.

5.9 Conclusion

i) the structure of as-spun PQT-12

During this experiment the structure of PQT-12 in thin films has been investigated. PQT-12 is an important polymer, as it shows excellent electric properties, and is stable at room temperature. The structure of the unit cell in the as-spun sample has been shown to be extremely sensitive to temperature changes, which suggests that the structure is in fact metastable, and any further heat treatment cannot return the structure to the as-spun structure. The unit cell of this metastable structure has been difficult to determine as it is believed that the structure includes a mixture of two or more separate structures, which are hard to de-convolve, in order to obtain the structures of the individual orientations. Correspondence with a group led by Dr. Kenneth Harris in the Cardiff University Department, in which several polymer crystallographers work, reaffirmed this postulate. They tried and failed to deduce a structure for the as-spun PQT-12 from diffraction images we supplied them. They confirmed our suspicion that this represents a mixed phase.

ii) the structure of PQT-12 upon annealing

As mentioned above, the structure of the film is extremely sensitive to the temperature the samples have been exposed to. Once the more crystalline as-spun structure is lost the structure cannot be recaptured by simple temperature heating cycles. The structure that is realised through a heating cycle, which controllably cools the sample back through its glass transition temperature, produces a high degree of polycrystalline ordering with a larger unit cell normal to the surface.

iii) the effect of modifying the substrate onto which the PQT-12 is deposited

A large majority of the analysis of this material was conducted on samples whose substrate had been treated with OTS prior to deposition of the PQT-12. It was seen that the OTS produced a similar structure to the one seen with untreated samples, but with a higher degree of polycrystallinity. At the surface (i.e. the top 5-10nm), the PQT-12 film is entirely polycrystalline, whereas in the bulk of the film, crystalline and polycrystalline material coexist.

iv) the effect of molecular weight on the PQT-12 structure

The metastable crystalline structure described for the as-spun PQT-12 sample of molecular weight 5000amu was not seen in the PQT-12 sample of molecular weight 16000amu. Instead a regular spaced peaks are observed out of plane at the locations of

the (0,0,3), (0,0,6) and (0,0,9) peaks for the lower molecular weight samples. This spacing is consistent with a unit cell size of 12.00Å. No regular spacing is seen between peaks in the plane of the sample. Upon heating above 130°C the crystalline peaks disappeared but returned when cooled to room temperature.

5.10 References

[1] M. L. Chabinyc, M. F. Toney, R. J. Kline et al, J. AM. Chem. Soc. 2007, 129, 3226.

[2] F. Y. Yang, K. J. Chang, M. Y. Hsu et al, J. Mater. Chem. 2008, 18, 5927.

[3] L. A. Majewski, M. Grell, Synthetic Materials 2005, 151, 175.

[4] A. Zen, M. Saphiannikova, D. Neher et al, Chem. Mater. 2005, 17, 781.

[5] M. Urien, G. Wantz, E. Cloutet et al, Organic Electronics 2007, 8, 727.

[6] B. Ong, Y. Wu, P. Liu Proceedings of the IEEE, 2005, 93, 1412.

[7] B. Ong, Y. Wu, P. Liu, S. Gardner, J. AM. Chem. Soc. 2004, 126, 3378.

[8] B. S. Ong, Y. Wu, P. Liu, S. Gardner, Adv. Mater. 2005, 17, 1141.

[9] A. Salleo, T. W. Chen, A. R. Völkel et al, Physical review B, 2004, 70, 115311.

[10] Y. Wu, P. Liu, B. S. Ong et al, Applied physics letters 2005, 86, 142102.

[11] N. Zhao, G. A. Botton, S. Zhu, Macromolecules 2004, 37, 8307.

[12] T. N. Ng, J. A. Marohn, M. L. Chabinyc, J. Appl. Phys. 2006, 100, 084505.

[13] M. Maters, D. M. De Leeuw, M. J. C. M. Vissenberg et al, Opt. Mater. 1999, 189, 197.

[14] R. Hayakawa, M. Petit, T. Chikyow et al, Appl. Phys. Letters, 2008, 93, 153301.

[15] R. Hayakawa, N. Hiroshiba, T. Chikyow et al, Thin Solid Films, 2009, 518, 437.

[16] Y. Sun, X. Lu, S. Lin et al, Organics Electronics, 2010, 11, 351.

Chapter 6 – In-Situ Crystallisation of PET

6.1 Introduction

Poly(ethylene terephthalate) (PET) has been commercially used for many decades, particularly in the packaging industry, including fabrication of soft drink bottles.

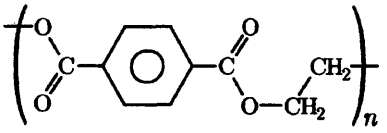

Figure 6.1 – molecular structure of PET

A schematic of the molecular structure is shown in figure 6.1. It shows that the PET polymer consists of a rigid phenyl group connected to a more flexible ethyl group. PET has a glass transition temperature of ~75°C, which, as will be explained later in the

chapter, is one of the reasons it has been chosen for this *in-situ* experiment. The crystallisation of polymers has been widely studied [1]-[10]. These experiments, in the main, have been concerned with the morphology of the growing spherulites and the process of crystallisation. A spherulite is a spherical semicrystalline region within the polymer film where the polymer backbone can form into a packed array of lamellae within an amorphous region. In this experiment, we will focus on the rate at which the PET spherulites grow radially, and how this rate is affected by varying thicknesses and temperatures. It has already been shown that the thickness of the film affects the glass transition temperature along with crystallisation kinetics and degree of crystallinity, phase behaviour, morphology, permeability, electrical properties, moisture absorption and dewetting [11].

Scanning Probe Microscope (SPM) studies of the rate of crystallisation of thin films can be conducted in two ways:

1. Samples are annealed ex-situ and later scanned with an AFM to obtain the average sizes of the spherulites as a function of anneal time. The rate of crystallisation can only be inferred by this averaging approach [6].
2. Samples are annealed *in-situ* and on the AFM sample stage, following the crystallisation in real time. It is advantageous to follow individual spherulites while the crystallisation process is occurring, taking images at regular intervals, as the rate of crystallisation is calculated for individual spherulites.

Several groups have carried out experiments on polymers that were crystallized at room temperature. In these experiments the samples were heated to temperatures above their melting point, cooled to room temperature and quickly placed in the AFM to follow the process [12]. More recently, in-situ heaters have been employed, so that a wider range of polymers, and a wider range of temperatures can be investigated [7, 8, 10, 11, 13-17]. Such a heater is designed and used in the current investigation.

There are three characteristic stages in the crystallisation of PET [18]. In the first stage the polymer backbone converts from a *gauche* to a *trans* conformation. The second stage involves the self-organization of the *trans*-polymer chains within the amorphous structure. Crystallisation occurs in the third stage. Radhakrishnan et al [18] have found that with PET thin films at 93°C the third stage occurs around 50min after the start of the anneal.

Due to expansion effects in our heater, and limitations in the Z direction of the AFM, stable images cannot be taken within the first 30mins of heating. Since the main interest of this investigation is in the third stage of crystallisation, this limitation is not critical.

6.2 The crystallisation process

In pure polymers, crystallisation starts with nucleation. However, for most polymers, crystallisation commences at pre-existing nucleation sites such as impurities. These are referred to as primary and crystallisation effects respectively. Once nucleation has

occurred, crystal growth can occur either by secondary (4 new surfaces formed) or tertiary (2 new surfaces formed) processes. In both cases the overall crystallisation rate is given by.

$$w = Cexp(-\frac{U}{R(T_c - T_\infty)})\exp(-\frac{K_g}{T_c(T_m^0 - T_c)})$$

...Equation 6.1

where C is a rate constant, U is an energy constant, R is the gas constant, T_∞ is the temperature at which all segmental mobility is frozen in, and K_g is the kinetic constant for the secondary nucleation [19]. The first exponential term is the temperature dependence of the rate of the short range transport of the crystallising segments. The second exponential term expresses the temperature dependence of the nucleation rate. When typical values of T_g and T_m of PET are used, the general form of the relationship is shown below.

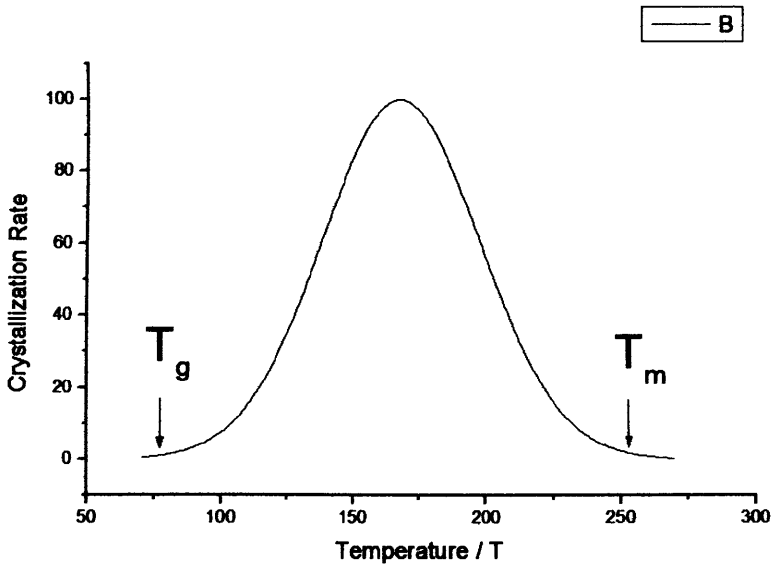

Figure 6.2 – Temperature dependence of the rate of crystallisation of PET.

It is now commonly accepted that there are two stages in the crystallisation of polymers. The primary stage is characterised by the radial growth of spherulites or axialites. In our case we have been growing spherulites which begin as a stack of lamellar crystals that splay apart and branch out. These branches then grow at a constant rate. A small distance behind this growth front, the second stage occurs. Secondary lamellae are formed and grow to fill in gaps left by the primary growth. They continue to grow until they meet other secondary lamellae formed from other branches. In this experiment we will only look at the rate of growth of the primary stage.

6.3 Design of the *in-situ* heater

6.3.1 Requirements of the heater

Other groups are now using in-situ AFM heaters in order to follow the kinetics of a transition. These groups have mainly used commercial heaters, but for cost and temperature stability considerations a heater was designed and built for this crystallisation experiment. Another important factor in our design was that we had a multimode AFM which put size restrictions on the heater. In order to fit within the AFM head the heater ensemble could not be more than 18mm in diameter and 8mm in height.

In a multimode AFM the sample sits on piezoelectric tubes, and the tip is held stationary (apart from being oscillated). During scanning it is the piezoelectric tubes that scan the sample under the tip, rather than the tip passing across the sample. For this reason the

heater ensemble must be light, and the heater wires must be highly flexible so as not to pass on any external vibrations which would affect the movement of the sample. The piezoelectric tubes are also affected by high temperatures; they must not exceed 55-60^{0}C to prevent gradual deterioration of the piezoelectric tubes' response. In order to preserve the long-term performance of our piezoelectric tubes it was decided to keep the base of the heater at a maximum temperature of 45°C. Crystallisation occurs over timescales of tens of minutes to hours at anneal temperatures of 80-100°C. These thermal constraints, together with the above spacial restrictions of the sample stage of the Veeco Multimode instrument, are quite demanding on the heater design.

6.3.2 The Heater stage

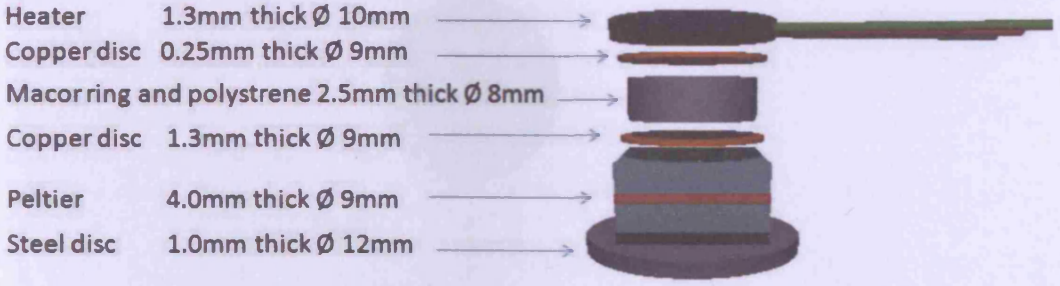

Figure 6.3 – The AFM heater

The heater, as seen in figure 6.3, has three main components which contribute to achieving the required temperature gradient; the Peltier element, the Macor machineable ceramic ring and polystyrene filler, and the heater itself. As mentioned earlier, in order to fit within the AFM head, the heater ensemble could not be more than 18mm in diameter and 8mm in height. However, the height of the heater needed to be

greater than this to achieve the temperature gradient, so a 6mm spacer was fitted under the AFM head to accommodate the heater.

6.3.3 The heating element

The heating element was similar to the one described in chapter 4, in that a mould of the required shape was made, and thermosetting epoxy resin was placed in the mould along with a wound insulated wire and a thermocouple (in a central position). A current was passed through the wire in order to set the epoxy. The size differed from the heater in chapter 4 and the other features were not incorporated, such as the addition of a ceramic pin.

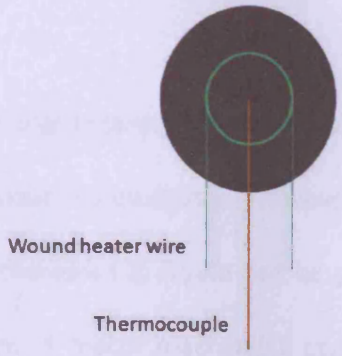

Figure 6.4 – Cross section of the heater used

It was also necessary to calibrate the top temperature of the heater so that the exact temperature of the sample was known. The whole heater ensemble was placed in boiling water and ice water in turn, and measurements of the voltage across the thermocouple were taken. An assumption was made that the thermocouple voltage is

linear with temperature between these two set points. This was the calibration process for the thermocouple buried in the epoxy cured heater element, but the temperature of the sample surface is not necessarily at the same temperature as the heater due to possible gradients across the sample substrate. A second thermocouple was connected to a piece of silicon, of similar dimensions to ones used in the experiments, with silver dag and attached to the heater also with silver dag. The heater was then raised to 100^{0}C and the voltage of the sample thermocouple was noted. This thermocouple was subjected to the same water calibration as the heater thermocouple and it was found that at high temperatures (between 85°C and 100°C), the top surface was consistently 2°C lower than the heater.

6.3.4 The macor ring and polystyrene

A polystyrene spacer was chosen between the upper epoxy-based heater and the Peltier stage for its low thermal conductivity. However, polystyrene suffers from drift at high temperatures, and therefore it would not be possible to follow individual spherulites during crystallisation. A macor machinable ceramic hollow ring was therefore used to provide mechanical stability. The inner space was filled with polystyrene, which provides significantly better insulation than an air gap, since convection currents are suppressed. This component proved to be significant in reducing the heat conduction to the piezoelectric tubes..

6.3.5 The Peltier element

The voltage supplied to the Peltier element was adjusted to help produce the required temperature gradient across the ensemble. The primary objective of the Peltier element was to the keep the bottom surface cool while providing limited heating to the sample stage. Without it the temperature of the piezoelectric tubes would exceed 45°C. The nominal maximum temperature difference across the top and bottom edges of our Peltier was 67°C when 2.1V was applied across it. However, we were not able to obtain this value due to the lack of a large heatsink in contact with the Peltier element. After construction of the heater ensemble, a thermocouple was placed on the bottom steel disc and the sample temperature was held at 90°C. The graph below shows the stainless steel base temperature as a function of applied voltage on the Peltier element.

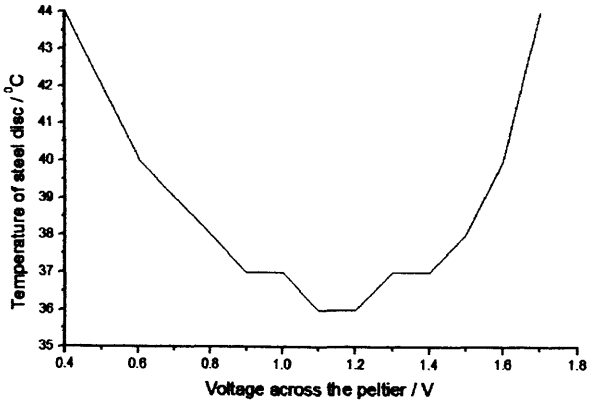

Figure 6.5 – Temperature response of the Peltier for varying voltages

At a sample temperature of 90°C the maximum temperature difference between the sample temperature and bottom temperature is 64°C, close to the nominal maximum of 67°C. From figure 6.5, it was found that the optimum voltage was 1.1V, and as such this

voltage was subsequently employed for all experiments (sample temperatures between 85 and 100°C).

6.4 Sample preparation

The PET used in this experiment was supplied by Goodfellow. A 4% w/w solution was made by dissolving the PET in chlorophenol. Subsequent 3%, 2% and 1% solutions were made from this solution by the addition of further chlorophenol. Samples were made from these solutions by spin casting onto a SiO_2 substrate at 5500rpm for 180 seconds, and annealed in air at 45°C for 3hours, to evaporate any remaining solvent. Prior to spin casting the SiO_2 substrate was placed in a UV/ozone chamber for 10 minutes to clear the substrate of any contaminants. UV/ozone cleaning is a widely used process to ensure that the surface of the substrate is clear of contaminants such as oils and greases[20]. Experiments were carried out on these samples no more than 24hrs after spinning. For film thickness analysis a sharp scalpel blade was lightly dragged across the surface. This produced a gap of approx 10μm wide.

6.5 AFM imaging

Tapping mode images were taken with the Nanoscope DI multimode SPM using Silicon tips, with a force constant of 10-130 N/m, and resonant frequency of 285-315 kHz. Height and phase images were taken during the experiments. A set point ratio of 0.8 was used. Cupere et al have reported that reducing this ratio significantly improves phase images of PET films for single images [10]. Multiple scans were performed over a 5 hour

period using a higher set point ratio of 0.8, which was less invasive over that time period and also resulted in less PET being deposited onto the tip. A scan rate of 16μm/s was used in order to take one 25μm square image every 15mins. Crystallisation in the films took several hours, so an image rate of 15min/image could easily track the process. The AFM scanned from the top of the image to the bottom each time, so that data from any given position is refreshed every 15mins. The images obtained were then subjected to a first order flattening process to compensate for the tilt of the sample. After all scans were completed, a scan of a different part of the sample was taken, and compared with the area already scanned to see if the scanning process itself had affected the growth of the spherulites. In all cases we found that the movement of the tip over the sample had not affected the growth of the spherulites.

6.6 Results and discussion

6.6.1 Thickness dependence on the rate of crystallisation

To illustrate crystal growth, figures 6.6 and 6.7 are included to show growth of the thickest and thinnest films as a function of time, all at 90°C.

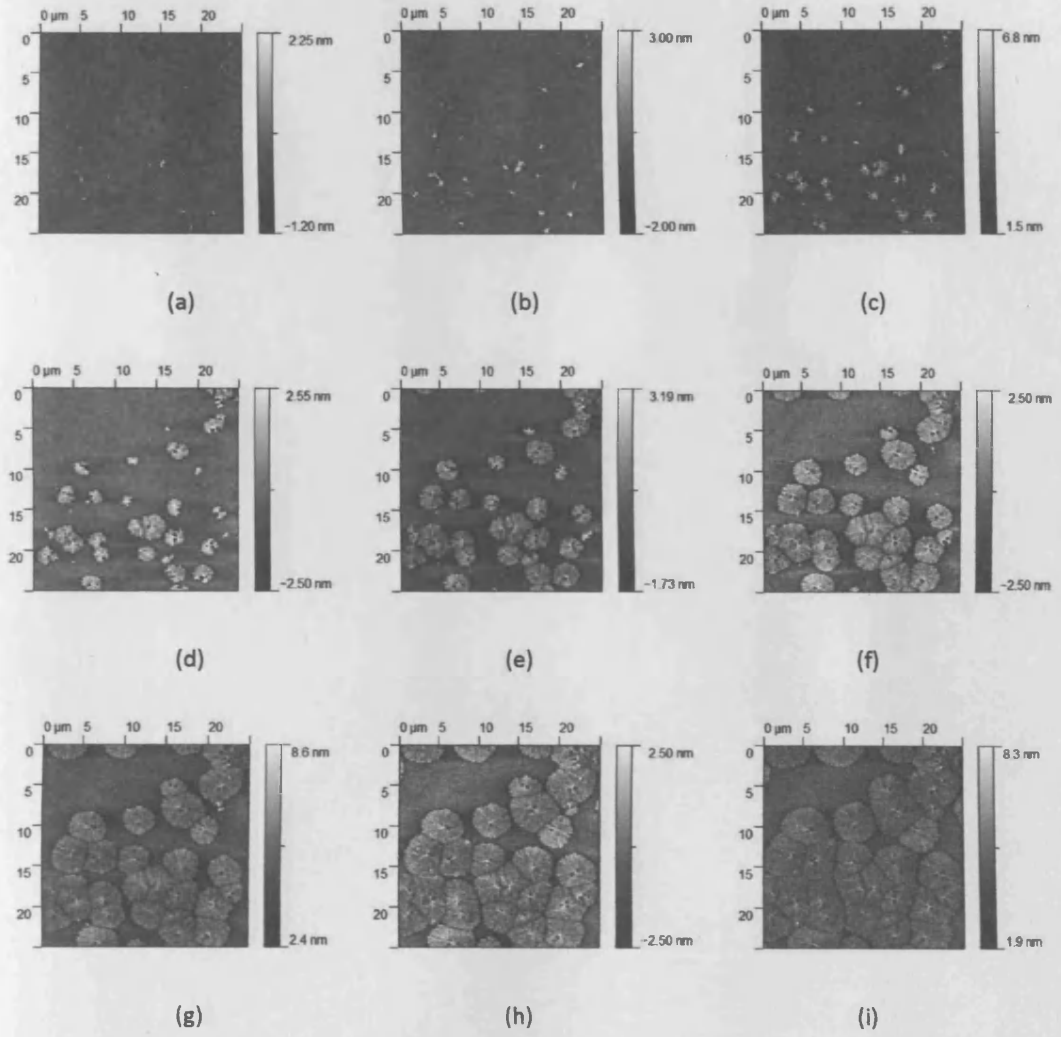

Figure 6.6 – 90 ^{0}C 120nm thick PET films after (a) 30 mins (b) 1 hour (c) 1 hour 30mins (d) 2 hours (e) 2 hours 30mins (f) 3hours (g)3 hours 30mins (h) 4 hours and (i) 4 hours 30mins.

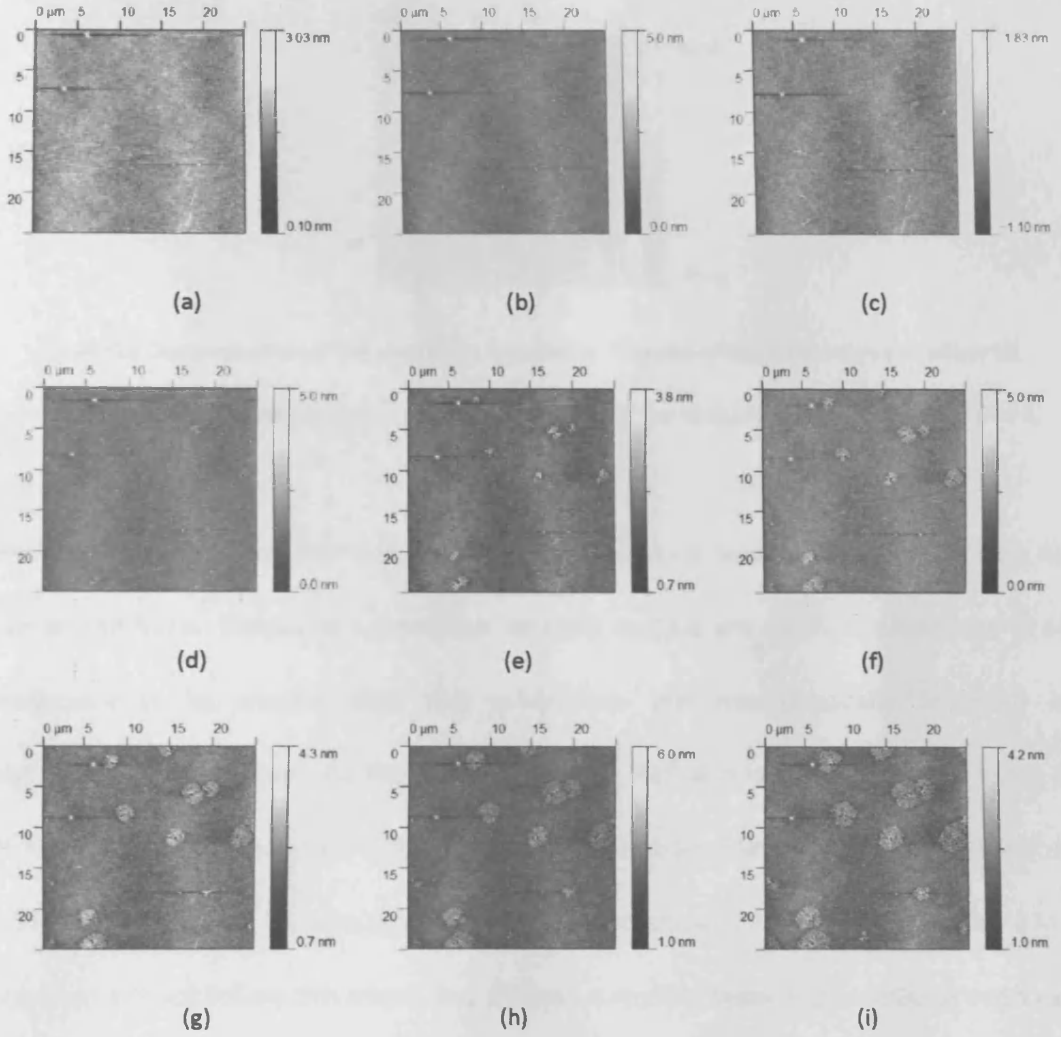

Figure 6.7 – 90 ^{0}C 17nm thick PET films after (a) 30mins (b) 1 hour (c) 1 hour 30mins (d) 2 hours (e) 2 hours 30mins (f) 3hours (g)3 hours 30mins (h) 4 hours and (i) 4 hours 30mins.

Images were also taken at 90°C for thicknesses intermediate to these. Using the built-in analysis program in the Veeco software, it is a straightforward matter to measure the advance of the growth front from the nucleation point. This can be seen in figure 6.8 below.

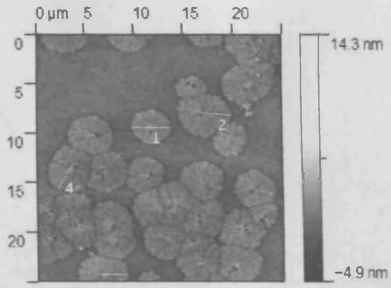

Figure 6.8 Determination of the size of the spherilites. The size of the spherulites can either be determined by the diameter/2, seen in line 1, or the size of the radial lines, seen in lines 2, 3 and 4.

Several spherulites from the same image were measured, and the average of these has been stated here. Particular spherulites for each sample are carefully chosen for these measurements to ensure that the spherulites are not physically impaired by neighbouring spherulites. As the thickness of the PET film is increased from 43nm to 120 nm the radial growth rate of the spherulites increases linearly from 8.0 ± 0.9nm/min to 14.3 ± 1.3nm/min, i.e. the growth rate is proportional to film thickness. The 17nm thick films did not follow this trend, but showed a slightly faster linear radial growth rate than expected of 7.2 ± 0.9nm/min. Samples of films thinner than this were produced (10nm) but these showed no crystallisation after 2hrs at 90°C. Graphs showing the growth for spherulites for the 120nm thick sample annealed at 90°C are shown in figure 6.9. Also shown in figure 6.9 is the growth rate over time for the same sample. Similar graphs have also been made for all other samples.

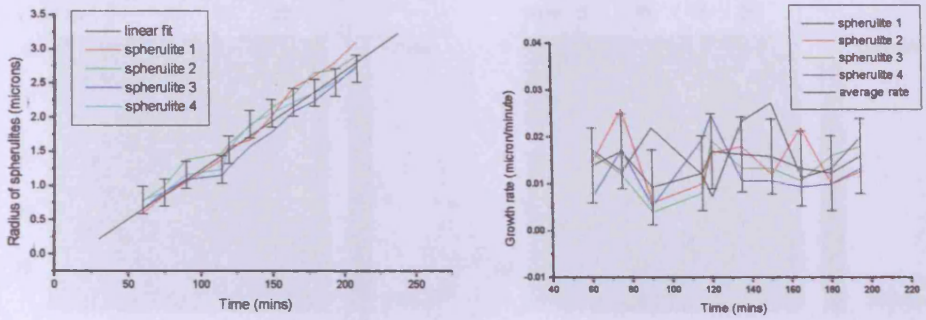

Figure 6.9. Graphs of a) spherulite radius vs time and b) growth rate vs time for 120nm PET film annealed at 90°C.

As can be seen in figure 6.9 the growth of the spherulites is linear over time. The linear fit line is extrapolated back to the intercept with the x axis in order to determine the time at which nucleation occurs. The nucleation of the spherulites within each thickness sample occurs at 14 ± 4 minutes. Once nucleation centres have been created during this initial 14 mins no further nucleation centres occur for the remainder of the heating.

6.6.2 Temperature dependence on the rate of crystallisation

The data in figures 6.6 and 6.7 were all taken at 90°C. As well as these measurements, additional readings were taken at 85, 95 and 100°C. Figures 6.10 and 6.11 show images for these temperatures for the thinnest and thickest samples. An image for 85°C for the thinnest (17nm) sample is not shown as no crystallisation was seen in this sample.

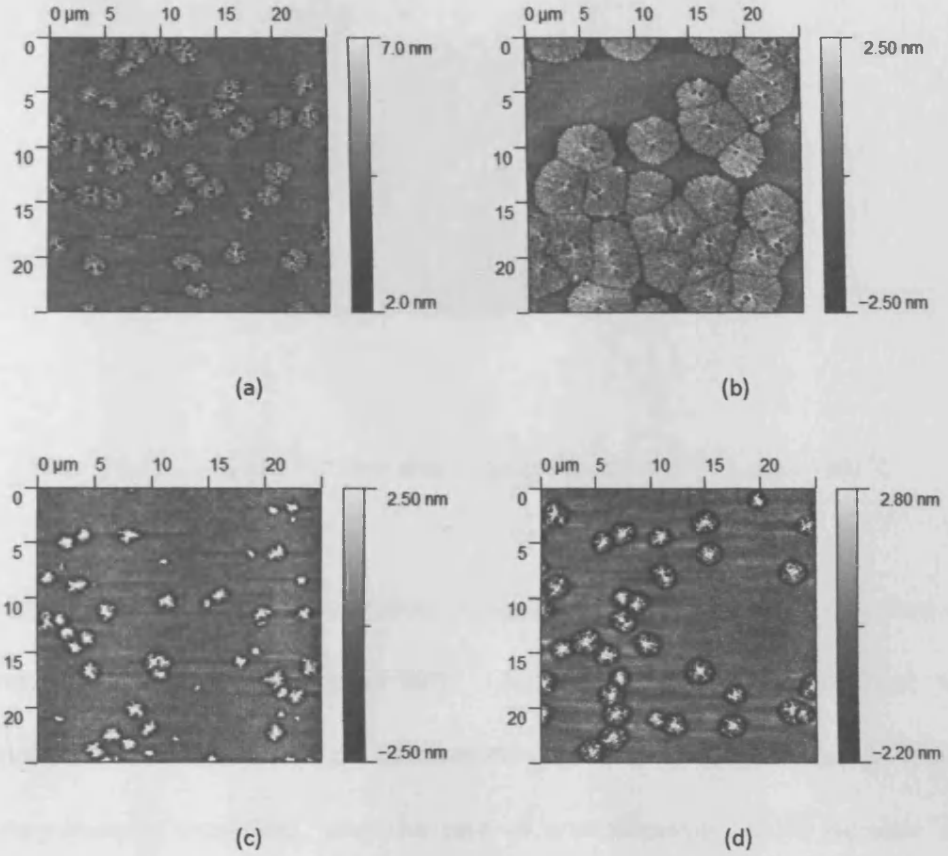

Figure 6.10. 120nm thick PET films after 4hours at (a) 85 ^{0}C (b) 90 ^{0}C (c) 95 ^{0}c and (d) 100 ^{0}C

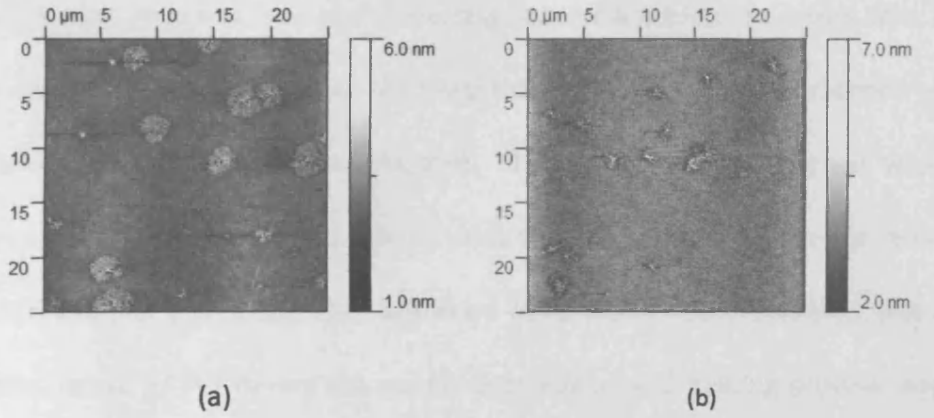

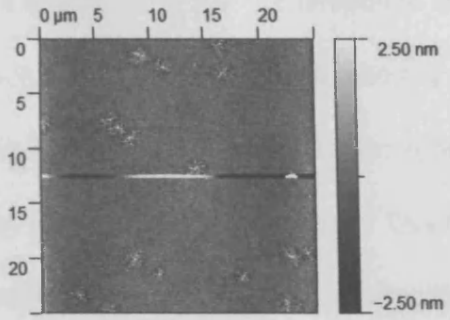

(c)

Figure 6.11. 17nm thick PET films after 4 hours at (a) 90 ^{0}C (b) 95 ^{0}C and (c) 100 ^{0}C

The results seen in this investigation were not consistent with what was expected as the temperature was increased above 90°C. As the operating temperatures in the experiment are at the lower end of the curve illustrated in figure 2, one would expect, as the temperature is increased, that the rate of crystallisation would increase almost exponentially. This trend is indeed seen when the temperature is increased from 85°C to 90°C but when the temperature is further increased to 95°C the rate of crystallisation is actually lower. All the temperatures investigated show nucleation points after 14 ± 4 minutes of heating, and at any given thickness the number density of nucleation centres is similar for all temperatures investigated. This inconsistency between what was expected and what was observed occurred close to the boiling point of water, leading us to question whether the samples had absorbed water from the surroundings, due to the hydrophilic nature of PET during the sample preparation and heating process, and that the water within the PET films was restricting (or promoting) crystallisation.

This postulate resulted in a change of sample preparation in an attempt to address this possibility. Once the PET solution had been dropped onto the substrate, and a film had been produced by spin coating the solution in a nitrogen atmosphere, the sample was transferred quickly onto the heating stage to be 'dried'. This heating stage was housed within a chamber which was flooded with nitrogen, expelling the air originally within the chamber, for the full duration of the drying process. The samples were then removed, exposing the samples to air, and transferred onto the heater, placed on the AFM and all wires required for heating were attached. The samples were exposed to the air for less than 5 minutes during this sample transfer. The AFM was covered with a chamber that was also kept under a positive nitrogen pressure throughout the subsequent heating cycle and scanning process. An oxygen monitor was used to monitor the 'air' inside the chamber covering the AFM to ensure that this positive pressure created by the nitrogen flow into the chamber maintained a moisture free environment for the sample.

This effort to ensure that the samples were only exposed to air for limited periods of time during the sample preparation and crystallisation process resulted in the same rate of crystallisation for subsequent samples. This suggests that either the slower crystallisation at 95°C and above is unrelated to water absorption or that the brief spells of time the samples were exposed to air was enough to absorb water that could not be removed by exposure to nitrogen, nor by the prolonged heating, while the samples were being scanned.

6.6.3 Structure of the growing spherulites

Another main difference seen between the samples annealed at different temperatures is the shape of the growing spherulites. The spherulites grown at 90°C are similar to those seen by De Cupere et al [10], where they "possess a centre of nucleation from which they develop to form crystalline features with a sector-like shape". These sectors grow outwards, and sectors from either side of the nucleation site meet, and the space left is gradually filled in. However, at 95°C and 100°C these 'sector shaped' spherulites are not observed: all spherulites have a circular appearance. At these higher temperatures, the spherulites also protrude further above the surface i.e. they are more spherical in shape rather than the more 2-dimensional, rather flat, shape the spherulites formed at a lower temperature. This can be inferred from the height profiles taken across the spherulites. These profiles are shown in figure 6.12.

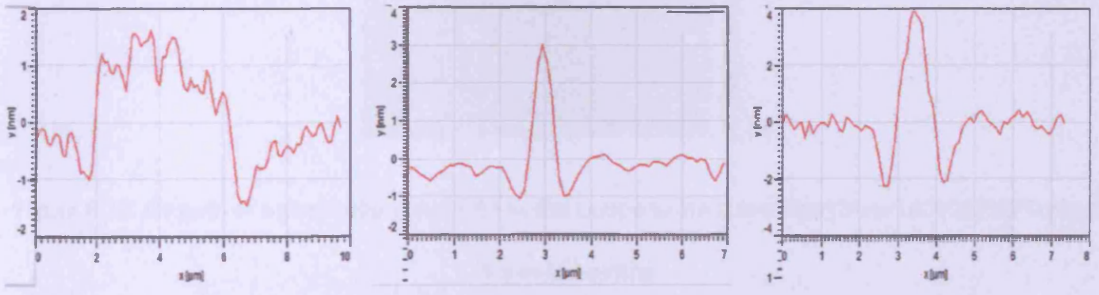

a) b) c)

Figure 6.12. typical profiles across spherulites seen in the thickest samples at a) 90, b) 95 and c) 100°C

The film immediately around the spherulites also shows deeper depression, resulting from the mass transport into the spherulite, impeding further growth.

These results demonstrate that the type of growth of the spherulites is not defined at the moment of nucleation, but rather by the subsequent thermal treatment. Figure 6.13 shows two images of a sample whose heating temperature was switched after 4 hours from 100°C to 90°C for a further 1hr, together with a further image of an expanded spherulite.

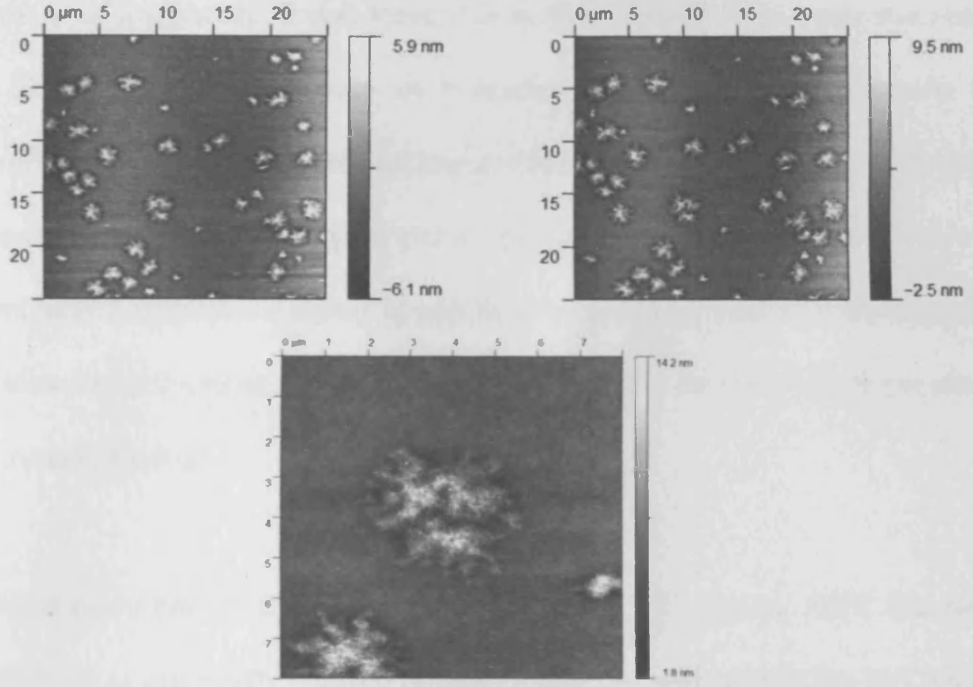

Figure 6.13. Growth of a particular spherulite as the temperature is switched from 100°C to 90°C after 4 hours of heating.

As can be seen in figure 6.13, the spherulite has a densely packed circular structure caused during the heating at 100°C, whereas subsequent growth at 90°C gives a more diffuse branch-like structure on its growth front, which has grown at a higher linear rate. This result suggests that the slower growth rate of the crystalline region above 95°C is related to a change in the structural nature of the growing spherulites rather than to

adsorption of water. However, this conclusion cannot be firmly established from our existing data.

6.7 Conclusion

This investigation attempted to determine how the thickness of the PET films affected the rate of crystallisation. It was found that as the thickness of the films was reduced from 120nm to 43nm the rate of crystallisation decreased proportionally from 13.9nm/min to 8.0nm/min. As the thickness of the film was further reduced, the growth rate continued to fall as the polymer strands became more restricted by the thickness of the film, which resulted in a higher T_g, and therefore a slower rate of crystallisation for a given temperature, until the film thickness was reduced so far as to restrict the polymer from crystallising at all.

As the temperature of the sample was raised to 95°C and to 100°C the rate of crystallisation unexpectedly reduced compared with the rates seen in the 90°C samples. The rate of crystallisation of the 120nm samples at 95°C and 100°C were 6.7nm/min and 8.0nm/min respectively. A question still remains as to whether water, present in the air, which may be absorbed into the sample during preparation, is affecting crystallisation. However, all reasonable measures were taken to reduce the possibility of water being absorbed into the sample.

This investigation was hampered by the reproducibility of results. The results stated and discussed in this chapter were experienced in about two thirds of the samples that were scanned. The remaining samples showed nucleation centres, but the subsequent growth was strongly suppressed, and so were not used for analysis in this investigation.

6.8 References

[1] N. W. Hayes, G. Beamson, D. T. Clark et al, Surface and Interface Analysis, 1996, 24, 723.

[2] Y. Sakai, M. Imai, K. Kaji et al, Macromolecules, 1996, 29, 8830.

[3] R. Pearce, G. J. Vancso, Polymer 1998, 39, 1237.

[4] R. Pearce, G. J. Vansco, Macromolecules 1997, 30, 5843.

[5] Y. Sakai, M. Imai, K. Kaji, M. Tsuji, Journal of Crystal Growth 1999, 203, 244.

[6] K. Taguchi, H. Miyaji, K. Izumi et al, Polymer 2001, 42, 7443.

[7] J. K. Hobbs, A.D.L. Humphris, M. J. Miles, Macromolecules 2001, 34, 5508.

[8] L. G. M. Beekmans, D. W. Van der Meer, G. J. Vansco, Polymer 2002, 43, 1887.

[9] A. Tracz, J. K. Jeszka, I. Kucinska et al, Journal of Applied Polymer Science 2002, 86, 1329.

[10] V. M. De Cupere, P.G. Rouxhet, Polymer 2002, 43, 5571.

[11] H. Schonherr, C. W. Frank, Macromolecules 2003, 36, 1188.

[12] J. K. Hobbs, T. J. McMaster, M. J. Miles et al, Polymer 1998, 39, 2437.

[13] H. Schonherr, C. W. Frank, Macromolecules 2003, 36, 1199.

[14] V. H. Mareau, R. E. Prud'homme, Macromolecules 2005, 38, 398.

[15] J. K. Hobbs, C. Vasilev, A. D. L. Humphris, Polymer 2005, 46, 10226.

[16] J. K. Hobbs, R. A. Register, Macromolecules 2006, 39, 703.

[17] J. K. Hobbs, Polymer 2006, 47, 5566.

[18] J. Radhakrishnan, A. Kaito, Polymer 2001, 42, 3859.

[19] Ulf W. Gedde, Polymer Physics, Kluwar Academic Publishers (1999)

[20] J. Vig, J. LeBus, IEEE Transactions on Parts, Hybrids, and Packaging 1976, 12, 365.

Chapter 7 – Conclusion

This thesis describes structural studies of polymer thin films using grazing incidence x-ray diffraction and atomic force microscopy. The main focus has been on the development of these techniques to probe the film structure during *in-situ* annealing. These approaches are broadly applicable to any polymer films, including the conjugated polymers that have been the focus here. The techniques developed in this investigation could therefore benefit research into a range of applications, such as chemical barriers, adhesion, membranes, sensors, and medical implants.

Chapters 2 outlines the theoretical background to the techniques and the materials investigated. This is followed in chapter 3 by a discussion of the experimental considerations required in the design of an x-ray chamber suitable for in-situ GIXRD studies, along with the design of compact heaters for both GIXRD and AFM (with further details of the AFM heater being discussed in chapter 6).

Chapter 4 concerns an investigation into the crystalline structure of poly(9,9-di-n-octyl-2,7-fluorene). The ultimate goal of this investigation was to produce a method of determining the internal crystalline structure of any polymer unit cell. This included measuring the intensities of crystalline diffraction peaks so that these may be compared with the calculated intensities from a postulated structure, derived from a molecular dynamic process and structure factor calculations. Initially F8 was chosen for this process as it was known to produce a relatively high number of crystalline diffraction peaks. During the investigation a group led by Chen in Taiwan produced a paper which claimed to have already produced such a method using F8. It quickly became apparent that the structure they had postulated failed to correspond to the observed x-ray data that was submitted by this group, or during my investigation. While writing this thesis, we have learned of two other groups who have become aware of the shortcomings of the Chen study. Despite the efforts of several groups to determine the detailed molecular structure of F8, no successful studies have appeared in literature. Despite the intense scientific and technical research into conjugated polymers, detailed structural models remain elusive: the literature is limited to unit cell parameters, molecular spacings and the orientation of the molecular backbone. There is a pressing need for an approach which successfully combines molecular modelling and diffraction analysis in a combined, iterative approach.

Another polymer, poly(3,3'''-didodecylquaterthiophene) (PQT-12), was also investigated using GIXRD (Chapter 5). The size of the crystalline unit cell was determined, as well as the structural effect of depositing the PQT-12 film on top of an OTS monolayer, rather

than a native silicon dioxide substrate. OTS is commonly used as a molecular coating for substrates as it has been found to improve the electronic properties, such as electron mobility, of conjugated polymers in transistor structures. It was found that the OTS monolayer did not change the size of the unit cell of the PQT-12, but it did increase the degree of polycrystallinity observed throughout the thickness of the PQT-12 film.

The investigation into PQT-12 also included a study of the film as its temperature was increased above the glass transition temperature, as well as a study into the affect of molecular weight on the structure of the film. These studies showed that the structure of the as-spun PQT-12 film is metastable. The as-spun crystalline structure was lost upon heating, and was not realised again on return to room temperature. It has been found that the structure seen in the film is also highly sensitive to preparation conditions.

The third polymer investigated was polyethylene terephthalate, PET, a commonly used polymer in soft drinks bottles. The rate of crystallisation was investigated as a function of film thickness, and it was observed that the rate of crystallisation at a given temperature above the glass transition temperature decreases with film thickness. The temperature dependence of the rate of crystallisation was also investigated. It was found that the rate of crystallisation decreased at anneal temperatures of around 95-100°C. This puzzling behaviour suggests that water may be absorbed by the PET films which are mildly hydrophilic in nature. In an attempt to overcome the possible problem of water absorption steps were taken to prepare the samples in a dry environment, by

spinning under nitrogen as well as producing a chamber around the AFM and flooding it with nitrogen to expel all air during the heating/scanning process. The samples were only exposed to air during the unavoidable transfer of the samples from the drying process to the AFM chamber. Despite this effort, the anomalous behaviour remained as subsequent samples produced no difference to the observed rate of crystallisation.

The GIXRD techniques developed for these studies are now being applied to polymer photovoltaic blends in which the structural changes induced during *in-situ* annealing are being followed, with a time resolution of 5 seconds during a 30 minute anneal. This is one technologically significant development arising from the above work. Further applications are likely in the coming decade.

Further work

A primary objective during the study of F8, which unfortunately was not achieved, was to produce a proposed structure from molecular dynamics which produced structure factors that compared well to experimental data. This was mainly due to the complexity of a large unit cell and the interactions between adjacent polymer backbones making generating a proposed unit cell difficult. It is believed that with further time and effort into the structure of the F8 unit cell that a proposed model could be produced. Ultimately once such a model has been produced which matches well with experimental data the system and knowledge gained from this work could be used to produce unit cell structures of other conjugated polymer films.

During the work into the structure of PQT-12 polymer films it has been shown that the structure within these films is sensitive to the conditions in which the films were prepared, for example PQT-12 has shown a very different crystalline diffraction pattern before and after heating above it's glass transition temperature. Future work into the structure of the PQT-12 film could further investigate the sensitive nature of the film structure by altering other preparation parameters such as the angular speed of the sample during spin casting or the solvent used to dissolve the PQT-12 material.

All of the investigations carried out during my studies involved designing and manufacturing equipment to enable the experiments to be conducted. This included designing a sample stage that could be placed onto a multimode AFM that whose top surface could be heated to 100°C while maintaining a low temperature at the bottom of the sample stage to ensure the safety of the multimode AFM's piezoelectric scanners. It became apparent during this investigation that a sample temperature of 100°C was not high enough to produce sufficient data to fully analyse the rate of crystallisation of PET. Therefore future work would also have to contain a new design of the sample stage to increase the physical capabilities.of the sample stage to allow this data to be taken.